

METAL-ORGANIC CHEMICAL VAPOR DEPOSITION OF SILICON/ZINC
SULFIDE QUANTUM CONFINED STRUCTURES

By

ERIC C. BRETSCHNEIDER

A DISSERTATION PRESENTED TO THE GRADUATE SCHOOL OF THE
UNIVERSITY OF FLORIDA IN PARTIAL FULFILLMENT OF THE
REQUIREMENTS FOR THE DEGREE OF DOCTOR OF PHILOSOPHY

UNIVERSITY OF FLORIDA

1997

Copyright 1997

by

Eric C Bretschneider

ACKNOWLEDGMENTS

I would like to thank the many individuals who have helped make this work possible. First, I would like to thank Dr. Tim Anderson for providing me with the opportunity for an exciting and challenging project. I am grateful to Dr. Paul Holloway and Dr. Kevin Jones for their willingness to take time to answer my questions and for helping me in countless ways with my project. I thank Dr. Chang Park for helping me to learn enough about statistics to find a key piece of information vital to the completion of this project. I would also like to thank Dr. Gar Hoflund for helping me to understand surface science techniques and for serving on my dissertation committee.

The experimental portion of this project could not have been completed without the assistance of the entire team at the Surge Area. Their friendship has meant more to me than you could possibly know. To Clint, I give my thanks for all the assistance performing experiments and creating numerous diversions to brighten Steve's day. To Albert, I give many thanks for the late night work characterizing samples so we would have data for the next day's run and for teaching me more about the English language. To Steve, I give my thanks for keeping things running in the clean room. This project could not have been completed without his help troubleshooting and fixing problems. I thank him also for his help making some of those dreary days a little brighter. To Olga go my thanks for helping me learn even more about MOCVD and for the frank discussions that helped me get through it all. Special thanks go to Paul Maruska, who was in many ways the grandfather of this project.

In the area of characterization, my thanks go to Brian for teaching me TEM prep, Wish for the help with TEM, Maggie and Balu for the SIMS work, and Linda for her timely assistance with PL.

I thank my family, for the patience they showed in the years I spent as a graduate student.

And last but not least, many heart felt thanks go to my wife, Kathleen, for tolerating the many late nights and early mornings required to get me through this project. I could not have completed it without her support.

TABLE OF CONTENTS

	<u>Page</u>
ACKNOWLEDGMENTS	iii
TABLE OF CONTENTS	v
ABSTRACT	viii
 CHAPTERS	
1 MOTIVATIONS AND OBJECTIVES.....	1
1.1 Motivation	1
1.2 Problem Definition	2
1.3 Background	3
1.4 Materials Review	9
1.4.1 Silicon	9
1.4.2 Silicon Dioxide	12
1.4.3 Porous Silicon	13
1.4.4 GaAs on Silicon	14
1.4.5 Zinc Sulfide	16
1.5 Processing Parameter Restrictions	19
1.6 Proposed Research	20
1.6.1 Device Structure	22
1.6.2 Structure Requirements	22
1.6.3 Research Goals	32
1.6.4 Growth Facilities	34
2 QUANTUM MECHANICAL CONSIDERATIONS	37
2.1 History	37
2.2 The Schrödinger Equation	48
2.2.1 Background	48
2.2.2 Infinite Barrier Solutions	51
2.2.3 Finite Barrier Solutions	53
2.2.4 Tunneling	57
2.3 Device Considerations	60
2.3.1 Confinement Energies	60
2.3.2 Tunneling	64

2.3.3	Critical Thickness	64
3	ZINC SULFIDE GROWTH	69
3.1	Substrate Preparation	69
3.2	Zinc Sulfide Growth	73
3.2.1	Parameter Space	73
3.2.2	Analysis	75
3.3	Doping Studies	82
3.3.1	Aluminum Doping	82
3.3.2	Contact Studies	84
3.3.3	Carrier Concentrations	90
4	SILICON GROWTH	94
4.1	Silicon on Zinc Sulfide	94
4.1.1	Substrate Preparation	94
4.1.2	Silicon on Zinc Sulfide Growth	95
4.1.3	Zinc Sulfide Surface Effects	106
4.1.4	Optimized Surface	115
4.2	Silicon on Silicon	116
4.2.1	Low Temperature Silicon Preparation	116
4.2.2	Silicon on Silicon Growth	119
5	DEVICE FABRICATION AND TESTING	123
5.1	Zinc Sulfide/Silicon/Zinc Sulfide Structures	123
5.1.1	Growth Conditions	123
5.1.2	Characterization Results	124
5.2	Device Fabrication and Testing	131
5.2.1	Device Fabrication	131
5.2.2	Testing Results	132
6	CONCLUSIONS	133
6.1	Review of Results	133
6.1.1	Epitaxial Growth	133
6.1.2	Quantum Confinement Effects	134
6.2	Directions for Future Research	135
6.2.1	Device Optimization	135
6.2.2	Silicon Quantum Dot LED	139
6.2.3	Silicon/Zinc Sulfide LED	141
6.2.4	Long Wavelength Quantum Cascade LED	141
6.2.5	New Silicon on Insulator Technology	143
6.2.6	Low Temperature Silicon Cleaning with H_2S	144

APPENDICES

A	NUMERICAL SOLUTIONS TO THE SCHRÖDINGER EQUATION	146
B	APPROXIMATE SOLUTIONS TO THE SCHRÖDINGER EQUATION	156
	REFERENCES	164
	BIOGRAPHICAL SKETCH	175

Abstract of Dissertation Presented to the Graduate School
of the University of Florida in Partial Fulfillment of the
Requirements for the Degree of Doctor of Philosophy

METAL-ORGANIC CHEMICAL VAPOR DEPOSITION OF SILICON/ZINC
SULFIDE QUANTUM CONFINED STRUCTURES

By

Eric C. Bretschneider

Chairman: Dr. Timothy J. Anderson
Major Department: Chemical Engineering

A comprehensive study of low pressure metal-organic chemical vapor deposition growth of zinc sulfide and silicon has been performed. The parameter space for successful deposition of both materials has been investigated and found to overlap, allowing successful deposition of both zinc sulfide and silicon under similar conditions.

Undoped and aluminum doped zinc sulfide and silicon films were grown on both (100) and (111) 4° off orientation silicon substrates. Diethyl zinc, hydrogen sulfide, triethyl aluminum and disilane were used as precursor materials. It was found that high quality epitaxial zinc sulfide films could be deposited over the temperature range of 300 to 650 °C. Growth rate was found to be nearly independent of temperature over this temperature range indicating a mass transfer limited growth mechanism. Aluminum doping yielded low resistivity, n-type material.

Key parameters affecting the surface roughness of zinc sulfide films were determined using a fractional factorial design. This method increases the efficiency of data collection and allows easy determination of the magnitude of multi-parameter interactions. The parameters studied included substrate orientation, deposition temperature, precursor concentrations, total hydrogen flow and the push flow ratio of the alkyl and hydride injectors.

Silicon growth rates varied from 120 to 9000 Å/hour at 450 and 600 °C respectively. A strong temperature dependence of the growth rate was found indicating a reaction limited step with an activation energy of 36.7 ± 4.3 kCal/mole. This agrees well with the energy barrier of 34.5 ± 4.6 kCal/mole for surface diffusion of hydrogen.

Quantum mechanical calculations that take into account the differences in effective masses for electrons and holes in silicon and zinc sulfide indicate that the band gap energy of a silicon quantum well shifts into the visible portion of the spectrum for well widths below 20Å.

Samples containing single and multiple quantum wells of silicon with zinc sulfide barriers were grown and characterized by photoluminescence, optical absorption, Raman spectroscopy, X-ray diffraction, scanning electron microscopy, transmission electron spectroscopy, and secondary ion mass spectroscopy. Additional samples with aluminum doped zinc sulfide cap layers were fabricated into LED devices using an indium/gallium alloy for contact.

CHAPTER 1

MOTIVATION AND OBJECTIVES

1.1 Motivation

Recent advances in increasing the switching speeds for silicon based devices have resulted in a situation in which the information transfer rate from one chip to another is limited by the ability of electrical interconnects to transmit information. The increased packing densities of devices in silicon-based compounds this problem by requiring additional area on the periphery of the chip for electrical interconnects. As the number of interconnects required increases, so does their space requirement, thus increasing the size of the chip and the length of the electrical leads. The development of an efficient optical emitter that could be incorporated with existing silicon-based technology would represent a significant breakthrough in the area of information transfer.

Further motivation for development of a silicon-based light emitting structure is spurred by recent advances in porous silicon which demonstrates high efficiency visible light emission. Porous silicon is characterized by a dendritic structure and an extremely high ratio of surface area to volume. These characteristics lead to difficulties in forming reliable ohmic contacts and fragile devices. It is proposed to investigate an epitaxial heterostructure device configuration to circumvent these problems. Using metal-organic chemical vapor deposition (MOCVD), silicon quantum well structures will be grown in

an attempt to alleviate these problems while still maintaining the desirable light emitting properties of porous silicon.

1.2 Problem Definition

In order to establish a research plan, it is first necessary to define the problem, the desired solution and determine any limitations on acceptable solutions. Simply stated, the problem is that no suitable technologies exist which allow integration of optical emission and detection devices with silicon-based logic or computational circuitry on a single substrate. Silicon is an indirect band gap semiconductor and as such, it is not possible to use monolithic silicon as a base material for the construction of an efficient optical emitter. Current applications requiring both optical emitters and silicon-based computation circuitry rely on electrical waveguide wiring to transmit electrical signals to a compound semiconductor based-emitter. The resulting increase in packaging costs and the inefficient rate of electronic data transmission at today's switching speeds increases cost and decreases performance. Two potential solutions are develop a solid state optical emitter that could be monolithically integrated with existing silicon-based circuitry or to develop computational circuits based on gallium arsenide (GaAs) technology. The goal of this study is to develop an optical emitter that can be integrated with silicon-based circuitry.

Two approaches exist for integrating the theoretical device with silicon circuitry. If the emitter device is fabricated first, then the doping profiles and device materials must be stable at silicon processing temperatures. Since typical silicon processing temperatures are greater than 1000 °C and most compound semiconductor materials are deposited at temperatures below 700 °C, it is unlikely that this approach would succeed.

Alternatively, the device could be formed after silicon processing. In this case, the fabrication of the emitter device would have to take place at temperatures low enough to not affect the doping profiles in the silicon circuitry. It is also important that the processing chemistry not interact with any of the silicon device components (e.g. doping or passivation layers).

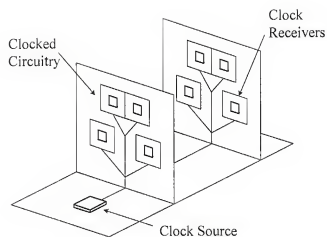
This conclusion leaves three possible fundamental approaches for the development of an efficient optical emitter that can be monolithically integrated with silicon-based circuitry. The first is to somehow modify silicon so that it becomes a direct band gap material. One way this may be accomplished by anodic etching¹ or spark erosion² of bulk silicon to form so called porous silicon. A second approach is to employ a heteroepitaxial emitter device formed from a direct band gap semiconductor such as GaAs or InP. The third possibility, which can be viewed as a combination of the first two approaches, is to use a wide band gap semiconductor as a barrier material to produce quantum confinement effects required to achieve efficient photon emission from silicon.

1.3 Background

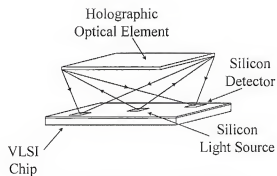
In terms of commercial electronic device applications, silicon has dominated the market as a host semiconductor material. Several characteristics of silicon, including its availability in dislocation free, large area single crystal wafer form and the dielectric properties of its native oxide have allowed it to gain this position of dominance. The indirect band gap of bulk silicon however, has prevented its use in efficient light emitting device applications. This fundamental inadequacy has created a situation that represents a two fold bottleneck for information transfer.

The first limitation is related to the decreased response times of silicon based electronic devices. Current technology allows switching at extremely high speeds (~ 10 picoseconds)³. Unfortunately, the transfer rate of data and timing pulses between chips and boards remains limited by the RC time constants of copper or aluminum wiring. As a result of these delays, electrical interconnects can only transfer rise times (signal pulses) of about 1 nanosecond between boards.³ Even with electrical waveguide wiring, there continue to be problems with impedance mismatches and transmission line losses, which lead to delays in data transmission and skewing of clock arrival times even for different locations on the same chip. This has resulted in an increased emphasis on the development of new materials and structures which can dramatically improve the speed and efficiency of information transfer in advanced processor or telecommunications systems, whether from chip to chip, board to board, or machine to machine.

Optical signals which travel at the speed of light can significantly reduce this interconnection problem.^{4,5} It would therefore be desirable to supplant copper or aluminum wiring with monolithically integrated, all solid state optoelectronic signal-transfer devices. Consequently, present investigations of optical interconnects involve the labor-intensive and hence costly attachment of III-V compound semiconductor light-emitting diodes (LEDs) or laser diodes onto silicon chips. This approach results in a hybrid chip with the electronic functions carried by silicon components and light emission by a III-V material such as GaAs or InP. True wafer scale integration could become a reality if all of the light-emission, light detection, and electronic amplification functions could be implemented directly on a single silicon wafer.



a) Electrical Clock Distribution



b) Optical Clock Distribution

Figure 1-1. Electrical clock signal distribution (a) requires transmission through wires. Optical distribution (b) can take place in three dimensions without interference.

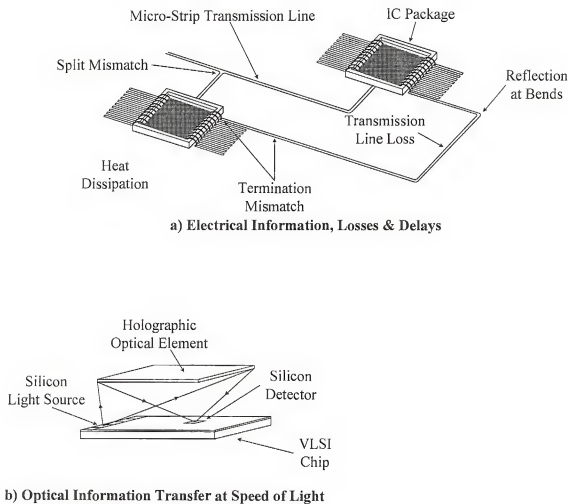


Figure 1-2. Electrical data transmission (a) suffers from signal delays and loss due to RC constants inherent with wiring. Optical data transmission (b) occurs at the speed of light and can transmit data in three dimensions without interference.

The second bottleneck, that also represents a potential barrier to the continued advancement of silicon integrated circuit (IC) performance is related to the area required by interconnects. The exponential growth of semiconductor chip capabilities is now being hindered by the difficulties associated with making interconnections to chips which have scaled-down device dimensions. The scaling down of feature sizes is usually accompanied by a process called "stuffing," or filling empty space on the chip with more transistors. When scaling-down a transistor's linear dimension by s , the number of transistors that can be stuffed into the chip increases by s^2 . Thus, as the number of elements in a chip grows, the number of interconnections required by the chip also grows. Eventually, a limit is reached in available space around the perimeter for placing bonding pads as each bonding pad requires a minimum of $400 \mu\text{m}^2$ of space. For modern high density chips, optical information transfer can offer a possible route to overcoming this interconnection problem.

Optical interconnects would also offer freedom from the planar constraints of electrical wiring. Light beams can pass through each other in three dimensions giving enormous flexibility to the package designer. Thus devices which emit light perpendicular to their surfaces can significantly increase the number of possible connections. Unfortunately, as stated previously, attempts to integrate optical and electronic interconnects have always raised the question of materials technology. Optical emission devices have not been possible using silicon. Fortunately, though, silicon has always been an excellent detector material. To use monolithic Si diode detectors, the

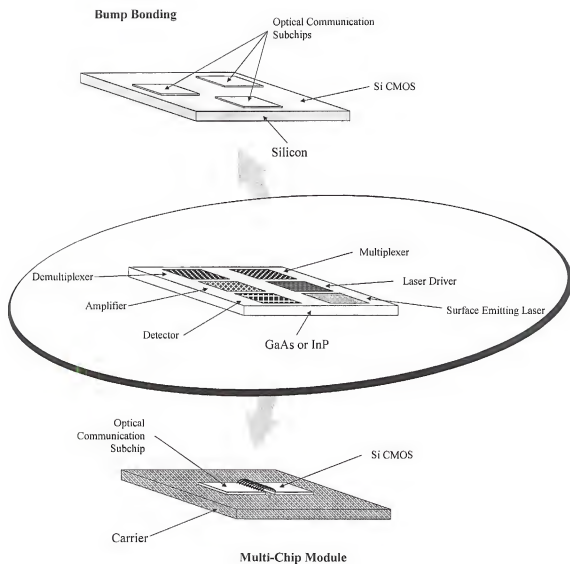


Figure 1-3. Present methods for optical interconnects involve post-processing assembly of non-silicon materials.

emitter wavelength must be shorter than about 1000 nm. Thus hybrid approaches have concentrated on the integration of GaAs light emitters (880 to 900 nm wavelength) with silicon detector and electronics.

1.4 Materials Review

1.4.1 Silicon

Silicon is the second most abundant element in the earth's crust after oxygen. It is readily available in high purity single crystal substrates with diameters to 300 mm. It can be readily doped to make n or p-type material using, for example, boron or phosphorus, respectively. It has a stable native oxide that can be used for passivation or as a dielectric. Its room temperature band gap of 1.12 eV corresponds to an emission wavelength of 1107 nm which is in the infrared portion of the spectrum.

Unfortunately, it is an indirect band gap semiconductor which makes it unsuitable for use in light emitting devices. In indirect band gap materials, the conduction band minimum and the valence band maximum occurs at different momentum coordinates in the energy-momentum plane. Due to this difference in momentum, it is not possible for an electron and a hole to recombine directly. Conservation of momentum requires that the electron and hole interact with a phonon, making recombination a three body interaction. As a result, it tends to be a relatively inefficient process. For direct band gap materials, electrons at the conduction band minimum and holes at the valence band maximum have the same momentum. Thus recombination may be rapid and efficient.

Silicon thin films are often grown by chemical vapor deposition (CVD) techniques using silane and chlorosilane based precursors. Typical deposition temperatures for single crystal silicon range from 900 °C to over 1200 °C. As the

growth temperature is decreased, the crystallinity of the deposited material degrades and polycrystalline material is deposited to approximately 600 °C. At still lower temperatures amorphous silicon is deposited.⁶

Although single crystal silicon can be deposited at a temperature as low as 900 °C when using silane based precursors, typical growth conditions involve temperatures above 1000 °C. CVD of epitaxial films is a complex multistage process which involves gas phase transport, surface adsorption and desorption, surface diffusion and surface reactions. The growth rate behavior of a CVD growth process with respect to growth temperature typically displays three different limiting regimes as shown in figure 1-4. Typically at low temperatures, surface reactions will be the rate limiting step. Since CVD reactions are normally thermally activated, the growth rate will vary with temperature. Growth in this regime imposes tight restrictions on the temperature uniformity, as minor variations in temperature will result in different growth rates and lead to non-uniform film thicknesses.

As the temperature increases, the reaction rate will also increase. Eventually it will reach a rate where reaction is no longer the controlling step and the process enters a new growth regime. If the surface reaction proceeds rapidly enough, it will be limited by the delivery rate of reactants to the surface. Here the controlling step is the transport of reactants from the bulk gas phase through the boundary layer to the surface. This growth regime is termed mass transfer or for a stagnant boundary layer diffusion limited. Since gas phase diffusion is a nearly temperature independent process, the growth rate does not change significantly with temperature. Most CVD processes are designed to operate in this regime, since the growth rate is insensitive to minor temperature variations

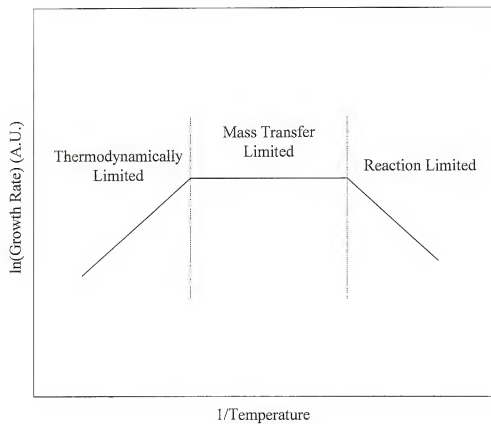


Figure 1-4. Typical rate limiting regimes in CVD processes.

across the substrate. At still higher temperatures, reaction and transport rates can be sufficiently high that equilibrium prevails and the system experiences an overall decrease in growth rate.

1.4.2 Silicon Dioxide

One of the great advantages of silicon in use for semiconductor applications is its stable native oxide. Silicon dioxide films can be deposited with or without dopants. Undoped silicon dioxide is used as an insulating layer between metallizations, an ion implantation or diffusion mask, or as a cap layer over doped regions to prevent outdiffusion during heating cycles. Phosphorus, arsenic, and boron doped silicon dioxide can be used as an insulating layer between metallizations, a gettering source, a diffusion source, or a final passivation layer in devices.⁷

Several different methods have been developed for depositing silicon dioxide. Films can be deposited at temperature below 500 °C using silane, oxygen, and a dopant.⁸ This reaction is particularly important for deposition over aluminum metallization, since silicon and aluminum form a eutectic at a temperature of 577 °C. Other methods rely on the decomposition of tetraethoxysilane $\text{Si}(\text{OC}_2\text{H}_5)_4$ at temperatures between 650 °C and 750 °C⁹ or the reaction between dichlorosilane and nitrous oxide at low pressures and temperatures near 900 °C.¹⁰

1.4.3 Porous Silicon

Given silicon's indirect band gap, conventional wisdom held that efficient luminescence was not possible in such materials¹¹ until the advent of porous silicon.¹² The surfaces of porous silicon, created by electrochemical etching, are covered with a myriad of microscopic silicon wires and dots. The dimensions of these features are on the order

of 1 to 5 nm.¹³ Bright photoluminescence has been observed from these silicon structures in the visible portion of the spectrum,¹⁴ suggesting that the radiative recombination mechanism for nanodimensional silicon is much different than that for bulk crystalline silicon. Several mechanisms have been proposed to account for the photoluminescent behavior of porous silicon including: absorbed fluorine (from the HF electrolyte),¹⁵ siloxene,¹⁶ amorphous silicon,¹⁷ absorbed hydrogen and hydroxyl groups,^{18,19} quantum wires effects,¹ and three-dimensional quantum confinement.²⁰ Chang conducted a review of these mechanisms and after comparing the characteristics of porous silicon with the results predicted by these models he concluded that quantum confinement effects were responsible for visible light emission from porous silicon.²¹

There are several different mechanisms by which confinement may increase the PL efficiency of silicon. Strong quantum confinement may enhance scattering or phonon related processes that make efficient radiative recombination possible, with radiative lifetimes that are very close to those encountered in direct band gap semiconductors.²² Another possibility is that as a consequence of the Heisenberg Uncertainty Principle, the wave function of electrons and holes spread out enough to produce significant overlap and hence lead to efficient recombination. Alternatively quantum confinement may lead to band folding^{23,24,25} and a subsequent shift to direct band gap behavior. Consequently, there is considerable interest in studying porous silicon structures which appear to exhibit quantum confinement effects,²⁶ especially the emission of visible light under optical or electrical excitation.

High magnification scanning electron photomicrographs of porous silicon reveal a dendritic structure. Unfortunately, the etched silicon material tends to be inhomogeneous

in structure due to the rapid nature of the etching process. For many applications, the rough features of porous silicon make electrical contacting difficult. Additionally, the enormous surface area may result in an extremely high density of surface states or provide unacceptable concentrations of non-radiative recombination centers.

1.4.4 GaAs on Silicon

In recent years, a great deal of effort has been expended in attempts to grown epitaxial GaAs on silicon substrates. The motivations behind these attempts are based on both economics afforded by inexpensive, large area silicon substrates and the optoelectronic performance of GaAs-based devices. Three major barriers exist to the development of GaAs on silicon optoelectronic devices: the high defect density of the epilayers resulting from the large lattice mismatch (~4%) between the GaAs and silicon, anti-phase domain generation due to polar on non-polar growth, and the residual stress produced by the large difference in thermal expansion coefficients. Although it is possible to grow epitaxial GaAs on silicon substrates, typical dislocations densities are on the order of 10^9 cm^{-2} or higher.²⁷ Several techniques have been developed in an attempt to produce high quality material with a low dislocation density.

1.4.4.1 Thermal cycle annealing

The thermal cycle annealing process involves deposition of a low temperature (400 °C) buffer layer of GaAs on silicon. The temperature is then ramped to a value in the range of 600 to 750 °C and a 1.5 to 2 μm film is deposited. Afterwards, the film is cooled to near room temperature and then heated to a temperature between 700 and 900 °C under an arsine atmosphere with temperature ramp rates between 50 and 100 °C/minute. This temperature cycle is then repeated.²⁸ The operative mechanism for

dislocation reduction is believed to be dislocation coalescence.²⁹ It has been found that the reduction of dislocation density is correlated with the number of thermal cycles and not the total anneal time. Dislocation densities as low as $5 \times 10^6 \text{ cm}^{-2}$ have been obtained, although numerical analysis predicts it is possible to obtain a dislocation density of less than $1 \times 10^5 \text{ cm}^{-2}$ if the thermal annealing is carried out for at least 1000 cycles.²⁸ As a comparison, commercial liquid encapsulated Czochralski (LEC) grown substrates are available with dislocation densities of $1 \times 10^5 \text{ cm}^{-2}$ for semi-insulating material and $< 1 \times 10^4 \text{ cm}^{-2}$ for doped material.

1.4.4.2 Superlattice buffers

An alternative method for reducing the dislocation density involves the use of superlattice layer structures. The primary drive in defect density reduction is the strain due to mismatch at the interface of the superlattice layers.^{30,31} Mixed dislocations are strongly influenced by the strain field at the superlattice interfaces. At strain levels resulting from mismatches of approximately 1% or more, the shear component of the stress bends 60° dislocations at the interface, resulting in dislocation annihilation or repulsion.³² It has also been reported that aluminum at the interface of a GaAs/ $\text{Al}_x\text{Ga}_{1-x}\text{As}$ structure tends to segregate to dislocations and enhance their lateral migration.^{33,34} The lowest reported defect densities for material grown using this technique has been on the order of $1 \times 10^5 \text{ cm}^{-2}$.³¹

1.4.4.3 Conformal Growth

Conformal growth essentially involves lateral growth from a GaAs “seed” to obtain low defect density material. The principal technological steps are as follows. First a layer of Si_3N_4 and then a layer of amorphous silicon. These layers are then patterned

and etched. GaAs is then deposited in the trenches left behind from etching. Afterwards, another Si_3N_4 layer is deposited. The amorphous silicon layer is then selectively etched and GaAs is grown in the void between the two remaining Si_3N_4 layers.^{35,36} Defect densities below $1 \times 10^5 \text{ cm}^{-2}$ have been achieved using this method.

Cracks have been observed in conformal growth material. It is believed that these are due to the excessive strain caused by the difference in thermal expansion coefficients of the materials used.³⁶ Similar cracks have also been reported for material grown by lateral overgrowth of GaAs using SiO_2 as a mask material.³⁷

1.4.4.4 Growth on patterned substrates

Growth on patterned substrates seeks to reduce dislocation densities by limiting the area of growth. As threading dislocations escape at the edge of small area growth, they are effectively “filtered out” of the growing epilayer and as a result, the defect density tends to decrease as the layer thickness increases.^{38,39} Fitzgerald and Chand studied the effect of varying mesa geometry and width.⁴⁰ Mesa grown material was characterized by cathodoluminescence (CL). They were able to obtain fairly constant CL intensity for 40 μm wide mesas and found that the integrated CL intensity for this material was equal to that of control GaAs on GaAs material grown with the same doping level.

1.4.5 Zinc Sulfide

Zinc sulfide has been studied as a phosphor material since the discovery of powder luminescence by Destriau in 1936.⁴¹ Its most common use is as a phosphor material for CRT phosphors and for thin film electroluminescent devices. It is a direct band gap semiconductor with a band gap energy of 3.62 eV in the cubic phase and 3.8 eV

in the hexagonal phase. These properties have made it attractive for use in short wavelength optical device applications.

Zinc sulfide thin films have been grown by a number of techniques including evaporation,⁴² vapor transport,⁴³ molecular beam epitaxy (MBE)⁴⁴ and MOCVD.⁴⁵ Much of the research on zinc sulfide thin film growth has involved the use of silicon substrates. Silicon is an excellent candidate substrate for zinc sulfide heteroepitaxy. It has a similar lattice parameter (0.40% lattice mismatch at room temperature) and is readily available in large diameter, defect free substrates. Researchers have come to different conclusions on the best silicon orientation for zinc sulfide growth. It has been variously reported that single crystal zinc sulfide could be deposited on (111) silicon substrates, but not on (100) silicon and vice versa.^{42,43,44,45} Most of these conflicting results can be traced back to thin surface oxide layers that were not completely removed prior to growth. Recent reports show that single crystal zinc sulfide can be readily deposited on both (111) and (100) oriented silicon substrates.⁴⁶

Zinc sulfide is found as a naturally occurring mineral in two forms: sphalerite (cubic) and wurtzite (hexagonal) and is notorious as the poorest electrical conductor among the common sulfides.⁴⁷ This poor conductivity is due to a Schottky equilibrium constant that is higher than the electron-hole equilibrium constant.⁴⁸ In other words, a crystal containing impurities is able to lower its overall energy by forming vacancies that compensate electrically active dopants.⁴⁹ At high growth temperatures, the compensation mechanism dominates and insulating material is deposited. At low growth temperatures, less energy is available to overcome the energy barrier to forming compensating

vacancies. Zinc sulfide has been deposited as low resistivity n-type films using aluminum, indium, or chlorine as donor species.^{50,51,52}

As with other wide band gap II-VI materials, it is extremely difficult to obtain low resistivity p-type material. The author knows of no reports of low resistivity p-type material. This fundamental shortcoming has led to the virtual abandonment of zinc sulfide research for optoelectronic device applications. Most zinc sulfide research today focuses on its use as a host material for thin film electroluminescent device structures.^{53,54}

Depending on the growth method used, zinc sulfide films are usually deposited in the temperature range of 200 to 400 °C. Higher growth temperatures have been used, but this range is preferred due to zinc sulfide's high congruent sublimation pressure. For this reason, CVD growth is usually performed using a high excess of sulfur to suppress sublimation. This situation is analogous to that for CVD growth of III-V materials in which the volatile group V element is generally present in concentrations between 20 and 100 times that of the group III elements.

1.5 Processing Parameter Restrictions

As stated previously, any process used to develop an efficient optical emitter that can be monolithically integrated with silicon-based circuitry as a final processing step must leave the existing device structures intact. This imposes some rather strict limitations on processing conditions for device fabrication.

Porous silicon is obviously poor choice for optoelectronic integration. Even if the problems with short lifetimes and fragile devices can be solved, the processing conditions required to create porous silicon rule out its use with silicon circuitry. Anodic etching involves the use of a HF-based electrolyte. HF would rapidly attack silica passivation

layers. Spark processing is not a viable alternative since the high electric fields involved would likely destroy the existing circuitry.

The maximum process temperature is a serious consideration. As mentioned previously, any processing taking place after aluminum metallization must take place at a temperature below the silicon-aluminum eutectic temperature of 577 °C. This fact poses a severe obstacle to the use of III-V materials for optoelectronic emitters. In order to obtain high quality material with favorable electronic properties by CVD growth, a deposition temperature above 600 °C is preferred. Although MBE techniques can produce acceptable material at lower temperatures; there is a second, fundamental limitation on the use of III-V materials for optoelectronic emitters for monolithic integration with silicon based circuitry.

During growth of III-V materials, it is necessary to maintain an over pressure of the volatile group V species in order to preserve a stoichiometric surface. It is this requirement that precludes the use of III-V device with silicon-based circuitry. Phosphorus is used as a "dopant" during oxide deposition in silicon processing to change the flow temperature for glass layers used in passivation. For GaAs based devices, gallium poses a particular hazard to dopant profiles as it has an extremely high diffusion coefficient in silica⁷ and a solubility of $\sim 1 \times 10^{19} \text{ cm}^{-3}$ in silicon at 600 °C.⁵⁵

This leads to the conclusion that quantum confinement of silicon by a wide band gap material that can be deposited at a low temperature is a promising approach for achieving optoelectronic integration. Processing conditions should be below the silicon-aluminum eutectic temperature and should not introduce any rapid diffusing species that could alter doping profiles.

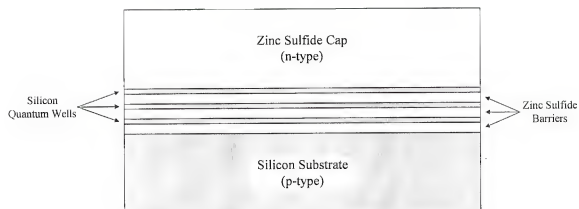


Figure 1-5. Proposed Zinc Sulfide/Silicon/Zinc Sulfide quantum well LED structure.

1.6 Proposed Research

Recently, several groups have reported blue shifts in PL measurements on silicon quantum well structures. Chen et al.⁵⁶ reported Raman shifts and PL shifts consistent with quantum confinement in Si:H/SiN_x:H quantum well structures. The structures were deposited using plasma assisted CVD followed by laser annealing. Saeta and Gallagher were able to fabricate silicon quantum well structures on SIMOX substrates using SiO₂ barriers. Room temperature PL measurements indicated the average thickness of silicon layers ranged from 20 to 80 Å.⁵⁷ Other groups have also reported blue shifted PL emissions. Baribeau, Lu and Lockwood⁵⁸ reported PL emission at wavelengths as short as 665 nm from Si/SiO₂ structures from quantum well structures grown using sequential MBE growth followed by UV-ozone oxidation. Samples with silicon quantum wells were grown with thicknesses between 10 and 300 Å. Steigmeier, et al.⁵⁹ grew Si/SiN_x structures using plasma-enhanced CVD (PECVD). PL measurements revealed emissions at 600 nm that were not seen in Si/SiN_x control samples without quantum well layers. PL emission in the range of 700 to 800 nm were seen in both samples and were attributed to surface states at the Si/SiN_x interface. While these studies have shown that silicon quantum well structures demonstrate the desired PL shift necessary in the development of an optoelectronic emitter, they all lack a means of efficient carrier injection into the quantum well regions. It is therefore doubtful that they will provide a direct path to monolithic optical integration with silicon-based technology.

1.6.1 Device Structure

Zinc sulfide is a promising candidate as a barrier material for quantum confined silicon. It is proposed to develop a zinc sulfide/silicon quantum well LED structure.

Zinc sulfide is nearly lattice matched to silicon (0.40% mismatch at room temperature) and has a room temperature band gap of 3.62 eV in the cubic phase. It can be grown by a variety of techniques at temperatures below the critical silicon-aluminum eutectic temperature. Additionally, it can readily be doped to yield low resistivity n-type material, providing a potential route to efficient carrier injection.

Since low resistivity p-type zinc sulfide has not yet been produced, the device will be grown on p-type silicon. Thus, the basic structure will be that of a p-i-n diode. Ohmic contacts will be made to the zinc sulfide cap and the silicon substrate to allow carrier injection.

Table 1-1. Properties of silicon and cubic zinc sulfide

Property	Silicon	Zinc Sulfide
Lattice Parameter (Å)	5.43072	5.4093
Band Gap Energy (eV)	1.12 (I)	3.62 (D)
Coeff. Thermal Expansion ($\times 10^6/^{\circ}\text{C}$)	2.33	7.85
Electron Affinity (eV)	4.79	3.17
Electron Effective Mass	0.19	0.525
Hole Effective Mass	0.40	0.58
Conduction Band Offset (eV)	1.62	-
Valence Band Offset (eV)	-0.88	-
Refractive Index	3.42	2.368
n-Type Dopants	P,As	Al,Cl,In
p-Type Dopants	B	-

1.6.2 Structure Requirements

1.6.2.1 Band alignment

One of the key issues that needs to be addressed at the abrupt interface of two semiconductors is how the band edges of the two materials line up at the interface. There are several possible configurations for band alignments as shown in figure 1-7. Each of

these alignments results in a band structure with unique properties relevant to device applications. Each band gap alignment can be described by the conduction and valence band offsets or alternatively for type I alignments, by the band gap distribution. The band gap distribution gives the percentage of the offset in the conduction band and the valence band in terms of the total offset between the two semiconductor materials.

Of the three types of band alignments, only the type I confines electrons and holes in the same spatial region. Type IIa alignments result in electron confinement in one material and hole confinement in another, resulting in the heterostructure equivalent of an indirect band gap semiconductor. Type IIb alignments result in the structural equivalent of a semimetal. Type III alignments result between a semiconductor and a semimetal. For the proposed device structure to function as an LED, it is an absolute requirement that the band alignment for the silicon/zinc sulfide system be of type I.

Although the band gap offsets are a vital piece of information for determining the performance of proposed device structures, they are unfortunately not easily measured or calculated. Many methods have been proposed for calculating band offsets in semiconductor heterojunctions.

In metals, the energy needed to eject an electron from the metal is known as the work function of the metal. The discovery that electron ejection from metals when exposed to ultraviolet light and its subsequent explanation was one of the key elements in establishing the quantum nature of the microscopic world. In semiconductor systems, the energy needed to eject an electron from a surface is that required to move an electron from the bottom of the conduction band to the vacuum level. This energy is analogous to the work function of a metal, but is commonly referred to as the electron affinity.

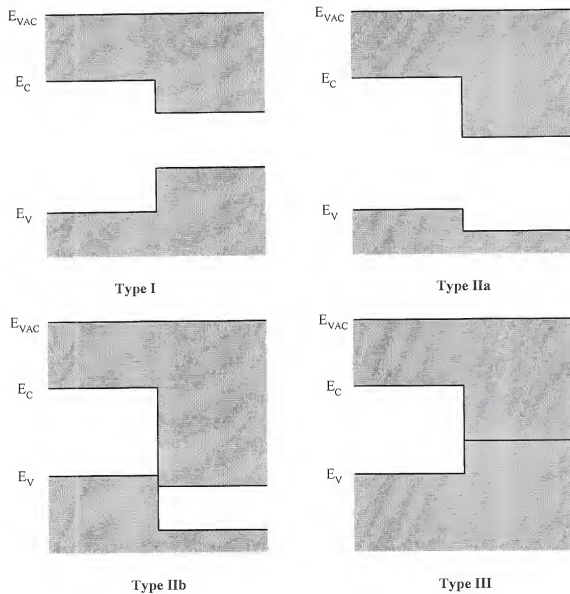


Figure 1-6. Three classes of band alignments for semiconductor heterojunctions.

Comparison of electron affinities is one method for estimating the band offsets in semiconductor systems. In this approach, the conduction band offset in a semiconductor heterojunction is set equal to the difference in the electron affinities, with the signs chosen such that the material with the smaller electron affinity has a higher conduction band at the interface. Simply stated:

$$\Delta E_C = E_{C2} - E_{C1} = \chi_1 - \chi_2$$

where χ is the electron affinity. This is known as the electron affinity rule. It was the first method proposed for determining conduction and valence band discontinuities.⁶⁰ Since the ionization energy Φ is equal to the sum of the electron affinity and the band gap of a material, it therefore follows that:

$$\Delta E_V = E_{V2} - E_{V1} = \Phi_1 - \Phi_2 = \chi_1 + E_{g1} - \chi_2 - E_{g2}$$

$$\therefore \Delta E_C + \Delta E_V = \Delta E_g$$

The electron affinity for silicon has been measured at 4.79 eV.⁶¹ A literature search was unable to find a report for the electron affinity of zinc sulfide, it was therefore estimated by plotting the barrier heights of various metals against the work function for each metal and fitting the results to a straight line with a unity slope.⁶² Using this method and the barrier height measurements of Aven and Mead⁶³ yields a value for the electron affinity of zinc sulfide of 3.17 ± 0.39 eV. This in turn, gives a conduction band offset of 1.62 eV and therefore a valence band offset of -0.88 eV for the silicon/zinc sulfide system. This represents a discontinuity distribution of approximately (65:35).

Another empirical method for estimating band offsets is called the common anion rule. It is based on the assumption that the valence band states of most semiconductors are composed of the anion atomic wavefunctions (it may also be inferred that the

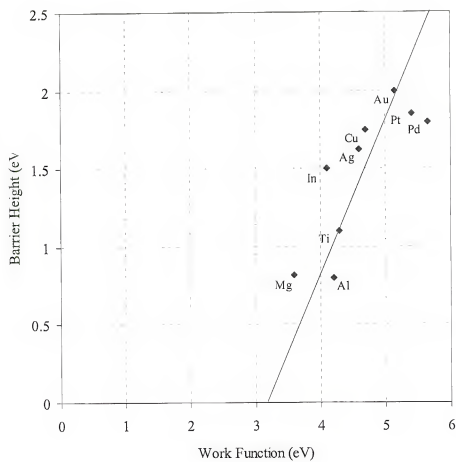


Figure 1-7. Schottky barrier heights of various metals on zinc sulfide, suggesting an electron affinity of 3.17 ± 0.39 eV.

conduction band states are primarily determined by the cation atomic wavefunctions).⁶⁴ Thus for a heterostructure made of semiconductors that share a common cation (e.g., ZnS/ZnSe) there should be little or no offset in the conduction band. As with the electron affinity rule the, band offsets determined by this rule should not be taken as hard facts. There are discrepancies with experimentally measured offsets.^{65,66} It should also be noted that in the case of common anion heterostructures the conduction band offset is larger than the valence band offset. The opposite is true for common cation heterostructures. The band offsets in the common cation ZnS/ZnSe system have been measured at $\Delta E_c = 0.23$ eV and $\Delta E_v = 0.86$ eV.⁶⁷ The common cation rule would estimate $\Delta E_c \approx 0$. While not ideal, the common anion rule does still help to provide a useful reference point when no other data is available.

Many band edge theories assume that there is an absolute energy associated with the conduction and valence bands of each semiconductor and that the band offsets are simply the differences between the corresponding absolute band energies of the semiconductor pair. Mathematically, this means that the theories assume:

$$\Delta E_v(A/B) = E_v(B) - E_v(A)$$

Such theories are called linear theories. If band edges are indeed absolute, the following relationship should hold:

$$\Delta E_v(A/B) + \Delta E_v(B/C) + \Delta E_v(C/A) = 0$$

This property is referred to as transitivity. It may also be used to test results for experimental accuracy and consistency. For example, the valence band offsets have been measured for the near lattice matched Ge/ZnSe/GaAs system.

$$\Delta E_v(\text{Ge/ZnSe}) + \Delta E_v(\text{ZnSe/GaAs}) + \Delta E_v(\text{Ge/GaAs}) =$$

$$-1.52 \text{ eV} + 0.96 \text{ eV} + 0.53 \text{ eV} = -0.03 \text{ eV}$$

Thus it can be shown that some systems do show transistivity. Using valence band to vacuum edge position data⁶⁸ and the band offset data for the ZnS/ZnSe system gives a valence band offset for the Si/ZnS system of:

$$\Delta E_v(\text{Ge/ZnSe}) - \Delta E_v(\text{Ge/Si}) + \Delta E_v(\text{ZnSe/ZnS}) = \Delta E_v(\text{Si/ZnS})$$

$$-1.40 \text{ eV} + 0.16 \text{ eV} + 0.23 \text{ eV} = -1.01 \text{ eV}$$

This value is in fair agreement with the value (-0.88 eV) determined by the electron affinity rule.

Unfortunately, while these relatively simple rules do work for some heterojunctions such as the GaAs/Al_xGa_{1-x}As system, it does not work for all semiconductor systems.^{69,70} In a real semiconductor heterojunction, there is always a charge transfer across the interface due to the dissimilar nature of the chemical bonds. This short ranged dipole can shift the relative band offsets from those predicted by the electron affinity rule. More sophisticated theories have tried to account for this interfacial charge transfer.

Other methods have been proposed that try to determine band discontinuities using first principal approaches. Harrison proposed determining band offsets by calculating the energy difference between the vacuum level and the valence band maximum using a linear combination of atomic orbitals (LCAO) theory.⁷¹ In contrast to the predictions of the electron affinity rule and transistivity, Harrison's theory predicts a valence band offset of -1.90 eV for ZnS/Si. While this value differs greatly from the previous ones, it does still predict a type I offset for the silicon/zinc sulfide

heterojunction. It should be noted that use of LCAO values result in greatest accuracy for junctions in which both sides are either polar or non-polar.⁷¹

Other authors have attempted to formulate theories to at least partly account for the effect of interfacial dipoles. Cardona and Christensen formulated their Dielectric Midgap Energy (DME) model along these lines.⁷² They estimated the midgap energy or charge neutrality level using average bulk band structure data. They were able to achieve fair agreement with the experimentally determined offsets for several systems. For the silicon/zinc sulfide system they predict a valence band offset of -1.7 eV, in close agreement with Harrison's LCAO method. While this method was developed to partially account for interfacial dipoles, it still assumes a non polar (110) zinc blende surface.

This brief survey points to the difficulty in determining the band discontinuities in a new semiconductor system. There are a number of variables that affect the accuracy of any given theory for predicting conduction and valence band offsets. A comprehensive review of offset prediction methods by Kroemer points out that, although excellent theoretical rules exist for semi-quantitative prediction of band offsets, no rule has yet been found with an overall accuracy of less than ± 0.20 eV.⁷³ He points to poorly understood second order effects such as interface charges and technology dependent offset variations as the limiting factors in offset theories.

More recently, work has been completed on experimentally determining the band offsets for the silicon/zinc sulfide system. Maierhofer et al.^{74,75} studied the silicon/zinc sulfide interface using Auger electron spectroscopy, photoelectron spectroscopy, and low-energy electron diffraction. The samples studied were MBE grown zinc sulfide on (111) silicon substrates. In previous studies on II-VI heterojunction formation, evidence was

found for interface reactions that can influence the magnitude of the valence band offset. Maierhofer's photoemission studies showed a valence band offset of $-0.70 \pm 0.2 \text{ eV}^{76}$. If a similar accuracy is assumed for the electron affinity rule and transistivity, the three values are in agreement and give an average conduction band offset of 1.64 eV (valence band offset -0.86 eV).

Although the quantum confinement calculations in Chapter 2 will be made using the average value of offsets as determined by Maierhofer, the electron affinity rule and transistivity ($\Delta E_c = 1.64 \text{ eV}$, $\Delta E_v = -0.86 \text{ eV}$), it should be emphasized here that every method reviewed predicts a type I band alignment. The relative importance of the magnitude of the conduction band offset will be discussed in more detail in Chapter 2.

Table 1-2. Summary of band offset measurements.

Method	$\Delta E_c \text{ (eV)}$	$\Delta E_v \text{ (eV)}$
Electron Affinity	1.62	-0.88
Transistivity/Common Cation	1.49	-1.01
Maierhoffer: Photoemission	1.80	-0.70
Average	1.64	-0.86

1.6.2.2 Ohmic contacts

An electrical contact is generally referred to as a contact between a metal and a non-metallic material whose function is either to block carrier injection (rectifying contact) or to enable carrier injection (ohmic contact). To explain the behavior of charge carriers at an interface, it is useful to understand the concept of the Fermi level (E_F). From a chemical perspective, the Fermi level of a material is the electrochemical potential or simply the chemical potential of electrons in a material. The Fermi level can be thought of as a reference level which represents the 50% probability level for being occupied by an electron. That is to say that an energy level equal to E_F has the same

probability of either being occupied by an electron or vacant. For metals the concept of the Fermi level is rather straight forward. For semiconductors, however, it is somewhat more complex. In a semiconductor the Fermi level typically lies within the band gap and is the equal to the equilibrium energy level that would exist if the valance and conduction bands where continuous.

When two materials with different Fermi levels are brought into contact there is a flow of charge carriers from one material into the other, resulting in a region of net positive charge on one side of the interface with the higher Fermi level and negative charge on the other. This process continues until the field generated at the interface increases to the point where there is no further net transfer. The electrons are now in equilibrium characterized by a constant E_F across the interface. The net effect of the generated field is to align the band structure of the two materials so that the Fermi level is continuous across the interface. The electric double layer that forms at equilibrium is referred to as the potential barrier and the potential across it is called the contact potential. For efficient carrier injection it is necessary to minimize this contact potential.

An ohmic contact between a metal and a semiconductor is defined as one in which the contact has a negligibly small impedance as compared with the series impedance of the bulk semiconductor. This implies that the free carrier concentration at the interface is much greater than that in the bulk of the semiconductor so that the contact may act as a reservoir of carriers. This condition leads to an alternative definition of an ohmic contact as one which creates an extended accumulation of charge carriers in the semiconductor at the semiconductor-metal interface.

For n-type semiconductors, there are two basic ways to make an ohmic contact. The first is to choose a metal with a sufficiently low work function (Φ_m) such that

$$\Phi_m < \chi_s + (E_c - E_f) = \Phi_s$$

where χ_s is the electron affinity of the semiconductor, E_c is the energy difference between the conduction band and the vacuum level for the semiconductor and E_f is the Fermi level of the semiconductor. The second is to heavily dope the semiconductor surface near the contact to make the potential barrier thin enough for efficient quantum mechanical tunneling. Both of these considerations will be taken into account in an effort to develop ohmic contacts to zinc sulfide as described in chapter 3. The important implication here is that metals with a low work function that are also n-type dopants in a semiconductor are the best candidates for making ohmic contacts.

1.6.3 Research Plan

1.6.3.1 Milestones

As stated previously, the proposed research project has as a goal the development of a silicon/zinc sulfide quantum well LED device. There are eight milestones that must be met prior to growth and testing of a device structure. They are:

- 1) Development of a low temperature method for cleaning silicon substrates.
- 2) Epitaxial growth of zinc sulfide on silicon.
- 3) Low resistivity n-type doping of zinc sulfide.
- 4) Ohmic contact formation to n-type zinc sulfide.
- 5) Demonstration of diode behavior in a p-type silicon/n-type zinc sulfide layered structure.
- 6) Low temperature epitaxial growth of silicon
- 7) Growth of epitaxial zinc sulfide/silicon/zinc sulfide multi-layer structures.

- 8) Demonstration of quantum confinement effects in from silicon/zinc sulfide quantum well structures.

1.6.3.2 Research plan

The research began with the first milestone stated above. The parameter space for epitaxial deposition of zinc sulfide on silicon wa investigated. The growth variables that were adjusted were deposition temperature, substrate preparation, zinc concentration and sulfur concentration. Confirmation of epitaxial growth was accomplished by X-Ray Diffraction (XRD), Transmission Electron Microscopy (TEM) and Atomic Force Microscopy (AFM).

Milestones three through five were closely related since growth of low resistivity material is difficult to demonstrate without ohmic contacts. Various schemes to produce ohmic contacts found in the literature were reviewed and tested. Hall measurements and modeling of the plasma region of FTIR spectra were used to verify doping levels. Current-Voltage (I-V) data verified the existence of both ohmic contacts and low resistivity material. Additionally I-V data was collected from a low resistivity n-type zinc sulfide sample grown on a p-type silicon substrate to verify formation of a p-n junction.

Milestones five and six also went hand in hand. Investigation of growth parameters focused on substrate preparation and growth temperature. Epitaxial growth was verified by XRD, TEM and AFM.

After completion of milestone six, growth of zinc sulfide/silicon/zinc sulfide structures on silicon substrates proceeded. Initial structures were examined by TEM to confirm epitaxial structures. Samples with thin silicon layers were examined by PL to

look for evidence of quantum confinement. Additional samples were grown on glass substrates and characterized by ultraviolet-visible light (UV-Vis) absorption.

After reaching these eight milestones, full device structure were grown and tested. Testing consisted of I-V data, PL and most importantly, electroluminescence (EL) measurements.

1.6.4 Growth Facilities

1.6.4.1 Growth system

The growth system used in this study is a modified Spire Model SPI-MOCVD 450 system. The reactor has a horizontal geometry with a tilted graphite susceptor. Heating is accomplished by rf-induction with temperature control provided by an Accufiber temperature controller connected to a thermocouple embedded in the susceptor. Growth temperature could be varied from 150 to 1200 °C. The system is capable of operating at growth pressures of 10 to 760 Torr.

The system is designed for up to four gas sources and four liquid alkyl and is equipped with a fast switching run-vent manifold to allow growth of structures with abrupt interfaces. Although the system is capable of using either nitrogen or high purity, palladium-diffused hydrogen as a carrier gas, only hydrogen was used in this study. Gas sources and alkyl sources are delivered to the reactor through separate inlets to minimize any potential pre-reactions.

Past experience has shown that a plasma will begin to form on and around the susceptor if the reactor pressure is reduced below about 30 Torr. The presence of plasma in the area of film deposition has been shown to lead to damaged substrate surfaces and results in films of poor crystal quality. Since uniformity tends to improve as the growth

pressure is reduced, all growths will be performed at 50 Torr to allow for process variations while still maintaining a pressure sufficient to inhibit plasma formation.

The system is also equipped with a turbo-pumped load lock with an ultimate pressure of 1×10^{-6} Torr to allow for loading of substrates without exposing the growth chamber to atmospheric contaminants. Substrates are loaded onto a quartz tray and are transferred to and from the growth chamber using a magnetically coupled manipulator arm.

The growth system is maintained in a class 100 clean room environment. Wet etching facilities are provided in the clean room and allow a minimal time delay between preparation of substrates and transfer to the system load lock.

For safety, the system cabinet is exhausted and maintained at a negative pressure with respect to the room. The system exhaust is sent to a burn box that uses a hydrogen-oxygen flame to oxidize any unreacted source materials. For additional safety, the system is monitored at multiple locations for hydrogen leaks and the manifold cabinet and burn box exhaust are sampled by a MDA hydride gas detection system to detect gas leaks or burn box malfunctions.

1.6.4.2 Sources

Diethyl zinc (DEZn) and hydrogen sulfide were used as sources for zinc sulfide growth. Although much of the research in the literature involves the use of dimethyl zinc (DMZn) as a zinc source, DEZn was used here due to its lower decomposition temperature. DEZn provides the additional benefit of lower carbon incorporation as it decomposes unimolecularly via β -hydride elimination.⁷⁷ N-type zinc sulfide has been grown using indium, chlorine, and aluminum as dopants. While investigating the

$\text{ZnS}_x\text{Se}_{1-x}$ system, Wright and Cockayne reported that aluminum was the most suitable dopant for sulfur rich compositions.⁷⁸ Based on this information, triethyl aluminum (TEAl) was chosen as an aluminum source for a n-type doping studies.

Due of the stability of traditional silicon precursor molecules, and the high sublimation pressure of zinc sulfide, the typical film deposition temperatures greatly different. Epitaxial silicon deposition usually takes place at a temperature above 1000 °C, while most reports on zinc sulfide growth have involved a growth temperature at or below 400 °C. In an attempt to lower the deposition temperature for silicon, disilane (Si_2H_6) was used as a silicon precursor molecule. Disilane is much more reactive chemically than silane (SiH_4)⁷⁹ and has recently been shown to have a significant probability of dissociative desorption on silicon surfaces at a temperature as low as 500 °C.⁸⁰ Disilane has a room temperature vapor pressure of less than 50 psi.⁸¹ Because of this low vapor pressure and its reactive nature, a 10% disilane-helium mixture was used in place of pure disilane.

CHAPTER 2

QUANTUM MECHANICAL CONSIDERATIONS

2.1 Historical Background

As the bulk of work in Chemical Engineering deals with units of measurement and physical laws that reside in the field of Classical Physics, it is perhaps best to pause here for a brief review of the history of Quantum Mechanics before continuing.

Towards the end of the nineteenth century, the general consensus among physicists was that almost all of the major principles of physics had been discovered and that little work remained in the field except for improving experimental designs and methods to determine "the next decimal place." This outlook appeared justified based on the tremendous advances that had been made in physics up to that time. Newton's Laws of Motion had done an excellent job of explaining the behavior of objects in the world around us. His mechanics had been brought to a high degree of both practical and theoretical sophistication by the work of Lagrange and Hamilton, yielding the mechanical theory of elasticity and hydrodynamics.⁸⁴ Experimental work by Joule and Count Rumford had clearly demonstrated the equivalence of mechanical work and heat.⁸⁵ Carnot had formulated what would later be known as the second law of thermodynamics. Gibbs's work following Carnot completed the development of thermodynamics in a form that has remained essentially unchanged to this day.⁸⁶ Working together, Maxwell, Gibbs, and Boltzmann had developed and formulated the kinetic theory of gases and statistical mechanics.

A debate over the nature of light (wave or particle) that dated back to the days of Newton was seemingly resolved as a result of the works of Fresnel and Young on interference phenomena. Their work led to a general acceptance of the wave theory of light over the particle or corpuscular theory of light. The first half of the nineteenth century also witnessed an intense period of discovery of electric and magnetic effects culminating in Maxwell's prediction of the electromagnetic nature of light.⁸⁷ His work not only unified the fields of optics, electricity, and magnetism, but also upon experimental verification by Hertz seemed to settle the argument over the nature of light once and for all.

The body of these accomplishments is considered to be the development of what is now known as "Classical Physics." Classical physics was extremely successful in explaining the phenomenon of the everyday world. Unfortunately, as science advanced and began to explore the extremes of nature, phenomena were encountered that could not be explained classically. Thus was born "Modern Physics." Modern physics is itself composed of two parts, relativity, which explains happenings at astronomical distances and extreme energies and quantum mechanics, which evolved in the course of searching for a way to explain and predict interactions and behavior at the extreme of atomic distances and low energies.

While relativity was the result of the insights of a single man, quantum mechanics was developed over a period of decades by many different people. It is also important to note that the very name of quantum mechanics implies a phenomenon that runs counter to the notions of classical physics; that energy is quantitized or exists only in integer multiples of a fundamental quantity.

The first clues that the world around us could not be fully explained by classical physics occurred when Rayleigh and Jeans attempted to derive the spectrum of black body radiation from first principles. It is important to realize that while real bodies do not emit and absorb all wavelengths of radiation equally, the spectrum emitted by many objects closely approximates that of an ideal or black body that absorbs and emits all wavelengths uniformly. The behavior of an object being heated is familiar to everyone. As it is heated, an object first begins to glow dull red then as it gets progressively hotter, it glows orange, yellow, white and eventually blue. There is a continual shift in the color of the light emitted from red through white and into the blue as the object is heated to higher and higher temperature. In other words, as the temperature increases, the frequency of radiation decreases. A plot of radiation intensity versus wavelength at different temperatures for a black body is shown in figure 2-1.

Several important observations were made concerning the nature of black body radiation with respect to temperature. The first was made by Wilhelm Wien in the late 1800s. Analyzing the spectrum of many objects at different temperature, he noted that the wavelength corresponding to the maximum intensity seemed to decrease as the temperature increased. Indeed, he found that the relationship could be successfully described by:

$$T\lambda_{\text{max}} = \text{constant}$$

This expression is known as Wein's Displacement Law and has been verified numerous times. Repeated experiments have yielded a value of 2.9×10^{-3} mK for the constant.

Another observation of the spectra of black body radiation was made by Josef Stefan. He noted that the total power emitted as radiation from a hot body was

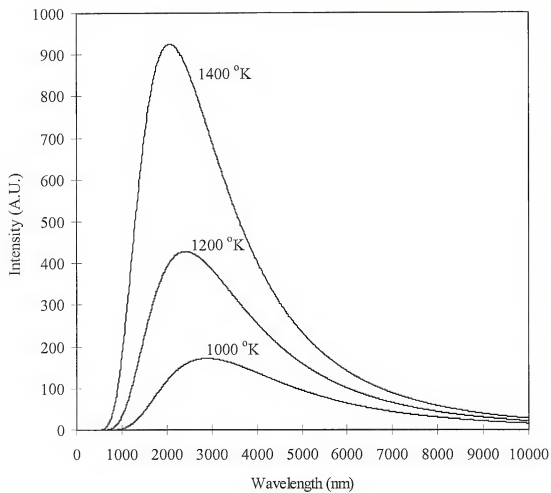


Figure 2-1. Intensity distribution of radiation from a black body versus wavelength for several temperatures.

superlinear with respect to temperature. He noted that it is in fact proportional to the fourth power of the temperature. In other words that:

$$P = \sigma T^4$$

The equation is known as Stefan's Law; the constant σ is known as the Stefan-Boltzmann constant and has a value experimentally determined value of $5.6697 \times 10^{-8} \text{ W/m}^2 \text{ }^\circ\text{K}^4$.

These two laws contained within them important clues to the nature of matter, although this was not obvious until later. It was expected that a true explanation of blackbody radiation would explain these laws and allow some form of them to be derived from first principles.

Lord Rayleigh with assistance from James Jeans took a classical approach to the problem and imagined the spectrum of radiation emitted from an object as resulting from the motion of electrons in the constituent atoms of the material body. They treated the electrons as a collection of harmonic oscillators, one for each possible frequency of light. This led to the assumption that the occurrence of light of frequency ν (wavelength $\lambda = c/\nu$) is due to the excitation of the oscillator of that frequency. Since the average energy of an oscillator at a temperature T is given by kT where k is Boltzmann's constant, the energy density in the wavelength range λ to $\lambda + d\lambda$ is the number of oscillators per unit volume in that range, $dN(\lambda)$ multiplied by their average energy. An explicit calculation of N gives the Rayleigh-Jeans Law:

$$\rho(\lambda) = \frac{8\pi kT}{\lambda^4}$$

where ρ is the energy per unit volume per wavelength, k is Boltzmann's constant and T is the absolute temperature. Unfortunately (for Rayleigh and Jeans) as λ decreases, $\rho(\lambda)$

increases without ever passing through a maximum, implying that even at room temperature, oscillators of short wavelength and high energy (corresponding to ultraviolet light, x-rays and even gamma rays) are excited. According to classical physics any object at even room temperature should glow in the dark. In fact, it implies that there can be no darkness because everything should be glowing brightly.

This nonsensical result was termed the ultraviolet catastrophe. Many people attempted to derive the correct equation believing Rayleigh and James had made some kind of error or mistake, but the end results were the same. The equation is correct according to classical physics.

Wien took a different approach, concentrating on the importance of entropy in the process of blackbody radiation.^{88,89} The expression he derived did an excellent job of fitting the spectrum at short wavelengths and was, overall, a tremendous improvement over the Rayleigh-Jeans result, but it underestimated the radiation intensity at longer wavelengths. His result was:

$$\rho(\lambda) = \frac{c_1}{\lambda^5} \exp(-c_2 / \lambda T)$$

The constants c_1 and c_2 were adjusted to fit the observed blackbody spectra at short wavelengths. The best fits were obtained for $c_2 = c_1/8k$. Wein's expression still, however, underestimated the intensity of radiation at longer wavelengths. This was the first instance of a phenomenon that classical physics was unable to explain theoretically. Solving the problem of blackbody radiation required an entirely new approach.

In 1900 Max Planck investigated this problem from the perspective of thermodynamics. As Rayleigh and Jeans before him, Planck assumed that the radiation emitted by a heated body was due to the oscillations of electrons in the atoms that

constituted the bulk of the material. He was the first to derive an expression that fit the intensity of black body radiation over the entire spectrum. He began by noting that while the Rayleigh-Jeans expression fit the data for long wavelengths very well, it failed for short wavelengths. He also noted that the opposite was true for Wein's expression. He derived an expression that was an interpolation of the two expressions and discovered that it fit the entire spectrum!⁹⁰ He then proceeded to rationalize his expression using an entirely new approach. His departure from the classical approach stemmed from his treatment of the energies of the harmonic oscillators. Implicit in the derivation of Rayleigh and Jeans was the assumption that the energies of the oscillators could take on any value. Planck used the assumption that the energy for a given oscillator was an integral multiple of the frequency. In other words that the energy was given by $E = nh\nu$, where n is a positive integer and h is a proportionality constant. In this framework, a beam of light can be thought of as a stream of particles, each having an energy of $h\nu$. The key result is that high frequency oscillators are not excited unless they can acquire an energy of at least $h\nu$. Therefore oscillators for frequencies $\nu > kT/h$ are not excited and emit no radiation. The net effect of this implication is to minimize or eliminate the contributions of higher frequency oscillators. Using this assumption and statistical arguments, Planck was able to derive the following equation for the distribution of radiation:

$$\rho(\lambda) = \frac{8\pi hc}{\lambda^5} \left[\frac{\exp(-hc/\lambda kT)}{1 - \exp(-hc/\lambda kT)} \right]$$

where h is a proportionality constant now known as Planck's constant. For short wavelengths the term $hc/\lambda kT$ is large and $\exp(-hc/\lambda kT) \approx 0$, reducing to Wein's

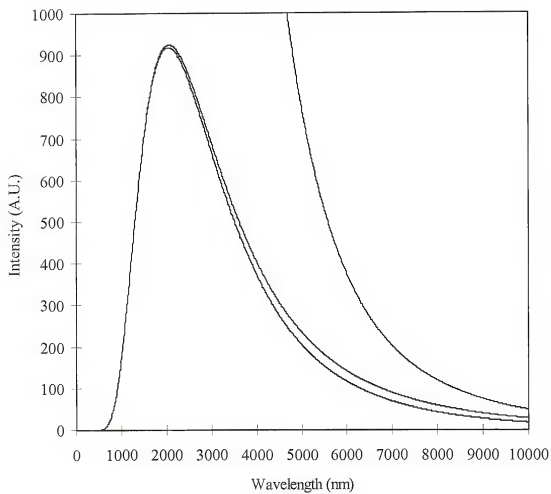


Figure 2-2. Comparison of observed black body radiation spectra with results of Rayleigh-Jeans, Wien and Planck.

expression for blackbody radiation. On the other hand for long wavelengths $hc/\lambda kT$ is small and the exponential terms can be approximated by $1 - hc/\lambda kT$, allowing the Planck expression to be reduced to the Rayleigh-Jeans result. This result is also obtained if the Planck constant, h , is set to zero. The complete expression fits experimental data very well. The value of Planck's constant may be determined by adjusting its value to give the best fit. A comparison of the Rayleigh-Jeans expression, Planck's expression, and experimental data is shown in figure 2-2. Planck was also able to account for Wein's Displacement Law and Stefan's Law. Taking the first derivative of the Planck expression with respect to λ and setting it equal to zero yields:

$$T\lambda_{\max} = \frac{hc}{5k} = 2.8776 \times 10^{-3} \text{ mK}$$

in excellent agreement with experiment. Integrating for $\lambda = 0$ to $\lambda = \infty$ gives:

$$P = \left(\frac{2\pi^5 k^4}{15c^2 h^3} \right) T^4 = \left(\frac{5.6703 \times 10^{-8} \text{ W}}{\text{m}^2 \cdot \text{K}^4} \right) T^4$$

which is also agrees well with experiment.

The important implication of the agreement Planck found between his theory and observations was that oscillators can not possess arbitrary amounts of energy. Planck had found the first hint that while the notions and inherent assumptions of classical physics did an excellent job of explaining most of the world around us, there were some instances where they failed dramatically. The concept of quantization of energy was a radical departure from the thinking of classical physics and its application to other problems soon showed it to be an important principle of nature.

Due to the ad hoc nature of the initial derivation of his expression, it was felt that while Planck's Law did an excellent job of describing black body radiation, the principle

of quantized energy was not the true mechanism behind the phenomenon. Most physicists felt that eventually, the true explanation would be found and the idea of a quantum nature could be laid to rest.⁹¹ This did not prove to be the case. Soon enough, other phenomena were found to be explained by quantization.

In the late nineteenth century while conducting experiments to confirm Maxwell's theory about the electromagnetic nature of light, Heinrich Hertz discovered that ultraviolet light causes electrons to be ejected from a metallic surface.⁹² This ejection of electrons from the surface of a metal is known as the photoelectric effect.

Classical physics explained the photoelectric effect in the following manner. Electromagnetic radiation was viewed as an electric field oscillating perpendicularly to its direction of propagation. The intensity of the radiation is proportional to the square of the electric field, so that as the intensity increases, so does the amplitude of the oscillating electric field. Since the electrons on the surface of a metal oscillate with the electric field, as the intensity of the field increases, they begin to vibrate more and more violently. Eventually their vibrations become so violent that they are ejected from the surface of the metal and travel with a kinetic energy that is proportional to the intensity (amplitude) of the field.

Three important fundamental observations were made concerning the photoelectric effect that classical physics was unable to explain.

- No electrons are ejected regardless of the frequency of light, unless a threshold value, characteristic of the metal is exceeded.
- The kinetic energy of the ejected electrons is linearly related to the frequency of the light.
- Even at low intensities electrons are ejected immediately if the light is above the threshold frequency.

Einstein found he was able to explain the photoelectric effect by using a quantum argument similar to Planck's. He began by assuming that light consisted of discrete quanta of energy ($E = h\nu$) now known as photons. Using a simple conservation of energy argument, he was able to show that the kinetic energy of the ejected electrons was equal to the energy of the incident photons minus the energy required to remove an electron from the surface of a metal (the work function or the ionization energy of the metal).⁹³ This not only successfully explained the photoelectric effect, it also implied that the wave theory of light was in serious need of revision. Diffraction experiments had shown that light behaved as a wave, but the photoelectric effect could only be explained if light consisted of a stream of particles!⁹⁴

Additional work by Einstein relating to heat capacities at low temperatures and by Compton dealing with the scattering of x-rays from electrons established the quantum nature of microscopic systems.⁹⁵ Both the photoelectric effect and the Compton effect showed that light has particle-like properties in addition to its behavior as a wave. There seemed to be no way to adequately explain the behavior of light using a framework assuming either particle or wave characteristics by themselves.

In the mid 1920's experiments by Davisson and Germer on the diffraction of electrons from a crystal showed variations in intensity characteristic of optical interference experiments in which light waves were allowed to constructively and destructively interfere with each other. This experiment which has since been repeated with other particles including molecular hydrogen and helium clearly demonstrated that in some sense, particles have wave-like properties. Now physicists not only had waves (light) that behaved as particles, but also they found particles behaving as waves!

This seeming conundrum is one of the central tenets of quantum mechanics: that on an atomic scale the concept of something behaving solely as a particle or as a wave leads to a woefully inadequate viewpoint. At atomic scales, the concepts of particle and wave are no longer black and white, but blur together into a gray area where particles behave as waves and waves behave as particles. This concept was formalized by de Broglie when he suggested that any particle with a given momentum (p) would have in some sense an associated wavelength (λ) given by $\lambda = h/p$.⁹⁶ This expression was confirmed for electrons in the Davisson-Germer experiments and for photons in the Compton effect. It is of great importance for electronic devices and structures with length scales in the range of nanometers. Any time the physical dimension(s) of a system are reduced to the magnitude of this wavelength, quantum effects become important and the particle will no longer behave classically.

Taking the de Broglie relation as a starting point and abandoning the concept of a localized particle required viewing the particle as existing as a type of probability distribution not unlike the amplitude of a wave. The concept of a wave function (Ψ) was introduced to replace the classical concept of a trajectory. Quantum mechanics evolved from the requirement of setting up schemes for calculating and interpreting Ψ .

2.2 The Schrödinger Equation

2.2.1 Background

In 1926 Schrödinger proposed an equation which when solved would give the wavefunction for any system. This equation is the counterpart in modern physics of Newton's Laws of Motion for classical mechanics. Newton's Laws of Motion were inspired postulates which when solved yield the trajectory of a particle. Similarly, the

Schrödinger equation is a fundamental axiom of quantum mechanics which when solved gives the wavefunction of a particle. Both Newton's Laws and the Schrödinger equation can not be derived from basic principles.⁹⁷ They do, none the less, provide real and valid information regarding the behavior of real particles. In its most general form, the Schrödinger equation can be written as:

$$\left[\left(\frac{-\hbar^2}{2m} \right) \nabla^2 + V \right] \Psi = i\hbar \left(\frac{\partial \Psi}{\partial t} \right)$$

where $\hbar = h/2\pi$, ∇^2 is the Laplacian for the system, V is the potential energy and m is the mass of the particle.⁹⁵ The version of the Schrödinger equation most commonly used in calculations is the one-dimensional, time independent form:

$$\left(\frac{-\hbar^2}{2m} \right) \left(\frac{d^2 \Psi}{dx^2} \right) + V\Psi = E\Psi \quad (2-1)$$

In the case of a particle in a region where the potential is zero everywhere the $V\Psi$ term drops out and the equation may be easily solved to yield:

$$\Psi = e^{ikx} = \cos(kx) + i\sin(kx), \quad k = \sqrt{\frac{2mE}{\hbar^2}}$$

Since $\cos(kx)$ (or $\sin(kx)$ for that matter) represents a wave of wavelength $\lambda = 2\pi/k$ and since the particle energy is entirely kinetic, and $E = p^2/2m = k^2\hbar^2/2m$ it can be shown that the momentum of the particle is related to the wavelength of the wavefunction by:

$$p = k\hbar = \left(\frac{2\pi}{\lambda} \right) \left(\frac{h}{2\pi} \right) = \frac{h}{\lambda}$$

which is the de Broglie relation. In the case of a particle whose motion is not restricted, the Schrödinger equation yields an experimentally verified conclusion! For particles in a region of uniform non-zero potential similar arguments lead to the conclusion that the de

Broglie wavelength of a particle will be related to its kinetic and potential energies by the relation:

$$\lambda = \frac{h}{\sqrt{2m(E - V)}}$$

It is important to note that the greater the energy of the particle, the shorter the de Broglie wavelength. This also implies that the smaller an area a particle is confined in, the greater its energy.

An important general aspect of the wavefunction that remains well defined even when it is difficult to speak in terms of wavelength is the curvature. When the wavefunction is sharply curved implies that it has a short wavelength and therefore high energy. The opposite is also true. This association of curvature and wavelength will help when interpreting the behavior of energy levels later on.

The last step in understanding the wave equation of a particle is the interpretation of its wavefunction. The Schrödinger equation is a second order differential equation and has an infinite number of solutions. In the case of a free particle in a region of uniform zero potential, it was found that $\Psi = e^{ikx}$. It can also be shown that $\Psi = Ae^{ikx}$ is a solution where A is a real constant. If there are no restrictions on the value of A, then there are also no restrictions on the value of k and hence the energy of the particle is arbitrary. By restricting the value of A, the admissible values of k are restricted, hence leading to the quantization of energy.

The most common interpretation of the wavefunction was first proposed by Born and is based on the analogy with the wave theory of light in which the amplitude of the electromagnetic wave is interpreted as the intensity. The Born interpretation is that the square of the wavefunction (or $\Psi^* \Psi$ if the wavefunction is complex) is equal to the

probability of finding the particle at a given point in space. The value of the pre-exponential term is then fixed by the requirement that for a given wavefunction : $\Psi = N e^{ikx}$

$$N^2 \int_{-\infty}^{+\infty} (\Psi^* \Psi) dx = 1 \quad \text{or} \quad N^2 = \frac{1}{\int_{-\infty}^{+\infty} (\Psi^* \Psi) dx} \quad (2-2)$$

since, logically the particle must be somewhere. From this point on, it shall be assumed that wavefunctions include a normalization factor such that

$$\int_{-\infty}^{+\infty} (\Psi^* \Psi) dx = 1$$

The Born interpretation imposes several restrictions on the acceptable solutions to the Schrödinger equation. The first requires that the wavefunction be finite everywhere. Any infinities would yield a normalization constant of zero which would imply that the normalized function is zero everywhere except for where it is infinite. It also requires that Ψ be single valued. Any wavefunction with more than one value at a point would imply that there is more than one possibility of finding a particle at that point. This is of course nonsensical. Additionally, the form of the Schrödinger equation itself imposes restrictions on the nature of acceptable wavefunctions. Being a second order differential equation implies that both Ψ and its first derivative are continuous and smooth.

2.2.2 Solutions for Infinite Potential Barriers

Solutions to the Schrödinger equation take on many forms depending upon the problem involved. In this case the concern is with a quantum well structure. A quantum well structure involves the creation of a potential well for electrons and holes in a semiconductor system with widths on the order of the de Broglie wavelength of the

particles involved. Typical scales are on the order of 100\AA or less. Solutions to the Schrödinger equation for such a system allow the calculation of the effective band gap of the quantum wells by giving information on the energy of confinement for electrons and holes.

The simplest case solution to the Schrödinger equation involves the classic particle in a box. A particle is imagined to be in a one dimensional region with zero potential. It is bounded at $x = 0$ and $x = L$ by potential barriers that are infinitely high. It can be shown that the solution given these conditions is of the form:

$$\Psi(x) = \sin\left(\frac{n\pi x}{L}\right), \quad n = 1, 2, 3, \dots \quad (2-3)$$

Substitution back into equation 2-1 allows calculation of the energy levels for the particle. These energy levels are given by:

$$E = \frac{h^2 n^2}{8mL^2} \quad (2-4)$$

where n is the quantum number, h is Planck's constant and m is the particle mass. As will be shown later, this solution is of limited value, but it is useful for pointing out many of the general properties of solutions involving the energy of particles in quantum systems. The first is that again, as predicted, the energy is quantized. The second is that as the quantum number of the energy levels increases, the energy increases on the order of n^2 . The third is that as the mass of a particle increases, its energy decreases. The same is also true of the degree of confinement. As the region a particle is confined to is increased, its energy is decreased. In reality however, infinite potential barriers are never realized and the system will have a finite barrier height (δ).

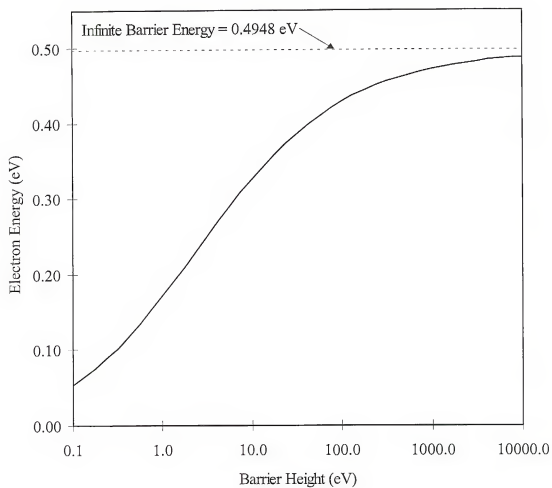


Figure 2-3. Confinement energy for an electron in a 20 Å silicon quantum well as a function of barrier height.

Another important consideration that this solution neglects is the mass of the charge carriers. Due to the periodic potential present in semiconductors the apparent or effective mass of charged particles (electrons or holes) is different from the actual mass. The effective mass can be calculated by measuring the acceleration of an electron or hole in an electric field. The force acting on the electron or hole can be calculated from the intensity of the field and the charge on the particle using: $F = qV$ where q is the charge on the particle and V is the strength of the electric field. Once the acceleration is known, the effective mass of the particle is then simply found using $m^* = F/a$, where m^* is the effective mass. Alternatively, if enough information about the band structure of a semiconductor is known, the effective mass can be calculated as follows. Given that $a = dv/dt = (dv/dk)(dk/dt)$, $F = \hbar dk/dt$ and that $v = (dE/dk)/\hbar$, it follows that $m^* = \hbar^2 (d^2 E/dk^2)^{-1}$.

The effect of mass differences in the well and barrier complicates the problem some, but analytical solutions are still possible. The form of the wave function inside the well and in the barrier remain unchanged, but the continuity constraints require that $\Psi_w = \Psi_b$ at the boundaries of the well, and that the first derivatives of the wavefunctions at the barrier satisfy:

$$\frac{1}{m_b^*} \left(\frac{\partial \Psi_b}{\partial x} \right) = \frac{1}{m_w^*} \left(\frac{\partial \Psi_w}{\partial x} \right) \quad (2-5)$$

Where m_b^* and m_w^* are the effective masses in the barrier and well material respectively. Applying these conditions to the problem result in two expressions for particle energy corresponding to symmetrical and assymmetrical solutions to the wave equation.

$$\tan\left[\frac{L}{2}\sqrt{\frac{8m_w^*\pi^2 E}{h^2}}\right] = \left[\frac{m_w^*(\delta-E)}{m_b^*E}\right]^{1/2} \quad (2-6)$$

corresponding to the symmetrical solutions of Ψ ($n = 1, 3, 5, \dots$) and

$$\cot\left[\frac{L}{2}\sqrt{\frac{8m_w^*\pi^2 E}{h^2}}\right] = -\left[\frac{m_w^*(\delta-E)}{m_b^*E}\right]^{1/2} \quad (2-7)$$

corresponding to the asymmetrical solutions of Ψ ($n = 2, 4, 6, \dots$). Note that for $m_w^* = m_b^*$ and $\delta \rightarrow \infty$ the two equations reduce to equation 2-4.

2.2.4 Tunneling

As mentioned previously, quantum confinement of a particle by potential barriers with a finite height has two important effects on the particle. The first effect has already been discussed in some detail: the ground state energy of the particle is increased. The magnitude of this increase is based on: the dimension of the region the particle is confined in, the height of the barriers confining the particle, the particle's effective mass in the well and barrier material. This effect has important implications for quantum well electronic devices. It allows an extra degree of freedom in tuning the band gap of a material. Depending on the composition and width of a quantum well and the barriers in a device structure, it is possible to effectively increase the band gap in a controlled manner. Additionally, the confinement of electrons and holes in a fixed region increases the probability of recombination and for direct band gap materials, the efficiency of light production.

In a typical quantum well device, electrons and holes are injected into the quantum well(s) where they recombine to produce light. The width of the quantum wells and the height of the barriers surrounding it are critical parameters for controlling the

wavelength of the light emitted. By using equation 2-6 (or 2-7) it is possible to estimate the confinement energy for electrons and holes in the quantum well. These energies are then added to the band gap energy of the quantum well to determine the effective band gap and therefore the expected wavelength emitted from the device. Since efficient optical emission typically requires material of high crystalline quality, the selected composition of the barriers (and therefore the height of the well barriers) is often severely limited. This in essence reduces the parameters available to tune device wavelengths to the width of the quantum wells.

Barrier width also plays another important role in the development of device structures. Recall that for any quantum well system with finite potential barriers, there exists a small, but finite chance of finding the particle inside the barrier. If the barriers are thin enough so that the wavefunction enters another region of zero potential before it decays to zero, it will begin to oscillate again just as it did inside the quantum well where it originated. This means that a particle may be found outside the area it was originally confined to even though it did not have enough energy to hop over the potential barriers surrounding it. This 'leaking' through classically forbidden areas is known as tunneling.

By evaluating the wavefunction for a particle inside a barrier it is possible to derive an expression for the tunneling probability of a particle given the particle's effective masses, the barrier height and the width of the barrier. It can be shown that the transmission probability will be proportional to a transmission factor T_t which is given by:

$$T_t = \frac{2\gamma}{\sqrt{(1-\gamma^2)\sinh^2(\kappa L) + 4\gamma^2\cosh^2(\kappa L)}} \quad (2-8)$$

where $\kappa = \sqrt{8m_b^*2(\delta - E)/\hbar^2}$ and $\gamma = \sqrt{\frac{m_b^*E}{m_w^*(\delta - E)}}$

The actual probability will depend on the area of the well the particle is in initially and can be calculated by normalizing the wavefunction according to the Born interpretation. A plot of the transmission coefficients for electrons and holes in a silicon quantum well with zinc sulfide barriers is shown in figures 2-5 and 2-6.

2.3 Device Implications

2.3.1 Confinement Energies

Using the equations derived above, it is now possible to predict the confinement energies of electrons and holes in a silicon quantum well with zinc sulfide barriers. It was noted in Chapter 1 that there is some disagreement on the value of the conduction band offset for the silicon/zinc sulfide system. In order to investigate the importance of the conduction band offset a series of calculations were performed using the parameters listed in Table 1-1 and the method detailed in appendix A. The emission edge of silicon quantum wells was calculated as a function of the well width and conduction band offset. It is interesting to note that the effective band gap of the silicon quantum wells is almost independent of the conduction band offset. Except for the extreme cases of no conduction band offset or no valence band offset, electron confinement and hole confinement are almost equally effective in increasing band gap energy. Although this may seem counterintuitive, careful inspection of the equations derived earlier in this chapter do provide an explanation.

The effective mass for holes in silicon is much larger than for electrons. This would imply that the quantum confinement effects for electrons should be greater than

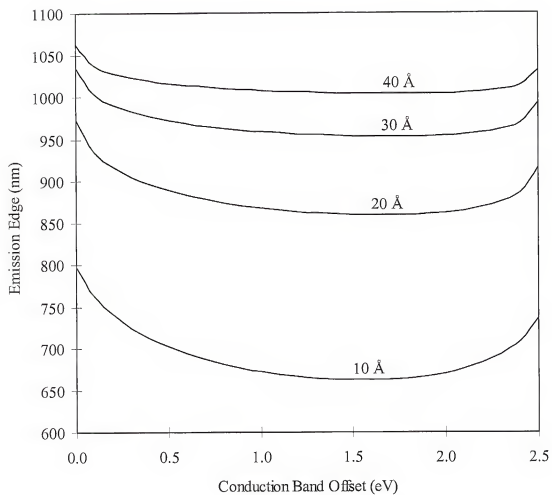


Figure 2-4. Emission edge for a silicon quantum well with carriers confined by zinc sulfide barriers.

that for holes. For the case of infinite barriers or for equal mass in the well and the barrier, this is true. However, the situation changes when the effective mass is different in the barrier and well material.

To begin, it is useful to first define the mass ratio as the ratio between the effective mass in the barrier to the effective mass in the well. Next, recall equation 2-6.

$$\tan \left[\frac{L}{2} \sqrt{\frac{8m_w^* \pi^2 E}{h^2}} \right] = \left[\frac{m_w^* (\delta - E)}{m_b^* E} \right]^{1/2} \quad (2-6)$$

This equation has no analytical solution, but can be solved by numerical or graphical methods. Solving graphically involves plotting both the left hand and right hand sides of the equation and locating the intersection. Increasing the mass ratio has the effect of shifting the right hand side of the equation to lower values. Since the tangent function increases monotonically between vertical asymptotes, the point of intersection will be shifted to a lower energies as the mass ratio increases.

The mass ratio for electrons in the silicon/zinc sulfide system is 2.105 while the mass ratio for holes is 1.105. As a result, the lower mass ratio for holes tends to offset the higher effective mass for holes and increases the confinement energy. Thus the effective band gap for silicon quantum wells is essentially constant over a large range of offsets.

It is important to note that all of the methods reviewed for predicting the band alignment for the silicon/zinc sulfide system as well an experimental measurement result in conduction band offsets (including errors) between about 0.4 and 1.8 eV. Even over this rather wide range the sum of the confinement energies for electrons and holes is essentially constant.

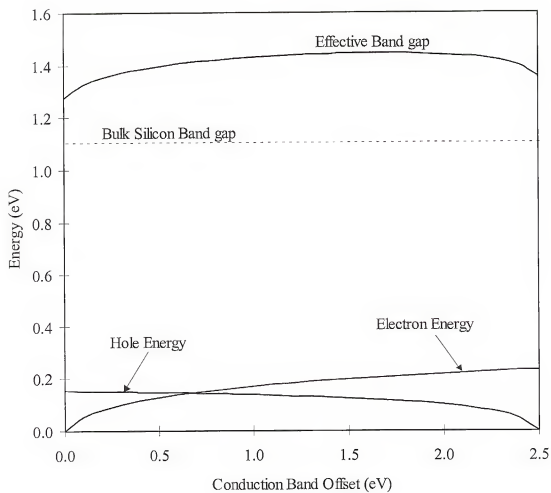


Figure 2-5. Electron, hole and effective band gap energies for a 20 Å silicon quantum well with zinc sulfide barriers.

In view of the results shown in figure 2-4, the quantum width should be less than 40 Å in order to obtain emission wavelengths reasonably above the band gap of bulk silicon. Emission at visible wavelengths will require well widths below 20 Å.

2.3.2 Tunneling Probabilities

There are three basic mechanisms to transport holes to the device structure from the silicon substrate: bulk transport, quantum tunneling and Fowler-Nordheim⁹⁸ tunneling. Zinc sulfide is known to have an extremely low hole mobility. Due to the difficulty in obtaining low resistivity p-type material, few experimental measurements have been made at room temperature. Using copper doped samples, Aven reported a hole mobility of 5 cm²/V-sec at 400°C.⁹⁹ Hole transport in zinc sulfide is further hampered the ease at which vacancies form to electrically compensate any donor or acceptor impurities that are incorporated during growth.¹⁰⁰ These vacancies provide ample scattering sites or traps that can severely limit charge carrier transport in zinc sulfide. The problem is not as severe for electrons as evidenced by the numerous studies that have reported successful growth of low resistivity bulk and thin film samples of n-type material. Despite this difficulty, it is none the less possible to estimate diffusion lengths for holes in zinc sulfide. While studying electroluminescence in zinc sulfide powders, Fischer estimated the diffusion length of holes to be on the order of 300 Å.¹⁰¹ This places a strict limitation on the maximum thickness of the quantum well structure if the device is to rely on bulk transport of holes to the silicon quantum wells.

The effectiveness of quantum tunneling will depend on the effective mass of the charge carriers, their energy, the barrier height and the barrier width. The tunneling probabilities for electrons and holes in silicon through a zinc sulfide barrier are shown in

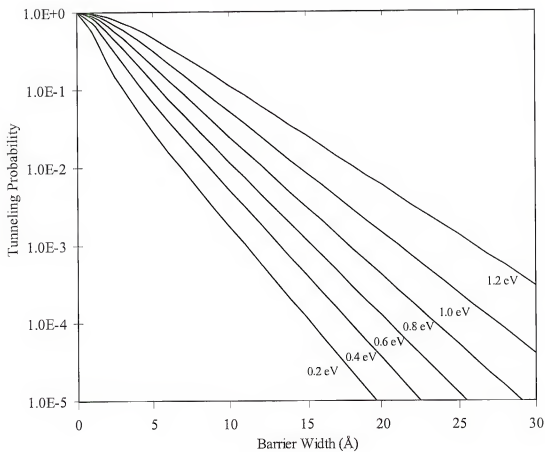


Figure 2-6. Transmission probabilities for electrons in silicon through a zinc sulfide barrier as a function of barrier width.

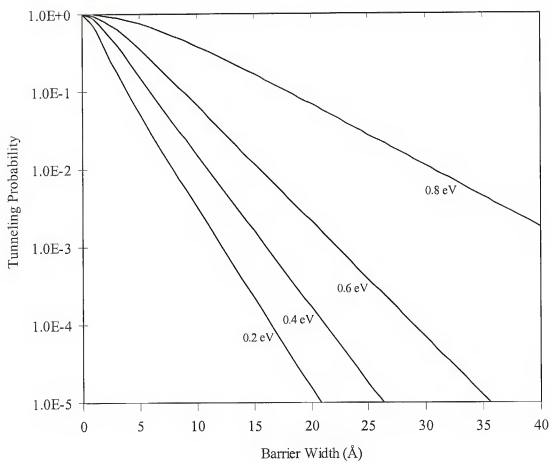


Figure 2-7. Transmission probabilities for holes in silicon through a zinc sulfide barrier as a function of barrier width.

figures 2-6 and 2-7. Although the effective mass for holes in silicon is nearly twice that of electrons, the tunneling probability for holes through a zinc sulfide barrier is much greater. This is due primarily to the lower barrier height (0.86 eV) for holes compared to electrons (1.64 eV).

The transmission probabilities for electrons and holes calculated above is for a single particle encountering a barrier. The actual tunneling rate through the zinc sulfide barriers will depend on the flux of particles reaching the barrier and the applied voltage. This makes calculation of the actual tunneling rate an extremely difficult problem to solve. Increasing the applied voltage increases the energy of the incident particles and generates potential gradients across the barriers. The net effect is that the transmission probability increases rapidly with applied voltage. As the potential gradient increases, the tunneling mechanism begins to change to Fowler-Nordheim tunneling. As the strength of the electric field is increased, the potential gradient across the barrier increases as well. As a result, the distance a particle must tunnel in order to penetrate the barrier decreases. Thus it is in essence tunneling through a triangular barrier.

Tunneling rates are difficult to take calculate. Equation 2-8 given the transmission probability for a single particle encountering a barrier. Applying a forward bias to the device will result in the accumulation of charge carriers at the barriers. Here the tunneling rate will depend on the distribution of particles near the barrier and their energy. Particles inside the quantum wells will oscillate until they recombine or tunnel through one of the surrounding barriers.

Taking these considerations into account, the width of the zinc sulfide barriers in the device should be on the order of 30 to 50 Å in order to allow for efficient tunneling.

Wider barriers will tend to increase the device resistance and hence operational voltage. They will also decrease the optical output of the device. This is well below the thickness limit required for bulk transport for holes to be effective.

2.3.3 Critical Thickness

In homoepitaxy, except for minor differences due to doping, the lattice parameter of the substrate and film are the same and there is no stress or strain in the deposited film. This is not the case for most heteroepitaxial systems. Except for lattice matched ternary or quaternary systems, there is a difference between the lattice parameter of the substrate and the film. This difference is described by a parameter known as the lattice misfit (f) given by:

$$f = \frac{(a_{os} - a_{of})}{a_{os}} \quad (2-9)$$

where a_{os} is the lattice parameter of the substrate and a_{of} is the lattice parameter of the film. This lattice misfit will result in the accumulation of tensile stress in the film if the substrate has a larger lattice parameter or compressive strain if the substrate has a smaller lattice parameter. As the thickness of the overlying film increases, the amount of accumulated stress or strain also increases until a critical value is reached and the film relaxes through the generation of misfit dislocations.

The basic theory for describing the elastic/plastic changes in a bilayer structure was developed in the late 1940s.¹⁰² It attempted to account for the accommodation of misfit between two lattices rather than being a theory of epitaxy. It predicted that epitaxial layers with a misfit of ~9% or less would grow pseudomorphically. As the film thickness increases, the total strain also increases and eventually exceeds the energy

associated with a relaxed structure consisting of arrays of misfit dislocations separating regions of relatively good fit.

For the case of a real film growing epitaxially on a substrate, the region of pseudomorphic grow extends only up to a critical film thickness (T_c) beyond which misfit dislocations are introduced. Matthews^{103,104} derived an expression for the critical thickness by minimizing the sum of the elastic strain energy (per unit area) and the dislocation energy (per unit area) with respect to the film strain. His approach yielded an expression for the critical film thickness given by:

$$T_c = \frac{b}{8\pi(1+\nu)f} \ln\left(\frac{T_c}{b} + 1\right) \quad (2-10)$$

where ν is Poisson's ratio and b is the dislocation Burger's vector.

Numerous experiments conducted by Bean on $\text{Si}_x\text{Ge}_{1-x}$ films on silicon have extended tests of the theory into the realm of large lattice misfits.¹⁰⁵ His studies showed that films considerably thicker than those predicted by equation 2-10 can be grown in practice. The reason for this is that Matthew's theory is based on an equilibrium analysis and strained layer films are not necessarily at equilibrium. Extended dislocation arrays do not form spontaneously with well defined spacings as Matthews assumed. Instead, they nucleate individually over an area determined by a certain width (w) and a unit depth, over which atoms above and below the slip plane are displaced by at least $b/2$. Relating this energy density to the energy supplied for nucleation determined by Matthews, Bean was able to derive an expression for the critical thickness given by:

$$T_c \approx \frac{(1-\nu)b^2}{(1+\nu)8\pi wf^2} \ln\left(\frac{T_c}{b}\right) \quad (2-11)$$

where w is a fitting parameter arbitrarily set equal to five $\langle 110 \rangle$ lattice spacings. Equation 2-11 was shown to yield an excellent fit when compared to experimental data for $\text{Si}_x\text{Ge}_{1-x}$ films.

Using the elastic constants for silicon and zinc sulfide and the method of Bean yields a critical thickness of 5980 Å for zinc sulfide on silicon and 5750 Å for silicon on zinc sulfide. Even using the rather pessimistic results of Matthews results in critical thicknesses of 86 Å and 87 Å for zinc sulfide on silicon and silicon on zinc sulfide respectively. Since the silicon quantum wells and zinc sulfide barriers are less than 50 Å thick, these results indicate that even under equilibrium conditions, both the quantum wells and the barriers should be free of misfit dislocations.

2.3.4 Structure Specifications

Summing up the results discussed above, the requirements for the various component layers for the device can now be used to specify the device structure. Based on confinement energy calculations, the well widths should be below 40 Å in order for the emission edge to be sufficiently above the band gap of bulk silicon to use silicon photodetectors. Well widths below 20 Å are required for visible light emission.

Tunneling rates are strongly dependent on the barrier thickness. In order to allow reasonable tunneling rates, the zinc sulfide barriers should be on the order of 40 to 50 Å thick. This sets the base period of the structure at 60 to 90 Å. Since the hole diffusion length in zinc sulfide is on the order of 300 Å, the number of periods in the structure should be less than 6 if hole transport in zinc sulfide is to be taken advantage of to improve device performance.

As was stated in chapter 1, the substrate and cap should be p-type silicon and n-type zinc sulfide respectively due to the difficulties associated with p-type doping in zinc sulfide. (Å)

Table 2-1. Material and structure specifications for Si/ZnS MQW LED.

Structure component	Material	Dopant	Thickness
Substrate	p-type silicon	Boron	> 500 μm
Barrier	undoped zinc sulfide	N/A	40 to 50 Å
Well	undoped silicon	N/A	< 40 Å
Cap	n-type zinc sulfide	Aluminum	~ 1 μm

CHAPTER 3 ZINC SULFIDE ON SILICON GROWTH

3.1 Substrate Preparation

Substrates used in this portion of the study were commercial 150 mm silicon wafers. Both (100) and (111) 4° off towards nearest (110) orientation were used. As the growth system was not designed for use with substrates larger than 25 mm in diameter, the wafers were cut into ~ 10 x 10 mm pieces using a dicing saw. Following dicing, the substrates were degreased using warm trichloroethane, acetone and methanol for five min each, followed by a de-ionized (DI) water rinse.

After degreasing, the substrates were then etched for 60 sec in a 6:1 BOE solution, followed by a 30 sec overflowing DI rinse. The substrates were then etched for 30 sec in a 10:1 DI:HF solution and then blown dry with filtered nitrogen from a liquid nitrogen boil off. After this preparation, the substrates were immediately transferred to the load lock. The load lock was evacuated to below 1×10^{-4} Torr and back filled to atmospheric pressure with palladium diffused hydrogen. The load lock was then re-evacuated to 1×10^{-5} Torr and was again back filled with palladium diffused hydrogen to the growth pressure (50 Torr) and transferred to the growth chamber. The susceptor was then brought to growth temperature and the substrates were dosed with H_2S for 3 min prior to initiating zinc sulfide deposition.

This final step is important to reduce anti-phase domain (APD) formation. Elemental semiconductors such as silicon and germanium crystallize in a so-called

diamond lattice. In a diamond lattice all of the constituent atoms are tetrahedrally coordinated. The entire structure can be thought of two interpenetrating face centered cubic lattices. Since the crystal structure is composed of a single element, all of the lattice sites are equivalent. In compound semiconductors, the equivalent cubic structure is referred to as a zinc blende or sphalerite structure. In an AB compound with a sphalerite structure, all of the A atoms occupy one fcc sub lattice and all of the B atoms occupy the other. The atoms are still tetrahedrally coordinated, but each lattice site is no longer equivalent. Only sites on each sublattice are equivalent.

Anti-phase domain formation is a fundamental problem in the growth of a polar compound on a non-polar substrate. The nucleation stage of growth is critical in minimizing APD formation. For zinc blende compound semiconductors, both the (100) or (111) crystal planes consist of alternating layers of A and B atoms. It was first proposed in the early 1980s that growth on these orientations has the potential for producing APD free material. Calculations^{105,106} and numerous experiments on the growth of GaAs on silicon have shown that it is possible to produce APD free material on both (111) and (100) misoriented substrates.^{107,108,109,110}

The basic premise of the experimental work on growth of APD free material is to expose the surface to one element first. If growth is initiated without this pre-exposure, the sublattice of the first monolayer will be randomly occupied by both types of atoms. Won et al. studied the interface charge polarity of a GaAs/Si p-n junction and was able to show that even submonolayer coverage of gallium or arsenic prior to growth is sufficient to produce APD free material.¹¹¹ It was theorized that the lower overall crystal energy in APD free material was the driving force for APD reduction in the case of submonolayer

exposures. Although Won found that both dosing the substrates with either gallium or arsenic resulted in APD free material, most studies of the GaAs/Si and GaAs/Ge systems utilize arsenic pre-exposure prior to growth. In the current study, the substrates were only dosed with sulfur prior to growth. Silicon-sulfur bonds are known to be energetically more favorable than silicon-zinc bonds.⁴⁴ Jones, Esson and Singer have reported that formation of a sulfur-rich silicon surface is an essential step for epitaxial growth of zinc sulfide on silicon and that no growth occurs without this layer.¹¹² For this reason, no growths were attempted dosing the surface with zinc prior to growth.

A potential concern during deposition of any compound semiconductor is the accumulation of one of the component elements on the surface. This can be a particular problem when depositing GaAs. The vapor pressure of elemental gallium is orders of magnitude lower than that of arsenic. This necessitates the use of V/III ratios much greater than unity to prevent formation of gallium droplets on the film surface. When heated, zinc sulfide is known to sublime congruently.¹¹³ Simple heating is therefore unlikely to result in significant degradation of the crystalline quality of a deposited film. Additionally, the equilibrium vapor pressures of zinc and sulfur over zinc sulfide are more than an order of magnitude lower than that of the pure elements.^{114,115} Thus, any excess sulfur or zinc on the surface will re-evaporate into the gas phase.

3.2 Zinc Sulfide Growth

3.2.1 Growth Results

Deposition of zinc sulfide on silicon was studied using the parameter ranges listed in table 3-1. The reactor pressure during growth was maintained at 50 Torr and the deposition time was held constant at 60 min.

Sample thickness was determined by cross-sectional SEM (XSEM). It was found that the growth rate was almost independent of temperature below 650 °C, demonstrating that mass-transfer limited growth is operative in the reactor over an extremely wide range of temperature. No significant difference was noted between the growth rates on (100) and (111) substrates, further supporting the argument for a mass transfer limited growth regime. XRD showed that zinc sulfide films were single crystal at all growth temperatures studied. Epitaxial growth was confirmed by TEM.¹¹⁶ Representative micrographs are shown in figure 3-8.

Table 3-1. Reactor operation parameter space for zinc sulfide deposition.

Variable	Range
DEZn Mole Fraction ($\times 10^4$)	0.2 to 1.0
H ₂ S Mole Fraction ($\times 10^4$)	30 to 100
Growth Temperature (°C)	300 to 700
Total Hydrogen Flow Rate (slm)	4.0
Growth Pressure (Torr)	50

At 700 °C, the growth rate showed a dramatic decrease. This drop in growth rate occurred because the vapor pressure of zinc in the bulk gas phase dropped below the equilibrium vapor pressure of zinc over zinc sulfide.¹¹⁵ Increasing the growth pressure or the DEZn inlet mole fraction would increase the vapor pressure of zinc in the gas phase and should allow mass transfer limited growth at an even higher deposition temperature. Due to the fact that it was possible to maintain mass-transfer limited growth at a temperature of 650 °C, which is well above the maximum process temperature limit of 577 °C discussed in Chapter 1, no experiments were performed using higher DEZn inlet mole fractions or higher reactor pressures.

Additional growths were carried out, maintaining the DEZn molar flow rate constant while varying the value of the VI/II ratio from 20 to 120. These growths were

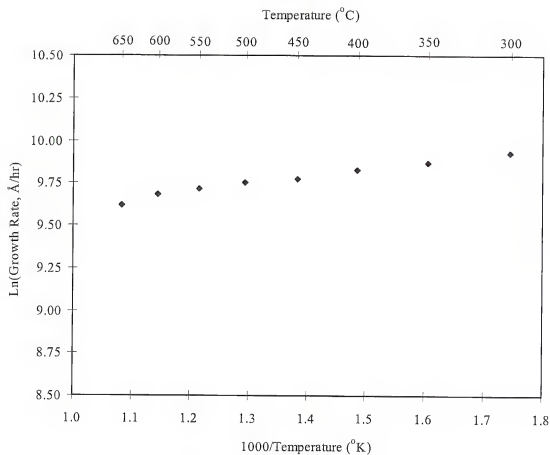


Figure 3-1. Arrhenius plot of zinc sulfide growth rate data indicating a mass transfer limited growth regime.

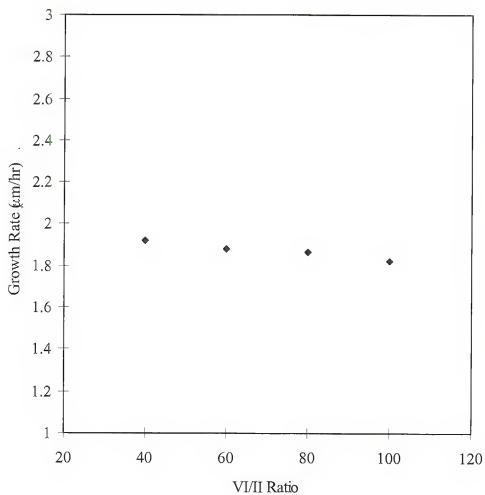


Figure 3-2. Effect of VI/II ratio on growth rate for zinc sulfide on silicon.

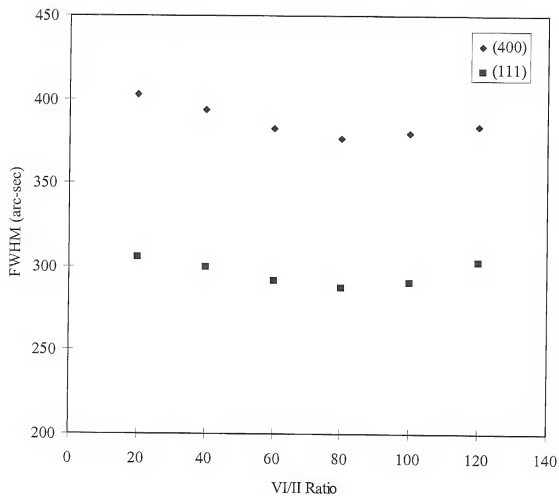


Figure 3-3. XRD FWHM of (400) and (111) reflections for zinc sulfide on silicon as a function of VI/II ratio.

carried out at a temperature in the range of 400 to 500 °C. Changes in the VI/II ratio had no significant effect on the growth rate, but it did have a slight effect on the crystallinity as measured by XRD. The narrowest FWHM values were obtained using a VI/II ratio of 80. It was generally observed that the films grown on (111) substrates possessed a higher crystalline quality (narrower FWHM) than films grown on (100) substrates.

3.2.2 Zinc Sulfide Growth Analysis

It is interesting to note that there is not a strong consensus about substrate orientation among the authors who have reported successful epitaxial growth of zinc sulfide on silicon. It has been variously reported that single crystal silicon can be grown on either (100)^{42,44,117} or (111)^{118,119} silicon substrates by different authors. In light of the stringent cleaning requirements for epitaxial growth of any material on silicon substrates, it is not surprising that early reports of zinc sulfide growth yielded polycrystalline material. The lack of success in producing epitaxial material using growth initiated by simultaneous introduction of zinc and sulfur precursors is also not surprising if the established techniques for epitaxial growth of GaAs on silicon reviewed at the beginning of this chapter are considered.

The surprising success in obtaining epitaxial material on both (100) and (111) substrates, in contrast to literature reports, is believed to be related to the choice of the sulfur precursor and the decision to dose the substrate surface with sulfur prior to growth. The substrate etching procedure outlined is not expected to generate an oxygen free surface. As stated previously, a temperature in the neighborhood of 1000 °C and a reducing hydrogen atmosphere are required to thermally desorb any remaining oxide. Yet the processing conditions prior to growth do not even begin to resemble those

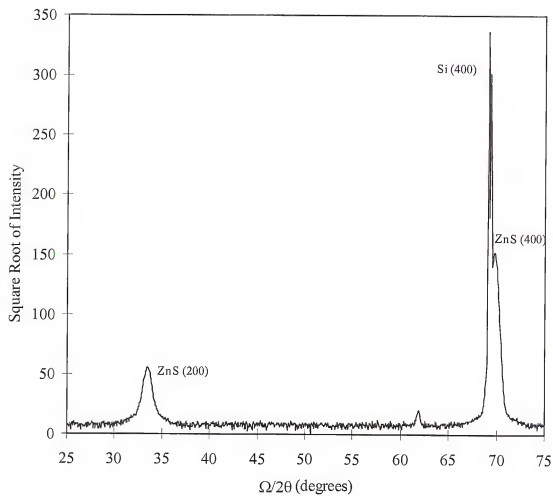


Figure 3-4. Low resolution X-ray diffraction scan of zinc sulfide on (100) silicon.

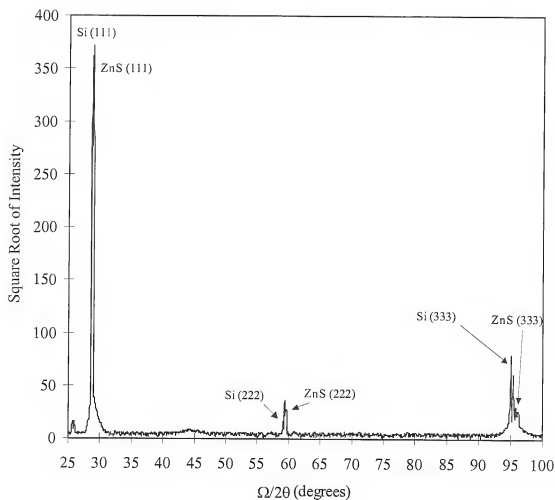


Figure 3-5. Low resolution X-ray diffraction scan of zinc sulfide on (111) silicon.

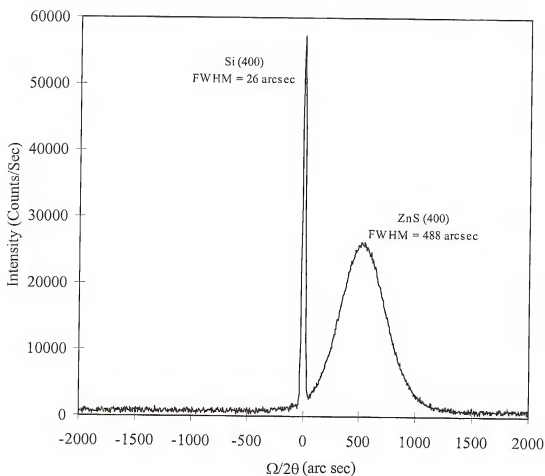


Figure 3-6. High resolution X-ray diffraction scan of zinc sulfide on (100) silicon.

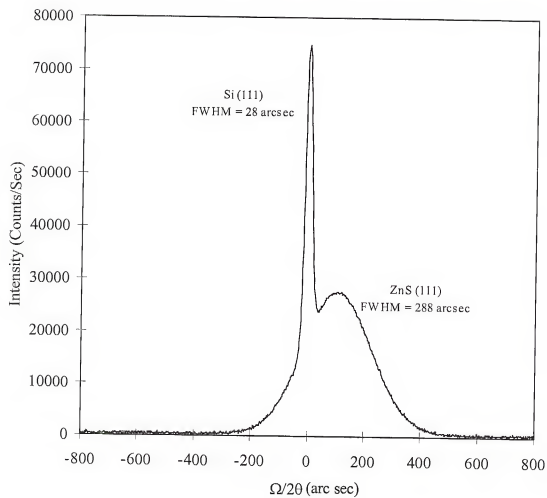


Figure 3-7. High resolution X-ray diffraction scan of zinc sulfide on (111) silicon.

required for oxide desorption. While studying zinc sulfide growth by MBE, Yongnian, Hickey and Gibson used a substrate preparation similar to that used in this study.⁴⁴ They theorized that sulfur atoms reacted with the residual oxygen on the silicon surface to form a volatile S-O complex. Tests using a H₂S gas beam for 30 min at 450 °C prior to growth resulted in films with the highest crystalline quality zinc sulfide reported.

Thermodynamic calculations were made using the ThermoCalc software package for the Si-H-O and the Si-S-H-O systems in the temperature range of 400 to 1400 °C. There was no significant difference in the sum of the oxygen species in the gas phase. However, the addition of sulfur to the system resulted in a substantial increase in the quantity of silicon species in the gas phase. Most of this increase could be attributed to the generation of SiS_x species. The equilibrium concentrations of the gas phase S-O species was negligible at temperatures below 800 °C. It is therefore unlikely that a volatile S-O complex is responsible for the improved surface reported by Yongnian et al. It is theorized that sulfur acts as a catalyst to promote the formation of SiO at lower temperature. This catalytic activity allows generation of an oxygen free surface at substantially lower temperatures than those used for thermal oxide desorption.

This theory is supported by an observation made during this study. The initial zinc sulfide growths yielded single crystal material. After this initial success, however, the experiments begin to produce polycrystalline material. A variety of different substrate preparations were used in an attempt to reproduce the initial results. All failed to produce single crystal material. Finally, thermal desorption at atmospheric pressure was attempted as a last resort. Characterization by TEM revealed an amorphous layer at the silicon/zinc sulfide interface. It was noted that the thickness of this layer increased



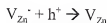
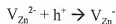
Figure 3-8. Low (left) and high resolution TEM micrographs of zinc sulfide/silicon interface showing epitaxial deposition.

with desorption time. A careful inspection of the system revealed a small leak (helium leak rate 2.3×10^{-7} cm³/sec) in the alkyl switching manifold that was introducing oxygen into the process stream. After the leak was repaired, the substrate preparation procedure outlined at the beginning of this chapter once again yielded single crystal material. It was also noted that essentially any preparation that did not leave a thick oxide layer on the silicon substrate would produce single crystal material.

3.3 Dopant Studies

3.3.1 Aluminum Doping

Perhaps the greatest difficulty in obtaining low resistivity zinc sulfide lies in the fact that donor impurities tend to generate zinc vacancies which act as acceptors. Hence



they are easily compensated. In bulk samples, low resistivity zinc sulfide is typically obtained by the use of the so-called zinc extraction treatment. This treatment involves immersing a sample in molten zinc or zinc-aluminum or zinc-gallium alloys at temperatures in the neighborhood of 1000 °C for 10 to 100 hr. This heat treatment is then followed by a rapid quenching and results in bulk specimens with resistivities of 10 Ω cm or less.^{120,121,122} Variations of this technique have been reported for thin films. Kaufman and Dowbor were able to obtain resistivities of 1 to 10 Ω cm by annealing zinc sulfide films in zinc vapor at 900 °C.¹²³ Even earlier work by Williams in 1966 resulted in low resistivity n-type zinc sulfide using high temperature vapor diffusion of Al, Cl, or In.¹²⁴

Unfortunately, this technique and its variations are liable to be of little use in the development of a zinc sulfide based light emitting device that is to be integrated with

silicon-based processors. The high diffusivity of dopants at a temperature of 1000 °C would degrade dopant profiles to the extent of destroying device structures. It is also probable that the diffusion of silicon at these temperatures would degrade quantum well layers to the point of generating silicon doped layers of zinc sulfide.

An additional consideration in the quest for a method of obtaining low resistivity material is the abruptness of the technique. As mentioned earlier, effective quantum confinement of electrons and holes relies on a barrier material with a low net carrier concentration. Additionally, it has been noted that since the diffusion length of holes in zinc sulfide is on the order of 300 Å, the active layer of the device structure should not be of greater thickness. By their nature, diffusion techniques are not capable of providing the abrupt doping profiles needed for the proposed device structure. The capping layer of zinc sulfide must be low resistivity in its as deposited state or converted to low resistivity material without the use of high annealing temperature.

In 1979 Olsen et al. succeeded in producing as deposited low resistivity, n-type zinc sulfide films using coevaporation of zinc sulfide with aluminum or indium.¹²⁵ Conductive films were deposited at a substrate temperature ranging from ambient to 300 °C. The best results were obtained by coevaporating an aluminum-zinc alloy followed by annealing in nitrogen at 450 °C for 6 min. All films deposited using coevaporation of aluminum were conducting as deposited with resistivities of 100 to 200 Ω cm. Post deposition annealing resulted in resistivities of less than 10 Ω cm.

Low resistivity aluminum doped zinc sulfide has also been reported for MOCVD grown material using trimethyl aluminum (TMAI) and triethyl aluminum (TEAI). Yamaga et al. reported resistivities of 1 to 10 Ω cm in as deposited materials using

dimethyl zinc (DMZn), TMAI, and hydrogen sulfide as source materials.¹²⁶ The effects of substrate temperature and Al/Zn ratios were studied. The lowest resistivity material was obtained for at a substrate temperature of 300 °C and Al/Zn ratios above 0.05.

Earlier work using the Lewis acid-base adduct diethyl zinc-diethyl sulfide (DEZn-DES), hydrogen sulfide, and TEAl as the precursor materials resulted in as deposited material with resistivities below 10 Ω cm.¹²⁷ The highest qualities material was obtained at a growth temperature of 350 °C and an Al/Zn ratio of 4×10^{-3} . These conditions resulted in material with a resistivity of 0.03 Ω cm and a net carrier concentration of 8×10^{18} cm⁻³. Growth rates were reported to be between 1 and 2 μ m/hr. It was also noted that the surface morphology of the films were not influenced by aluminum doping.

Following these studies, aluminum-doped zinc sulfide was grown in this study using DEZn, hydrogen sulfide and TEAl as precursor materials. The substrate temperature was set at 350 °C. Reactor conditions were adjusted to give a zinc sulfide growth rate of 1.6 μ m/hr. Using an Al/Zn ratio of 0.03, specular films were obtained with morphologies identical to those of undoped material.

3.3.2 Contact Studies

The ability to make ohmic contacts to n-type zinc sulfide is of crucial importance to the proposed device structure. While it has been relatively easy to make ohmic contacts to many n-type III-V semiconductors, it has been difficult to repeatably achieve ohmic contacts to zinc sulfide. This is partly due to the problems associated with obtaining low resistivity material and partly due to the low electron affinity of zinc sulfide. In order to obtain ohmic contacts to n-type material, it is generally necessary to use a metal with a work function less than the electron affinity of the semiconductor¹²⁸ or

to heavily dope the surface region near the contact to make the potential barrier at the interface thin enough for efficient quantum mechanical tunneling.¹²⁹

The low electron affinity of zinc sulfide stated in Chapter 1 (3.17 eV) indicates that it would be difficult to make electrical contacts to n-type material, but a low work function metal that also acts as a donor in zinc sulfide should be sought. Table 3-2 lists several metals that have commonly been used as contact materials and their work functions. A cursory inspection reveals that indium, aluminum and gallium are promising candidates for ohmic contacts to n-type zinc sulfide. A search of the literature on zinc sulfide reveals several different recipes have been discovered that successfully yield ohmic contacts. A summary of methods is detailed below.

Table 3-2. Work function of common contact metals.

Metal	Φ (eV)
Au	5.31
Ag	4.54
Al	4.25
In	4.12
Ga	4.20

Smith and Aven have reported successful formation of ohmic contacts to bulk zinc sulfide doped with aluminum by etching in hot (250°C) pyrophosphoric acid immediately followed by scribing on contacts with indium wire that had been dipped in mercury. Additional indium is added to the contacts and the samples were subsequently annealed at 350°C in a hydrogen atmosphere.^{130,131} Hall measurements revealed donor concentrations greater than $10^{18}/\text{cm}^3$ and indicated that aluminum forms a level 0.18 eV below the conduction band. Although a hot acid etch was used in these studies prior to

the application of contact materials, later investigations found that no surface etching was necessary to make ohmic contact.

Blount et al. studied ohmic contacts and came to the conclusion that low electron affinity metals (indium and gallium) were not sufficient by themselves for making ohmic contact to zinc sulfide due to its low electron affinity. They determined that the diffusion of indium and gallium into zinc sulfide would be the dominant factor in determining the nature of the contact.¹³² They found that when using indium-gallium alloys, ohmic contacts could be made after annealing at temperatures between 300 and 500°C for three to five minutes in hydrogen. Higher annealing temperatures were reported to degrade contacts.

Williams also studied contact mechanisms to aluminum and chlorine doped zinc sulfide using sputtered films of indium tin oxide followed by annealing under two atmospheres of argon at 700°C to diffuse indium in the zinc sulfide. A final anneal at 375 to 400°C in air yielded ohmic contacts.¹³³ The problem of achieving ohmic contact to aluminum doped zinc sulfide has been studied by several other authors, with each coming to slightly different conclusions on the best material and procedures to make the contact.^{126,134,135,136,137}

In light of the methods described in the literature, a study was performed using indium, indium-gallium alloys, and indium-mercury as contact materials was performed. The alloy compositions listed are given on a weight percentage basis. As deposited aluminum doped samples were used. No chemical etching was performed prior to depositing the contact metals. All samples were annealed in forming gas (10% H₂, 90% N₂) for five to ten min at temperatures between 300 and 400°C. The contacts were

characterized after annealing by current-voltage (I-V) measurements. A linear I-V trace was used as the basis for determining ohmic contacts.

A summary of results is given in Table 3-3. Indium contacts were made by pressing a clean piece of cold indium against the surface. The indium was then heated with a soldering iron to wet the surface. The two indium-gallium alloys used are liquid metals at room temperature and must be 'painted' onto samples surfaces to ensure wetting. The indium mercury contacts were made by dipping a clean piece of indium into mercury and then scratching the sample surface. Additional indium was added to the scribed contacts prior to annealing.

Table 3-3. Results of contact annealing study.

Material	Anneal Temperature (°C)	Anneal Time (min.)	Result
Indium	300	5	non-ohmic
Indium	300	10	non-ohmic
Indium	350	5	non-ohmic
Indium	350	10	non-ohmic
Indium	400	5	Ohmic, high resistance
Indium	400	10	Ohmic, high resistance
In:Ga (25:75)	300	5	Ohmic, high resistance
In:Ga (25:75)	300	10	Ohmic
In:Ga (25:75)	350	5	Ohmic
In:Ga (50:50)	300	5	Ohmic
In:Hg	300	5	non-ohmic
In:Hg	300	10	non-ohmic
In:Hg	350	5	non-ohmic
In:Hg	350	10	non-ohmic
In:Hg	400	5	Ohmic, high resistance
In:Hg	400	10	Ohmic

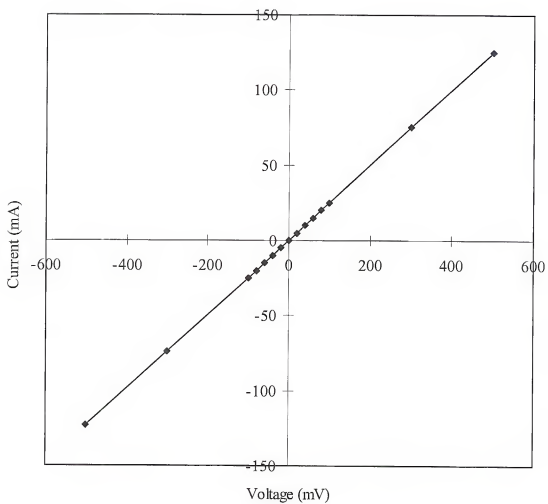


Figure 3-9. Current-Voltage characteristics for aluminum doped zinc sulfide sample with (50:50) Indium-Gallium alloy contacts, after annealing at 300 °C for 5 min.

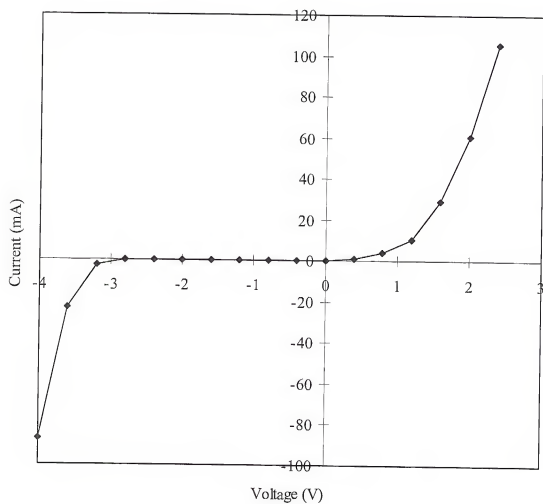


Figure 3-10. Current-Voltage characteristics for p-silicon/n-zinc sulfide diode. Silicon contact was made using indium dot. Zinc sulfide contact was made using a 50:50 Indium-Gallium alloy followed by annealing at 300 °C for 5 min.

The results show that ohmic contact are most easily formed using a 50:50 indium-gallium alloy. This alloy was used to make ohmic contact to samples grown on silicon and glass substrates for electrical characterization.

With ohmic contacts in place, the resistivity of a sample can be determined by measuring the resistance between two contacts. If the distance between the contacts is known, along with the area of the contacts, the resistivity (ρ) can be found from:

$$\rho = R \frac{A}{L}$$

where R is the measured resistance, A is the area of the contacts and L is the distance between the contacts. The resistivity of aluminum doped thick films was found to be between 2 and 6 Ω cm. This compares favorably with results reported in the literature.^{138,139,140}

3.3.3 Carrier Concentrations

Net carrier concentrations of zinc sulfide on silicon films were determined using Fourier Transform Infrared Spectroscopy (FTIR). FTIR has been shown to provide a rapid non destructive means of measuring film thickness and determining free carrier concentration.¹⁴¹ Carrier concentrations are determined by using the Fresnel equation to model the reflectance and transmission of light for a thin film on a thick substrate. Provided the electrical and optical properties of a film are known it is possible to model the predicted FTIR spectrum of a film for a given thickness and carrier concentration.¹⁴² As an experimental technique, the film thickness and free carrier concentration can be adjusted until the predicted plasma minimum and the overall shape of the modeled spectrum match that obtained by FTIR. The results are most accurate if either the film

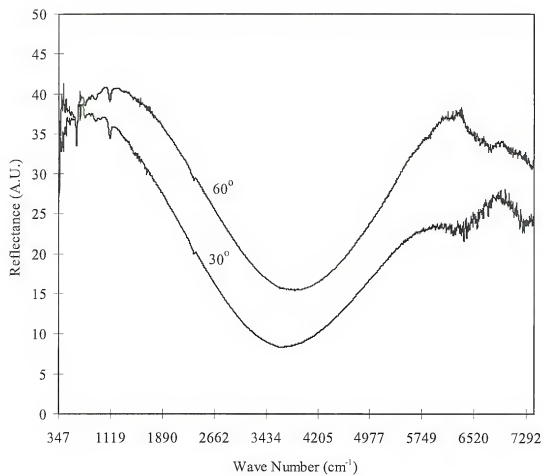


Figure 3-11. FTIR spectra for aluminum doped zinc sulfide films taken at angles of 30° and 60°.

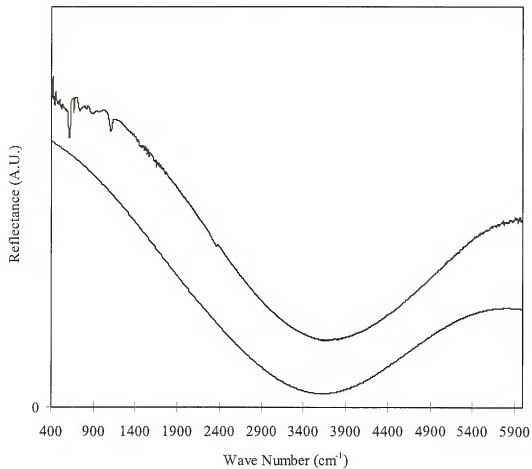


Figure 3-12. Actual and modeled FTIR spectra for aluminum doped zinc sulfide films.

thickness or free carrier concentration are independently measured and used as a fixed parameter. Free carrier concentrations are accurate for net concentrations greater than about $5 \times 10^{17} \text{ cm}^{-3}$.

FTIR spectra of aluminum doped zinc sulfide films were taken at two different reflectance angles. It is necessary to use at least two different angles to ensure that the plasma minimum is located and that an interference fringe is not mistaken for the plasma minimum. As the reflectance angle is changed, the effective thickness of a film will change and any features related to interference patterns will shift to different wave numbers. A plasma minimum in a spectrum will not shift to different wave numbers as the reflectance angle is changed. Figure 3-10 shows the FTIR spectra taken at two different angles for an aluminum doped zinc sulfide film. The spectra are largely similar and the minimum located at approximately 3750 cm^{-1} was taken as the plasma minimum. Using the thickness obtained by SEM, the doping level was used as a fitting parameter to model the FTIR spectrum. The best fit resulted from using a carrier concentrations of $2.4 \times 10^{19} \text{ cm}^{-3}$ using the growth conditions mentioned above.

Since silicon is not available in semi-insulating form, Hall measurements were not possible on these samples. Additional experiments were performed in which aluminum doped zinc sulfide films were deposited on glass substrates using growth conditions identical to those above. Hall measurements confirmed n-type doping and yielded a carrier concentration of $4.3 \times 10^{19} \text{ cm}^{-3}$ and an electron mobility of $122 \text{ cm}^2/\text{V sec}$. The fact that the carrier concentration is higher than that derived from FTIR modeling may be due to aluminum segregation at grain boundaries.

CHAPTER 4 SILICON GROWTH

4.1 Silicon on Zinc Sulfide

4.1.1 Substrate Preparation

4.1.1.1 Silicon Substrates

The silicon substrates used for this portion of the study were cut from commercially available 150 mm diameter boron-doped wafers. Both (100) and (111) 4° off towards nearest (110) orientations were used. Doping levels were 3×10^{18} and $2 \times 10^{17} \text{ cm}^{-3}$ respectively. The substrates were degreased using warm trichloroethane, acetone and methanol for 5 min each, followed by a 30 sec DI water rinse. The initial preparation step consisted of a 60 sec etch in a 6:1 BOE solution, followed by a 30 sec overflowing DI rinse. Two different final preparations were used. The first consisted of a 30 sec dip in a 10:1 DI:HF solution followed drying with filtered nitrogen from a liquid nitrogen boil off. The second preparation consisted of an alternating cycle of a 30 sec dip in 10:0 DI:HF followed by immersion for 30 sec in boiling DI. This cycle was repeated for up to 10 times. After this second preparation step, samples were dried using filtered nitrogen from a liquid nitrogen boil off.

After wet etching, the substrates were placed on a quartz transfer tray and immediately transferred to the load lock on the growth system. After loading, the load lock was evacuated to below 1×10^{-4} Torr and back filled to atmospheric pressure with palladium diffused hydrogen. The load lock was then re-evacuated to 1×10^{-5} Torr and

back filled with palladium diffused hydrogen to the growth pressure (50 Torr) and transferred to the growth chamber. The susceptor was then brought to growth temperature and zinc sulfide deposition was initiated.

4.1.1.2 Glass Substrates

The glass substrates used in this study were of Corning 7059 glass coated with 1000 Å of ITO and then 1000 Å of BaTa_2O_5 . The substrates were degreased using warm trichloroethane, acetone and methanol for 5 min each, followed by a 30 sec DI water rinse. No further chemical preparations were used. After the DI rinse, the substrates were dried using filtered nitrogen from a liquid nitrogen boil off. The substrates were then placed on a quartz transfer tray and placed in the load lock on the growth system. After loading, the load lock was evacuated to below 1×10^{-4} Torr and back filled to atmospheric pressure with palladium diffused hydrogen. The load lock was then re-evacuated to 1×10^{-5} Torr and back filled with palladium diffused hydrogen to the growth pressure (50 Torr) and transferred to the growth chamber.

4.1.2 Silicon on Zinc Sulfide Growth

4.1.2.1 Parameter Space

Silicon deposition was performed on zinc sulfide films on silicon substrates. Substrates were cleaned using the methods described above. The temperature was held constant for zinc sulfide and silicon deposition. After zinc sulfide growth, the DEZn flow to the reactor was terminated and a hydrogen sulfide atmosphere was maintained for three minutes. The hydrogen sulfide flow to the reactor was then shut off and the disilane flow to the reactor was initiated. To terminate silicon growth, the disilane flow was switched

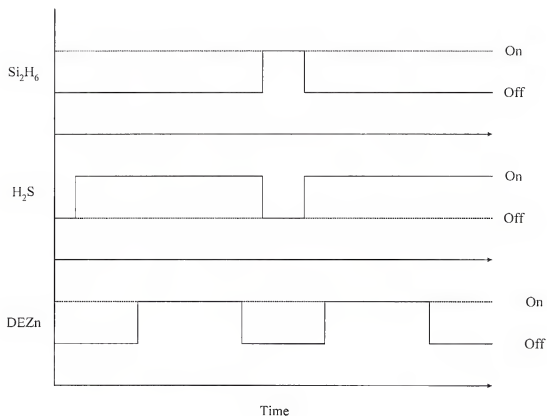


Figure 4-1. Precursor switching sequence for initial silicon growth experiments.

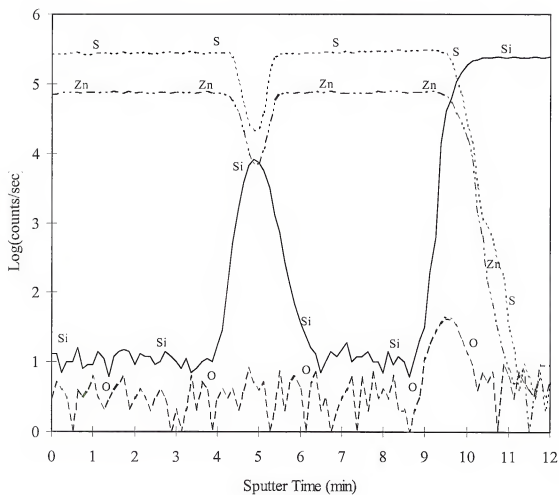


Figure 4-2. SIMS profile of ZnS/Si/ZnS structure. Angle = 60.8° , Beam energy = 3.00 keV, current = 120 nA (Cs^+).

to the vent. Simultaneously, the hydrogen sulfide flow was switched to the reactor. After 60 sec, the DEZn flow was switched to the reactor and deposition of zinc sulfide was resumed. A schematic reactant flow sequence is shown in figure 4-1.

Silicon growth time was maintained at 30 min. The disilane flow rate was maintained at 100 sccm, giving an inlet mole fraction of 2.5×10^{-3} . A 20 min zinc sulfide deposition was performed prior to and subsequent to silicon deposition. Silicon deposition was performed at temperatures from 450 to 600 °C.

4.1.2.2 Growth Analysis

SIMS analysis showed a strong peak in the silicon signal approximately half way through the structure. The location of this peak corresponded exactly with the minimums in the zinc and sulfur signals. No indications of diffusion of silicon, sulfur or zinc were noted. The solubility of sulfur and zinc in silicon reach a maximum at temperatures near 1300 °C and are on the order of 10^{16} cm^{-3} . The solubilities decrease rapidly with decreasing temperature and are below 10^{14} cm^{-3} at the growth temperature.¹⁴³ It was therefore not anticipated that there would be appreciable zinc or sulfur diffusion in the deposited silicon film.

Few studies have been conducted concerning the solubility of silicon in zinc sulfide. In order to study ZnS:Cu,Si phosphors, Wachtel¹⁴⁴ fired zinc sulfide powder with copper compounds and silicon under a hydrogen sulfide atmosphere. Maximum silicon incorporation was achieved using up to 20 mole % silicon and two firings at 1100 °C. This resulted in conversion of the silicon to SiS₂ and in some silicon incorporation. No quantitative data on the solubility of silicon under these conditions was reported, but an

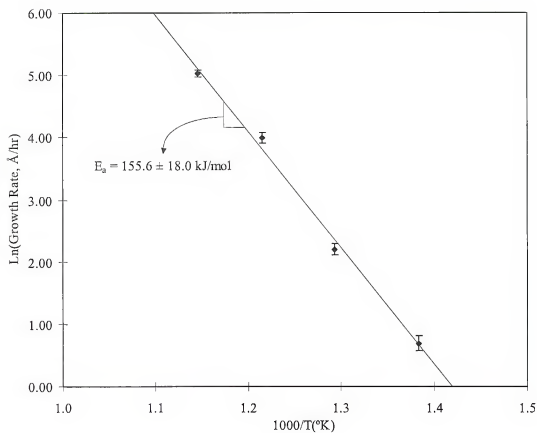


Figure 4-3. Arrhenius plot of disilane growth rate data. Note apparent activation energy of $155.6 \pm 18.0 \text{ kcal/mol}$.

upper limit of $\sim 10^{19} \text{ cm}^{-3}$ was determined. It was determined that silicon substituted on zinc sites and formed complexes with pairs of copper atoms. Electron spin resonance studies have confirmed that silicon occupies zinc lattice positions in zinc sulfide.¹⁴⁵

The possibility of SiS_2 formation during the deposition process was a concern. Accordingly, a sample was grown in which the hydrogen sulfide flow was maintained to the reactor during silicon deposition. XRD and SIMS analysis showed no evidence of SiS_2 formation. This is consistent with the findings of Wachtel that the reaction between silicon and hydrogen sulfide was slow at 950 °C and only occurred at an appreciable rate at 1100 °C.¹⁴⁴

Growth rates were determined by SEM and TEM measurements. As shown in figure 4-4, substrate temperature was found to have a strong influence on growth rate. Silicon layers were noted to conform with the zinc sulfide interface. SEM analysis of films grown at higher temperature showed excellent thickness uniformity.

The strong temperature dependence of the growth rate indicates a reaction limited growth regime. When the data are plotted on an Arrhenius plot, an apparent activation energy of $155.6 \pm 18.0 \text{ kJ/mol}$ is obtained. There are several possible mechanisms that would explain this activation energy. The first and simplest is that surface diffusion of hydrogen on silicon is somehow responsible. The activation energy for this process is known to be $144.8 \pm 19.2 \text{ kJ/mol}$.¹⁴⁶

This mechanism seems to explain the measured activation energy well, but further elucidation is possible. If simple surface diffusion of hydrogen were the rate limiting step, then a similar activation energy would be measured for silicon deposition in a hydrogen atmosphere from silane and chlorosilane precursors. This, however is not the

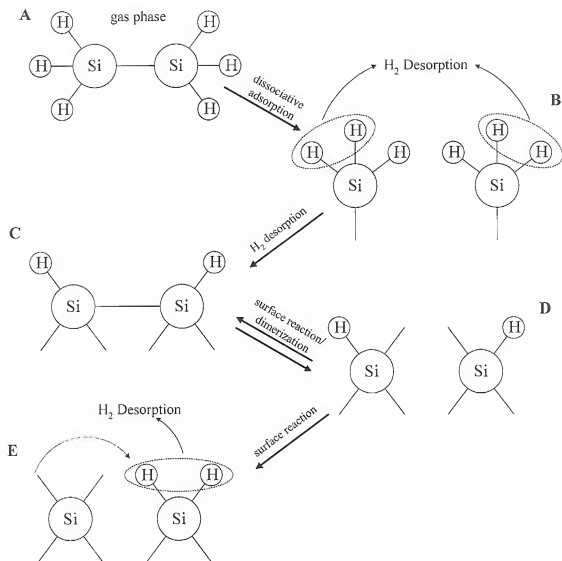


Figure 4-5. Proposed mechanism for silicon growth from disilane. Based on isothermal hydrogen desorption study of Horie et al.

case. The activation energies for silicon growth from SiCl_4 , SiHCl_3 , and SiH_2Cl_2 are 159.0 ± 5.0 kcal/mole, 87.0 ± 9.6 kcal/mole and 43.5 ± 14.6 kJ/mol.⁷ Since the reaction pathway for SiCl_4 involves gas phase reactions with hydrogen that end in the production of SiH_2Cl_2 which subsequently decomposes to yield silicon and HCl , it seems doubtful that simple surface diffusion of hydrogen is responsible for the apparent activation energy for silicon growth from disilane.

Since it has been shown to have a significant probability of dissociative desorption on silicon surfaces at temperatures as low as 500°C ,¹⁴⁷ a mechanism involving SiH_x (where $x \leq 3$) species seems more probable. Dissociative adsorption of disilane results in SiH_3 surface species. SiH_3 on the surface rapidly reacts to form SiH by hydrogen desorption. The behavior of the SiH surface species is vital in determining the rate limiting mechanism for silicon growth from disilane.

Horie et al. studied the desorption rate of hydrogen during isothermal annealing for adsorbed disilane on silicon surfaces.¹⁴⁸ In their study, it was determined that surface disorder was caused by silicon dimer bond breaking and reformation. It was found that hydrogen desorption occurred through dimer bond breaking followed by hydrogen transfer to one member of the dimer pair to form a dihydride prior to hydrogen desorption. Reider, Hofer and Heinz have estimated the activation energy of this at 144.3 ± 19.2 kcal/mole.¹⁴⁹ A diagram of this mechanism is shown in figure 4-5. This mechanism is consistent with the data obtained for silicon growth from disilane and what is known about hydrogen desorption from silicon.

Although SEM analysis showed apparently smooth interfaces between zinc sulfide and silicon films, higher resolution TEM micrographs revealed a rough interface.

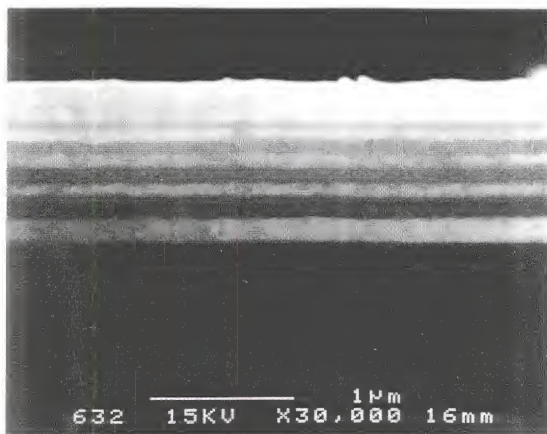


Figure 4-6. SEM micrograph of zinc sulfide/silicon multi-layer structure. Silicon deposition times were 10, 8, 6, 4 and 2 minutes.

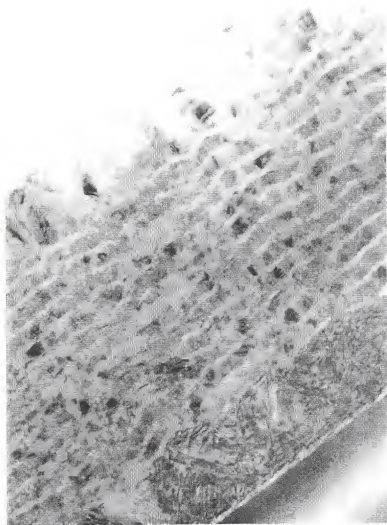


Figure 4-7. TEM micrograph of zinc sulfide/silicon multi-layer structure.

It was noted that although the initial zinc sulfide layer was single crystal, all subsequent layers were polycrystalline. It was hypothesized that the rough surface of the initial zinc sulfide film provided favorable nucleation sites for a variety of silicon phases. To determine what caused this transition to polycrystalline material, a study of the effect of a number of growth parameters on the morphology of zinc sulfide films on silicon was conducted in an attempt to resolve this situation.

4.1.3 Zinc Sulfide Surface Effects

4.1.3.1 AFM Surface Study

Atomic Force Microscopy (AFM) was used to study the surface of zinc sulfide films grown for various times and under different conditions. The growth temperature was varied between 350 and 550 °C. The DEZn inlet mole fraction was varied from 6.0 to 10.0 $\times 10^{-5}$. A constant VI/II ratio of 80 was maintained for all growths. A Digital Instruments Nanoscope III AFM was used to conduct the study. Samples were analyzed in both tapping mode and contact mode. Figure 4-8 shows the surface of a typical zinc sulfide film deposited in the growth system. The root mean square (rms) surface roughness of the films typically varied from about 20 to 35 nm. The rough surface provides a large number of locations on the surface where silicon deposition can begin. This leads to island nucleation and subsequent three dimensional growth. The various planes present on the zinc sulfide surface result in a multitude of slightly different orientations of silicon islands. As a result, by the time the islands coalesce, the silicon layer is polycrystalline. It follows that the zinc sulfide cap layer would also be polycrystalline.

A series of samples were grown using the same growth conditions but for varying lengths of time to determine the effect of film thickness on surface roughness. The growth rate was maintained at 1.6 $\mu\text{m/hr}$. If the roughness increases with time, then deposition of thin films of zinc sulfide should result in improved crystallinity of silicon layers. As shown in figure 4-9, the surface roughness rapidly increases during the first few minutes of growth and then reaches a steady value. This behavior was noted on both (100) and (111) oriented substrates.

Surface roughness was measured and averaged for four locations on each substrate. In order to determine if substrate orientation had any significant effect on roughness, this data was collected for a series of growths using both (100) and (111) oriented substrates. All runs were performed using a growth temperature of 450 $^{\circ}\text{C}$, inlet DEZn mole fraction 8.0×10^{-3} , and $\text{VI/II} = 80$. A total of 15 different samples was analyzed. Although on average the roughness of films grown on (100) substrates was lower, the difference between the orientations was not statistically significant. Taken as a whole, the data showed an average surface roughness of 26.92 nm with a standard deviation of 2.84 nm.

In order to assess the individual sample variation, surface roughness was measured at between six and ten locations on each sample. Measurements were taken on square areas of 1, 5 and 10 μm per side. Statistically, there was no difference in the surface roughness measured on sample areas of this size. The within sample variation was found to be $< 10\%$ of the average rms roughness.

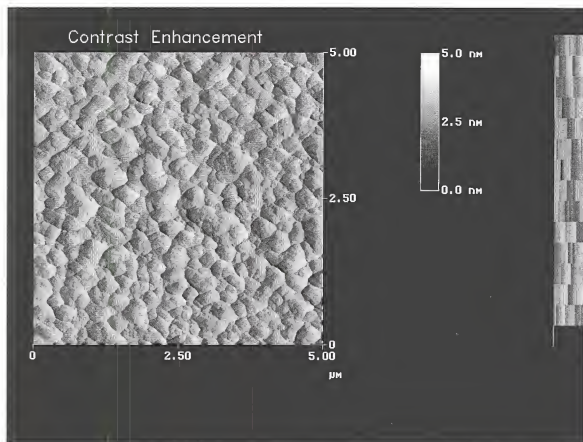


Figure 4-8. Deflection mode AFM scan of a typical zinc sulfide on silicon film. 30 minute deposition, growth temperature = 450 °C, DEZn inlet mole fraction = 8.0×10^{-5} , VI/II = 80.

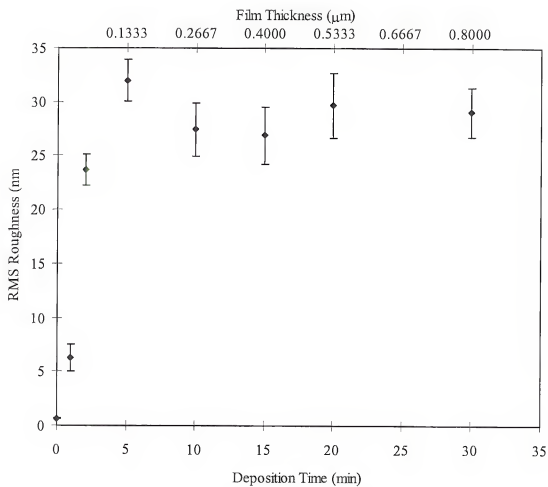


Figure 4-9. Effect of deposition time on zinc sulfide surface roughness on (100) silicon. Roughness at time zero is that of silicon substrate.

4.1.3.2 Factorial Design

There are many factors that can affect the surface morphology of MOCVD grown layers. To examine the dependence of surface morphology with respect to even a few of these variables by conventional experimental methodologies would take a large number of experiments and yet would not provide information on potential interactions between parameters. Traditional experimentation follows the idea of changing one variable at a time while holding all other variables constant. This method is inefficient and may result in a data yield that is incomplete when compared to design of experiment (DOE). DOE is a structured method of testing each variable that maximizes the amount of information extracted from a given number of experiments.^{150,151}

For simplicity, a two-level fractional factorial design was used to investigate the effects of five parameters on surface roughness. For factorial designs, it is typical to repeat the set of runs to allow direct measurement of variation or experimental error. The data previously collected to determine the run to run and within sample variation was used as a measure of the variation and experimental error.

When performing a 2^k factorial design, the number of experiments required increases exponentially with k . For large values of k , there is often a great deal of redundant information. For example, the 32 runs required for a 2^5 factorial design allows the calculation of the average, 5 main effects, 10 two parameter interactions, 10 three parameter interactions, 5 four parameter interactions and 1 five parameter interaction. If, it is assumed that the higher order interactions are negligible, then the number of runs can be reduced at the expense of information on the higher order interactions.

Table 4-1. 2^{5-1} fractional factorial design using I = -1234.

Order	Run	1	2	3	4	5 = -1234
4	1	-	-	-	-	-
1	2	+	-	-	-	+
13	3	-	+	-	-	+
8	4	+	+	-	-	-
10	5	-	-	+	-	+
9	6	+	-	+	-	-
12	7	-	+	+	-	-
3	8	+	+	+	-	+
14	9	-	-	-	+	+
5	10	+	-	-	+	-
2	11	-	+	-	+	-
6	12	+	+	-	+	+
11	13	-	-	+	+	-
15	14	+	-	+	+	+
7	15	-	+	+	+	+
16	16	+	+	+	+	-

In this study, the 2_v^{5-1} fractional factorial design shown in Table 4-1 was used. The table was constructed beginning with a full 2^4 design according to standard methods.¹⁵² The column signs for the first four variables were then multiplied. The opposite sign of the product was then used for the fifth variable. As mentioned before, the reduction in the number of experiments comes at a price. A 2_v^{5-1} design has a resolution of five. The resolution signifies the degree to which effects are confounded. In a resolution five design, the sum of the confounded effects is equal to five. Thus, the main effects are confounded with the four order interactions and the second order interactions are confounded with the third order interactions. If the analysis results show a significant effect in the second or third order interactions, then additional runs will need to be performed to clarify the effects. The sequence of the runs was randomized in order to minimize the effect of any trends on the analysis.

4.1.3.3 Analysis

In any MOCVD process, there are a number of variables that potentially affect the quality of a deposited film. In this study, a total of six variables were investigated: substrate orientation, growth temperature, DEZn inlet mole fraction, H₂S inlet mole fraction, total hydrogen flow (or gas phase velocity) and the ratio of the hydride push flow to the alkyl push

Table 4-2. Parameter space for surface optimization study.

Parameter	Setting		
	-	0	+
Temperature (°C)	450	475	500
DEZn Mole Fraction ($\times 10^4$)	7.0	8.0	9.0
H ₂ S Mole Fraction ($\times 10^4$)	48.0	64.0	72.0
Total Hydrogen Flow (slm)	3.80	4.00	4.20
Push Flow Ratio	4.667	5.667	6.667
Growth Pressure (Torr)	50	50	50
Growth Time (min)	30	30	30

flow. Substrate orientation was investigated by simultaneous preparation and growth on (100) orientated and (111) 4° off towards the nearest (110) orientation silicon substrates. A series of four control growths were performed at the center of the parameter space investigated.

After growth, the surface roughness of samples was measured using AFM. The surface roughness was measured over an area of 25 μm^2 in four locations on each sample and averaged. Again, it was noted that although the (100) oriented material on average had a lower rms surface roughness, the difference was not statistically significant. Following this, the surface roughness for both orientations was averaged and used in the factorial analysis. The magnitude of the effects was determined using Yates algorithm.

The significance of the effects was determined using the standard deviation

derived earlier. The magnitude of each effect was converted to a z-value (magnitude/standard deviation) which was then used to derive a probability for the event.

Table 4-3. Results of factorial analysis.

Effect	Description	Probability
21.399	Average	-
11.474	[DEZn]	0.0003%
4.121	[H ₂ S]	7.35%
3.118	Total H ₂ Flow	13.57%
-2.299	Push Ratio	20.90%
-1.624	[DEZn][H ₂ S]	28.43%
0.740	[DEZn](Total H ₂ Flow)	39.74%
2.201	[DEZn](Push Ratio)	22.07%
1.840	[H ₂ S](Total H ₂ Flow)	25.78%
0.079	[H ₂ S](Push Ratio)	48.80%
3.585	(Total H ₂ Flow)(Push Ratio)	10.38%
2.035	(Temperature)(Push Ratio)	23.58%
-2.253	(Temperature)(Total H ₂ Flow)	21.48%
-1.860	(Temperature)[H ₂ S]	25.78%
-4.404	(Temperature)[DEZn]	6.06%
-6.036	Temperature	1.70%

Significant effects were determined using a criteria of < 5% probability. Only two parameters showed any significant effect: DEZn mole fraction and temperature. The analysis shows that surface roughness decreases with decreasing DEZn mole fraction and increasing temperature.

Since DEZn is the limiting reactant in the deposition of zinc sulfide, it is expected to have the strongest effect on growth rate. It can therefore be inferred that it would have a strong affect on both the surface morphology and the crystallinity. Higher growth temperature increases the mobility of surface species and is thus expected to improve

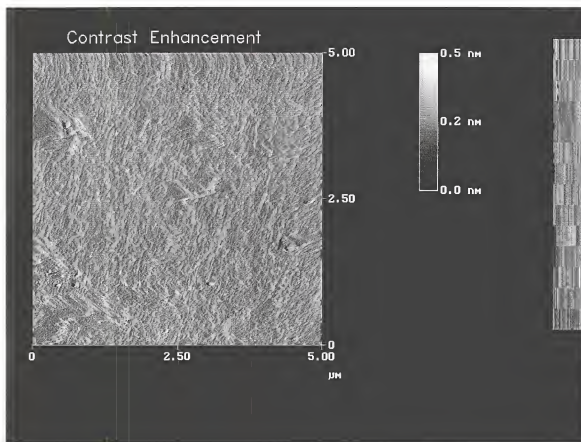


Figure 4-10. Deflection mode AFM scan of zinc sulfide growth using conditions for minimized surface roughness. 30 minute deposition, growth temperature = 600 °C, DEZn inlet mole fraction = 2.0×10^{-5} , VI/II = 80.

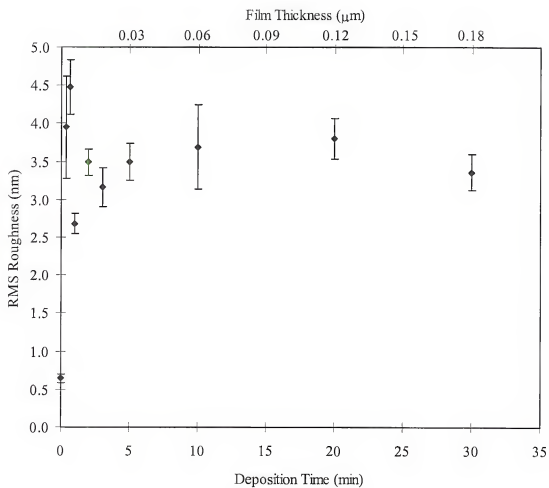


Figure 4-11. Effect of deposition time on zinc sulfide surface roughness on (111) silicon using optimized growth conditions. Roughness at time zero is that of silicon substrate.

surface morphology. Following these results, a new series of growth experiments were performed using a higher growth temperature and a decreased DEZn mole fraction. These experiments led to the optimized surface shown in figure 4-10.

The new conditions showed a remarkable improvement in surface morphology. Previous growths showed a rough surface dominated by rectangular features. The surface of films grown on (111) substrates were dominated by what are believed to be diatomic ledges. These features are crystallographically oriented have a period that agrees well with that expected for a 4° misorientation.. The surface roughness was decreased by almost an order of magnitude to an average of 3.5 ± 0.4 nm.

The growth conditions used resulted in a substantially lower growth rate. To demonstrate that the improvement in surface roughness was not simply due to the thinner films, the effect of deposition time on surface roughness was investigated. It was noted again that the surface roughness rapidly increased and then reached a maximum value. The thickness after a 30 min deposition under these conditions corresponds to the thickness after approximately seven minutes of growth using the using the standard conditions. As was shown in figure 4-9, the surface roughness of films deposited using standard conditions has already achieved its maximum value by this thickness.

4.1.4 Optimized Surface

Silicon growth on the optimized zinc sulfide surface showed substantial improvement. High resolution XRD analysis of silicon/zinc sulfide/silicon films showed no significant difference in crystallinity as measured by intensity and FWHM. AFM scans showed a surface roughness slightly higher than that of the silicon substrate (0.645 nm vs 0.952 nm). The defect density of the silicon epilayers was estimated from etch pit

density measurement (EPD). The EPD was determined by using Sirtl and Schimmel etches¹⁵³ and counting etch pits using a Nomarski microscope. Analysis showed an etch pit density of less than $5 \times 10^2 \text{ cm}^{-2}$. These results indicate that decreasing the surface roughness of the zinc sulfide layer results in a substantial improvement in silicon crystallinity and that silicon heteroepitaxy is possible on zinc sulfide.

Silicon growth on the optimized zinc sulfide surface showed substantial improvement. High resolution XRD analysis of silicon/zinc sulfide/silicon films showed no significant difference in crystallinity as measured by the FWHM. AFM scans showed a surface roughness slightly higher than that of the silicon substrate. Defect density of the silicon epilayers was estimated from etch pit density (EPD). The EPD was determined by using Sirtl and Schimmel etches¹⁵³ and counting etch pits using a Nomarski microscope. Analysis showed an etch pit density of less than $5 \times 10^2 \text{ cm}^{-2}$. These results indicate that decreasing the surface roughness of the zinc sulfide layer results in a substantial improvement in silicon crystallinity and that silicon heteroepitaxy is possible on zinc sulfide.

4.2 Silicon Growth

4.2.1 Low Temperature Silicon Preparation

As dimensions continue to shrink, semiconductor devices become increasingly sensitive to high temperature processing which may destroy or degrade doping profiles. As a result, a great deal of effort has been spent in recent years in searching for ways to generate an oxygen free silicon interface without having to resort to thermal oxide desorption. Research has focused on both ex-situ wet etches and in-situ dry cleaning methods.

4.2.1.1 Ex-situ Techniques

The bulk of the work reported on wet etching preparations for low temperature silicon growth focuses on HF and NH_4F based solutions for a final cleaning step. Traditionally, silicon is prepared using the so-called RCA clean which uses a series of basic and acidic oxidation steps followed by oxide removal with an HF solution.¹⁵⁴ The series of oxidations and etches are designed to generate a surface with a thin passivating layer of oxide that is free of metallic impurities. After the final wet etch step, the substrates are transferred to a growth system where a thermal oxide is grown on the substrates. This thermal oxide is subsequently removed by a high temperature desorption step. Electron stimulated desorption studies have shown that temperatures above 950 °C are required to obtain an oxide free surface.¹⁵⁵ This method results in a highly reproducible oxygen free surface, but adds substantially to the thermal budget and time for a process.

While this method works well for virgin substrates, it is far from ideal for later stages of processing where device structures and doping profiles are already fabricated. A low temperature cleaning step is essential to minimize dopant diffusion. The use of both HF and NH_4F based solutions have been proposed as final steps for substrate preparation for low temperature silicon growth.

Dilute HF solutions have recently been found to provide an effective method for creating a clean, oxygen free, hydrogen passivated silicon surface that does not require a high temperature baking step.¹⁵⁶ Comparison of hydrogen passivated surfaces generated from HF treated surfaces and from quenching the silane CVD reaction are similar¹⁵⁷ and that both surfaces consist of primarily of monohydride species with some dihydride and

hydrocarbon species also present.^{158,159,160} Studies of silicon epitaxy in an ultra high vacuum CVD system have shown that the hydrogen passivated surfaces generated from final HF etches is possible in two temperature ranges; $\sim 425\text{ }^{\circ}\text{C}$ to $650\text{ }^{\circ}\text{C}$ and $> 750\text{ }^{\circ}\text{C}$.¹⁵⁸ In the lower temperature range, the kinetics of hydrogen desorption from the surface are slow with respect to the growth process and a clean interface is maintained. Between temperatures of 650 and $750\text{ }^{\circ}\text{C}$, the hydrogen desorption occurs faster than epitaxial growth, resulting in prolonged exposure of a highly reactive silicon surface. Above $750\text{ }^{\circ}\text{C}$, the growth rate continues to increase and epitaxial growth is once again possible.

NH_4F -based etches also result in high quality, hydrogen passivated silicon surfaces. It has been shown that NH_4F etches may be superior to HF etches in providing a stable hydrogen passivated surface.^{161,162} HF-based etches yield smooth surfaces for (100) silicon substrates and rough surfaces for (111) silicon substrates.¹⁶³ In contrast, NH_4F based etches have been shown to have the opposite behavior and generate atomically smooth surfaces with large (111) terraces.¹⁶⁴ For (100) oriented material, the surface will roughen as (111) facets develop. The degree of surface roughening on a substrate depends on the amount of etching that occurs.

As a result of the behaviors of HF and NH_4F etches, it is expected that a final HF etch will provide the best results for (100) substrates and a final NH_4F etch will provide the best results for (111) substrates. Despite the characteristic of these etchants, it should be pointed out that there are numerous references in the literature of successful low temperature silicon epitaxy using both types of etches on both (100) and (111) oriented substrates.¹⁶⁵

4.2.1.2 In-situ Techniques

Additional work has been performed on in-situ techniques for silicon surface preparation. These techniques fall into one of two broad categories: plasma cleaning and HF vapor. As mentioned previously, it is possible to generate a plasma in the system, but it is not possible to control the chemistry, uniformity, and power levels of the plasma. Additionally, the system is not designed for HF sources. Due to the equipment constraints, these techniques were not investigated. They are merely mentioned here for completeness.

4.2.1.3 Substrate Preparation

Based on the experience reported in the literature, the DI:HF/boiling DI procedure used in preparing silicon substrates for zinc sulfide growth (see § 4.1.1.1) was used to prepare silicon substrates without modification. The low interfacial oxygen levels detected by SIMS indicated that either method used in zinc sulfide growth should provide a sufficiently clean surface for low temperature silicon homoepitaxy.

4.2.2 Silicon on Silicon Growth

4.2.2.1 Growth Conditions

The growth conditions used for silicon homoepitaxy are listed in table 4-4. The silicon deposition temperature was maintained at or above 550 °C to establish a reasonable growth rate. The deposition time was varied from one to sixty min. After preparation and substrates of both orientations were loaded, the substrates were then brought to growth temperature and silicon growth was initiated with no further treatment of the surface. Silicon on silicon samples were analyzed by XRD, AFM, optical microscopy and selective etching to determine defect density.

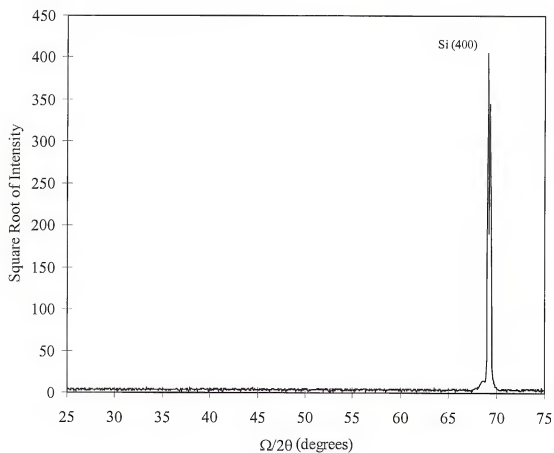


Figure 4-12. Low resolution XRD scan of 1 μm thick silicon film on silicon (100) substrate.

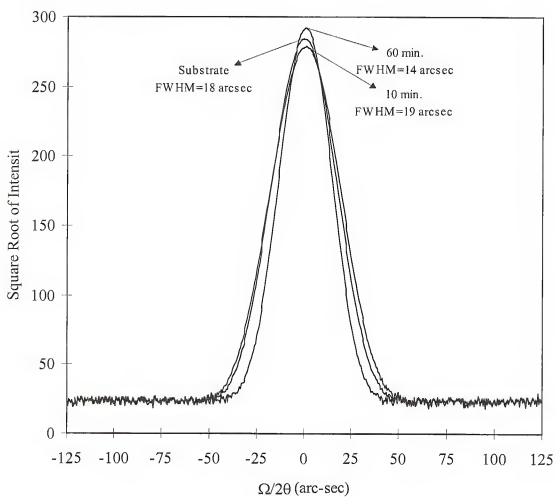


Figure 4-13. High resolution XRD scans of low temperature silicon films.

Table 4-4. Parameter space for silicon on silicon deposition.

Variable	Range
Si ₂ H ₆ Mole Fraction ($\times 10^4$)	25.0
Growth Temperature ($^{\circ}\text{C}$)	550 to 600
Total Hydrogen Flow Rate (slm)	4.0
Deposition Time (min)	1 to 60
Growth Pressure (Torr)	50

4.2.2.2 Analysis

Low resolution XRD scans showed no evidence of polycrystalline material on any runs. No differences were detected between bare substrates and the substrates with low temperature silicon. High resolution XRD showed shoulders on the substrate peak on films with thin samples. These shoulders increased in intensity and narrowed in width as film thickness increased. The presence of these shoulders indicates that in the initial stages of silicon deposition under these conditions, some defects were present, but that the quality of the material improved with increasing film thickness. Though the difference was not statistically significant, samples with 1 μm thick silicon films actually showed a narrower FWHM than the substrate!

Substrates of both orientation were prepared using the methods described in § 4.2.1.3. These samples were loaded into the growth system and brought to growth temperature for 10 minutes and then cooled to simulate any roughening of the surface due to thermal effects. AFM analysis showed a slight increase in surface roughness (0.645 nm vs 0.835 nm).

Sedgwick, Agnello and Grützner investigated the effect of oxygen contamination on low temperature silicon growth.¹⁶⁶ Clean substrates were exposed to oxygen doses equivalent to surface coverages of 0.001 to 1 monolayer. They

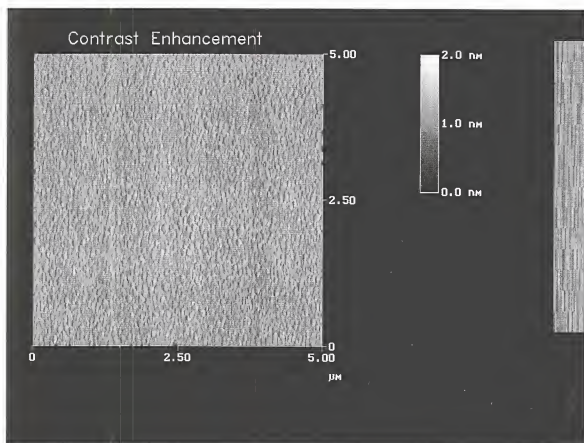


Figure 4-14. Deflection mode AFM scan of 1 μm thick silicon film on silicon (100) substrate.

observed pyramidal and star defects in epilayers which were believed to be due to the formation of (111) microtwins near the interface.¹⁶⁷ The pyramidal defect density was found to be proportional to the square of the interfacial oxygen density. This relationship was found to hold for interfacial oxygen densities from $5 \times 10^{11} \text{ cm}^{-2}$ to $1 \times 10^{15} \text{ cm}^{-2}$ over a wide range of experimental conditions.

Based on this work, samples were analyzed using Nomarski microscopy. The maximum pyramidal defect density was found to be less than 10 cm^{-2} , indicating an interfacial oxygen density of less than $1 \times 10^{11} \text{ cm}^{-2}$. To verify the technique, a sample was prepared as normal and then immersed in room temperature DI water for three min to expose the surface to oxygen. Analysis revealed the presence of a high concentration of pyramidal defects ($\sim 7 \times 10^3 \text{ cm}^{-2}$) corresponding to an interfacial oxygen concentration of $\sim 5 \times 10^{12} \text{ cm}^{-2}$. This confirmed that the preparation methods used are able to generate high quality oxygen free silicon surfaces.

Selective etching to reveal defects showed defect densities of $1 \text{ }\mu\text{m}$ thick films to be below 100 cm^{-2} . These results indicate that it is possible to grow high quality silicon films using disilane as a silicon precursor and without high temperature processing.

CHAPTER 5

DEVICE FABRICATION AND TESTING

5.1 Zinc Sulfide/Silicon/Zinc Sulfide Structures

5.1.1 Growth Conditions

Device structures were grown on silicon (100) and (111) 4° towards the nearest (110) off orientation substrates prepared using the methods previously described in Chapter 3. Glass substrates were prepared by degreasing in warm solvents as described in

Table 5-1. Silicon quantum well and zinc sulfide barrier growth conditions.

Variable	Set Point
DEZn Mole Fraction ($\times 10^4$)	0.20
H ₂ S Mole Fraction ($\times 10^4$)	16.0
Si ₂ H ₆ Mole Fraction ($\times 10^4$)	25.0
Alkyl Push Flow (slm)	0.60
Hydride Push Flow (slm)	3.40
Growth Pressure (Torr)	50
Susceptor Temperature (°C)	600

Chapter 4. All growths of quantum well portion of the structures were performed at a susceptor temperature of 600 °C. After deposition of the quantum wells, the H₂S flow was increased and the susceptor temperature was reduced to 350 °C prior to zinc sulfide cap deposition. Growth conditions used for the barrier layers were set at the conditions found in Chapter 4 to give the highest quality zinc sulfide surfaces. Barrier thicknesses were held constant at 50 Å. The nominal quantum well thickness was determined by extrapolation of thickness/deposition time data. The quantum well thickness was varied

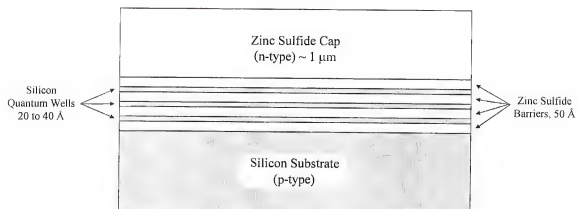


Figure 5-1. Silicon/zinc sulfide MQW LED structure.

Table 5-2. Zinc sulfide cap layer growth conditions.

Variable	Set Point
DEZn Mole Fraction ($\times 10^4$)	0.80
TEAl Mole Fraction ($\times 10^4$)	0.024
H ₂ S Mole Fraction ($\times 10^4$)	64.0
Alkyl Push Flow (slm)	0.60
Hydride Push Flow (slm)	3.40
Growth Pressure (Torr)	50
Susceptor Temperature (°C)	350

from 20 to 40 Å. The number of quantum wells in a samples was varied from 2 to 30. The growth parameters for quantum well and cap layer growth are listed in tables 5-1 and 5-2 respectively.

5.1.2 Characterization Results

Samples containing multiple quantum wells were analyzed by micro Raman spectroscopy. Bulk crystalline silicon shows a strong Raman signal at 520 cm⁻¹. Quantum confinement effects should result in a shift of the signal to lower wavenumbers. Sasaki and Kitahara used Raman to characterize the size of silicon nanoparticles in porous silicon and where able to correlate Raman and PL shifts.¹⁶⁸ Figure 5-2 shows a clear shift in energy for nominal 30 Å quantum well structures compared to bulk siliconw. Broadening of the signal indicates that the well widths may not be completely uniform or that the silicon layers are not completely planar.

Multi-quantum well (MQW) samples with 30 periods and nominal well thicknesses of 20 and 30 Å were grown on glass substrates and analyzed by UV-Vis absorption to determine absorption shifts. Figure 5-3 shows the absorption spectra of two MQW samples and the spectra from a control sample of 1 µm of aluminum doped zinc sulfide on glass. The addition of silicon quantum wells has a strong influence on the absorption spectrum. The absorption wavelength of the quantum wells is proportional to

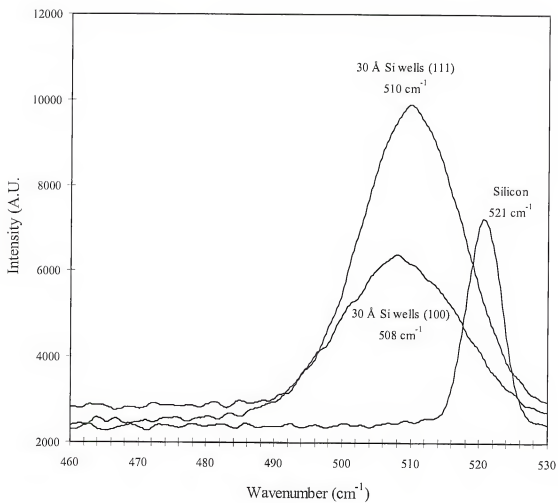


Figure 5-2. Raman spectra for bulk silicon and silicon MQW samples.

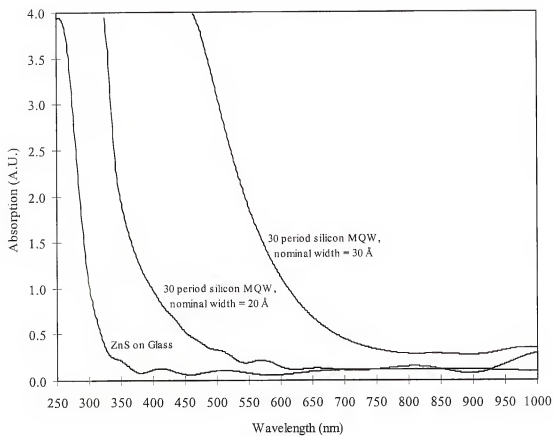


Figure 5-3. Absorption spectra for zinc sulfide and zinc sulfide with silicon MQWs on glass substrates.

the well width. While the qualitative correlation with the predicted absorption wavelengths from quantum mechanical calculations is quite good, the quantitative agreement is poor. This is believed to be due to the fact that zinc sulfide deposition on glass substrates yield polycrystalline material. This in turn leads to a rough interface. As a result, the deposited silicon layers are not true quantum wells and may consist of a network of silicon dispersed in a zinc sulfide matrix or of nanocrystalline material. In both cases, the increase in the number of confinement dimensions will increase the confinement energy. It is therefore expected that the absorption edge will shift to shorter wavelengths as was observed.

MQW samples grown on silicon substrates were analyzed for PL using a 325 nm HeCd laser as an excitation source. A zinc sulfide sample with a high temperature, undoped buffer layer and a lower temperature aluminum doped cap was used as a control to determine PL emissions from the silicon quantum wells. Figure 5-4 shows the PL spectra from the control sample and MQW samples with varying nominal well thicknesses. All samples showed strong self activated emissions at ~ 425 nm and ~ 460 nm from donor complexes.^{169,170,171} Samples containing MQW layers showed additional long wavelength peaks not seen in the control sample. This PL emission shifted to shorter wavelengths as the nominal well width decreased. The full width, half maximum (FWHM) of the emission peaks ranged from 43 to 67 nm.

A comparison of the predicted emission wavelength and the measured PL wavelength shows that in each case, the prediction overestimated the emission wavelength. There are several possible explanations for this. The well thickness for the samples was determined by adjusting the growth time for the silicon layers. It was not

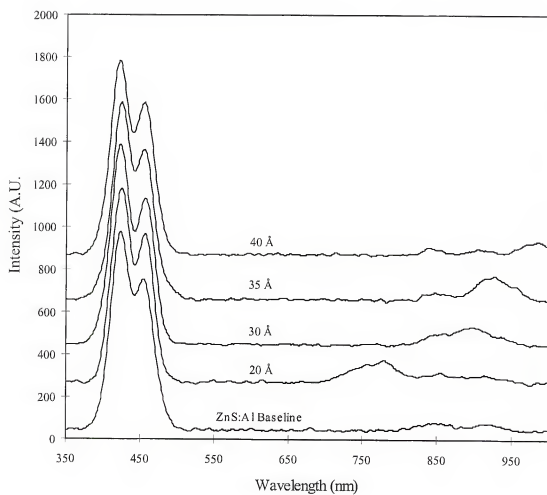


Figure 5-4. PL spectra of an aluminum doped zinc sulfide control sample and MQW samples grown on silicon substrates.

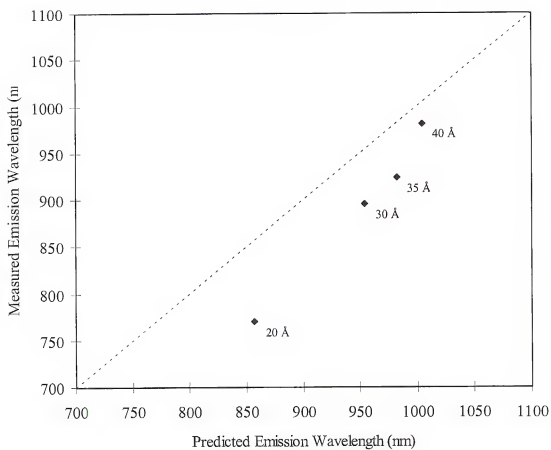


Figure 5-5. Predicted versus measured PL emission wavelength for MQW samples grown on silicon substrates.

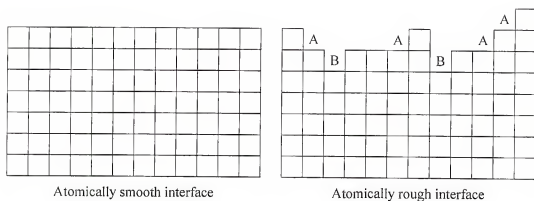


Figure 5-6. Comparison of atomically smooth and rough interfaces during crystal growth. Atoms encountering sites marked A and B have a higher probability of incorporating compared to atoms encountering a smooth surface.

possible to obtain accurate measurements for layer thickness below ~ 100 Å. Data on layer thickness versus time was fitted using a linear equation. This equation was then used to extrapolate the growth time required for thin layers. The extrapolated line did not intersect the origin. This indicated the presence of an energy barrier that must be overcome before silicon deposition begins. The presence of this offset time make accurate prediction of film thickness for short growth times difficult.

An alternative explanation relates to the conditions under which the thickness data used was collected. The data was collected from samples grown using conditions that yielded a rough zinc sulfide growth surface. During growth on an atomically smooth surface, there are few terrace ledges or step sites where an adatom can bond with two or more atoms. On an atomically rough surface adatoms, on average, have a greater probability of encountering a terrace ledge and being incorporated in the growing film. Thus, it is expected that rough surfaces will have a higher growth rate than smooth surfaces.

The MQW samples were grown using the conditions for minimized surface roughness. Thus, it is expected that the growth rate of the silicon quantum wells will be lower, and that the samples will therefore have a shorter emission wavelength than predicted.

Alternatively, if the interfaces of the quantum wells were not atomically smooth, the silicon would be confined in more than one dimension. Increasing the number of confinement dimensions should increase the confinement energy and yield a shorter emission wavelength.

5.2 Device Fabrication and Testing

5.2.1 Device Fabrication

Devices were fabricated by scribing the back side of the silicon substrate and cleaving into samples approximately 5 mm square. Front side contacts were made by painting a 50:50 indium:gallium alloy on the zinc sulfide cap and annealing for five minutes at 300 °C under a forming gas atmosphere.

Since the alloy used is a liquid metal at room temperature, additional indium was added to the contact and heated with a clean soldering iron until a solid contact was produced. Back side contacts were made by placing a piece of freshly cut indium on the back side of the silicon wafer and heating with a clean soldering iron.

5.2.2 Testing Results

Testing of LED devices was performed by contacting the upper and lower contacts with metal probes and applying a voltage. Samples were observed in a dark room for signs of electroluminescence. No luminescence was observed for any samples for applied voltages of less than 6 V. Two samples grown on (100) substrates with nominal well widths of 20 Å showed weak red emission visible to the naked eye that increased in intensity for voltages above 6 V. This emission was visible only under scotopic viewing conditions.

Device structures fabricated from the control sample and MQW samples with wider well widths showed no evidence of luminescence even at voltages as high as 9 volts. No luminescence was observed on any samples grown on (111) substrates.

CHAPTER 6 CONCLUSIONS

6.1 Review of Results

6.1.1 Epitaxial Growth

6.1.1.1 Zinc Sulfide on Silicon

It has been shown that epitaxial zinc sulfide on silicon can be readily deposited on both (111) 4° off towards nearest (110) and (100) oriented silicon substrates. The conflicting reports in the literature about which orientations of silicon result in epitaxial growth are believed to be due to residual oxygen at the silicon/zinc sulfide surface. The majority of reports in the literature stated that epitaxial growth was possible on (100) substrates, but that (111) substrates yielded polycrystalline material. A small percentage of the reports stated that the converse was true.

Zinc sulfide deposition was found to be mass transfer limited over a temperature range of 300 to 650 $^\circ\text{C}$. The growth rate decreased dramatically at 700 $^\circ\text{C}$. At this temperature, the zinc partial pressure in the growth chamber was equal to the congruent sublimation pressure of zinc sulfide. Although no runs were performed with increased DEZn mole fractions, it is believed that higher sulfur and zinc partial pressures would extend the mass transfer limited regime to higher temperatures.

A fractional factorial design was used to instigate the effects of growth parameters on the surface roughness of zinc sulfide on silicon films. Growth temperature and DEZn mole fraction were found to have the greatest effects on surface roughness. Surfaces with

rms roughness values of 3.5 nm or less were obtained under optimum conditions. AFM scans revealed the presence of what appear to be crystallographically oriented, diatomic ledges on the growth surface. Surface roughness was found to rapidly increase in the first few minutes of growth and then saturate at a steady value.

6.1.1.2 Silicon on Zinc Sulfide

Epitaxial growth of silicon on zinc sulfide was shown to be possible provided the underlying zinc sulfide has a sufficiently low surface roughness. High surface roughness resulted in deposition of polycrystalline material. It was found that silicon films could be deposited on with EPDs below $5 \times 10^2 \text{ cm}^{-2}$.

Deposition rates were found to be strongly influenced by temperature, indicating a reaction limited growth mechanism. Growth rates were found to vary from 120 Å/hr at 450 °C and 9000 Å/hr at 600 °C using a disilane mole fraction of 2.5×10^{-3} and a total hydrogen flow rate of 4.0 slm. An Arrhenius plot of the growth rate data shows an activation energy of $155.6 \pm 18.0 \text{ kJ/mol}$. The activation energy was found to be in close agreement with that of silicon surface dimer formation.

6.1.1.3 Silicon on Silicon

Successful low temperature silicon epitaxy was shown to be possible using a variety of HF and NH_4F preparations. It was found that no high temperature oxide desorption step was required for epitaxial growth. Pyramidal defect density indicated an interfacial oxygen concentration on the order of $1 \times 10^{11} \text{ cm}^{-2}$ or less on prepared silicon substrates. EPD of material deposited at 550 and 600 °C was less than 100 cm^{-2} .

6.1.2 Evidence for Quantum Confinement Effects

A review of techniques for calculating band alignments in semiconductor heterojunctions showed that the silicon/zinc sulfide system forms a type I band alignment; resulting in strong confinement of both electrons and holes in silicon. Quantum mechanical calculations show that the predicted emission edge for silicon confined by zinc sulfide is essentially independent of the conduction band offset except for the extremes of no electron or no hole confinement.

Analysis of sulfide/silicon/zinc sulfide structures by Raman spectroscopy, UV-Vis absorption and PL indicated quantum confinements in silicon MQW samples with zinc sulfide barriers. The characterization results showed trends consistent with quantum confinement of silicon by zinc sulfide. MQW LED structures with 20 Å nominal well widths grown on p-type silicon with n-type zinc sulfide cap layers showed visible electroluminescence at applied voltages greater than 6 V.

6.2 Directions for Future Research

6.2.1 Device Optimization

6.2.1.1 Growth Uniformity

Although this study demonstrated the feasibility of a silicon based LED device, much work remains in optimizing the device structure. The device yield suffered greatly from non-uniform growth of zinc sulfide barrier layers. The zinc sulfide barrier thickness has a strong effect on the threshold voltage and brightness of the device.

The MOCVD system in this study was designed primarily as a materials research system. The focus during the design phase was on the ability to grow zinc sulfide with the selected precursors and not for uniform growth. These difficulties with growth

uniformity stem from the design of the reactor inlet. The highly reactive nature of the zinc and sulfur precursors used necessitates the use of separate inlet for each source. The use of a central inlet for DEZn results in a zinc sulfide growth profile that is approximately gaussian with a maximum located on the centerline of the reactor. Growth in a mass transfer limited regime therefore yields films with an approximately gaussian thickness profile.

Two options are open for improving growth uniformity. The first is to use a less reactive sulfur precursor. DEZn and H_2S are known to be highly reactive, even at room temperature. It has been reported that use of both diethyl sulfide (DES)¹⁷² and carbon disulfide¹⁷³ as a sulfur source for zinc sulfide deposition effectively eliminates pre-reactions. This would allow the precursors to be mixed prior to injection into the growth chamber, resulting in more uniform film growth.

A second alternative is a redesign of the growth chamber and reactor inlet to accommodate multiple injectors. The use of multiple injectors helps to minimize concentration profiles and therefore tends to result in more uniform growth. While more costly, this alternative would also allow for a change in reactor geometry and has the potential for yielding large area uniform growth on multiple large diameter substrates.

6.2.1.2 Doping Level Optimization

The doping levels of both the silicon substrate and the zinc sulfide cap were not optimized. Doping levels in LEDs are known to have a significant impact on both the threshold voltage and the brightness of an LED. Equipment availability and substrate material limitations affected the ability to adjust the doping levels of both the silicon substrate and the zinc sulfide cap layer. Typical commercial LED structure use doping

levels between $5 \times 10^{17} \text{ cm}^{-3}$ and $5 \times 10^{18} \text{ cm}^{-3}$. While the doping levels of the zinc sulfide cap are on the upper side of this range, the silicon substrates had doping levels between $2 \times 10^{17} \text{ cm}^{-3}$ (111) and $3 \times 10^{18} \text{ cm}^{-3}$ (100). This mismatch in doping levels shifted the depletion zone into the substrate and increased the threshold voltage of the LED. Higher doping levels in the substrate should improve the operating characteristics of the device.

Three methods exist for increasing the silicon doping levels: increased doping of the substrates during bulk crystal growth, ion implantation followed by thermal annealing and deposition of a highly doped silicon buffer layer prior to zinc sulfide deposition. The first option is not feasible for wafer scale optoelectronic integration. The design constraints of the silicon computational devices dictate the doping level of the substrates. This option does remain a possibility for simple LED device construction, although the high brightness of current commercial III-V based LEDs makes such a venture improbable. Such devices may be able to compete in the low brightness LED market due to the potential for significant cost reductions in substrate material, precursors and the lower toxicity of the precursor chemicals. Commercial prices for GaAs substrates are on the order $\$16 \text{ in}^{-2}$ and account for approximately 30% of the final device cost. The cost of silicon substrates is lower by more than an order of magnitude with commercial prices of $\sim \$1.40 \text{ in}^{-2}$ for 150 mm diameter substrates. Additional savings should also be possible due to reductions in the cost of epitaxial growth.

Of these options, the second appears to be the most attractive in terms of commercialization. Ion implantation is already used extensively in silicon device fabrication and would require minimal modification to an existing fabrication facility.

Annealing temperatures and times would need to be constrained so that doping profiles of existing device structures would not be altered.

While technically interesting, the use of a highly doped silicon buffer layer presents new problems. This may be an option for low cost, low brightness LEDs, but typical silicon deposition temperatures make it unfeasible for optoelectronic integration. Development of a method for doping epitaxial silicon films, using disilane as a silicon source, at low temperatures would remove this hurdle. This approach has further potential benefits in increasing brightness as indicated in § 6.2.1.4.

Better control over the doping levels of the zinc sulfide cap layer could be obtained by growth on semi-insulating substrates. Hall characterization requires that the layer being measured be electrically isolated from the substrate. Silicon is not available in semi-insulating form. A full study of aluminum doping in zinc sulfide films would require the use of GaAs, GaP or silicon on insulator (SOI) substrates.

6.2.1.3 Zinc Sulfide Contacts

The optical output of the device suffered greatly due to the opaque metallic contact used on the zinc sulfide cap layer. Although some light was transmitted through the zinc sulfide cap, the brightness of the device could be significantly improved by use of a transparent contact or a transparent current spreading layer. Commercial III-V LEDs use both of these techniques to increase brightness.

This presents a new set of problems due to the low electron affinity of zinc sulfide. Indium-tin oxide (ITO) is one of the most commonly used transparent conductors. A number of successful reports of ohmic contact to zinc sulfide using indium

based alloys implies that indium rich ITO based contact schemes may provide a possible solution.

6.2.1.4 Distributed Bragg Reflectors

Most commercial high brightness LEDs in the 600 - 800 nm range utilize distributed Bragg reflector (DBR) structures to increase brightness. DBR structures take advantage of the difference in refractive index between two materials to produce a high efficiency reflector that can be tuned to a specific wavelength.¹⁷⁴ The use of a silicon/zinc sulfide DBR structure below the light emitting region could increase the light output of the device by as much as 40 to 60%. Use of such a structure would require the ability to grown highly doped silicon at low temperatures.

Unfortunately, the electrical conductivity of the DBR would most likely be very low due to the highly resistive nature of zinc sulfide. Unless a method is found to deposit low resistivity p-type zinc sulfide, this approach would require p-type silicon in the final layer of the DBR. Contact would then be made to this layer to allow for carrier injection at the base of the structure.

6.2.2 Silicon Quantum Dot LED

The analysis of confinement effects performed in Chapter 2 show that it is highly unlikely that the technology developed in the course of this study will be of use in production of short wavelength (< 600 nm) LEDs. Increasing the number of dimensions of confinement provides an attractive method for decreasing the emission wavelength. Growth of silicon structures confined in two dimensions (quantum wires) or three dimensions (quantum dots) has the potential to shift emission wavelengths into the blue region of the spectrum

Several approaches are available for growth of quantum dots in this material system. The first is to decrease the deposition time for the silicon layers. A linear fit of film thickness as a function of time for silicon on zinc sulfide shows an offset and does not pass through the origin. This indicates that the presence of an energy barrier which must be overcome before epitaxial deposition begins. An alternative explanation would be that the first silicon islands that form during deposition must reach a critical size in order to be stable and grow over time.

When the first atoms reach the zinc sulfide surface, they randomly diffuse across the surface until they either desorb from the surface and re-enter the gas phase or they react with another atom on the surface to form a cluster. These clusters will grow or decay as additional atoms on the surface collide with it or the component atoms break away from the cluster. The minimum size of a stable cluster depends on the reaction conditions and the interface energy of the material system.

Quantum dots can be deposited by halting silicon deposition before the nuclei grow to the point where they begin to coalesce. Subsequent zinc sulfide growth will cover these dots and the process can be repeated to build up a layer of zinc sulfide with embedded quantum dots.

Another method would be to attempt to simultaneously deposit silicon and zinc sulfide. During the course of this study, such growths were performed in order to evaluate the solubility of silicon in zinc sulfide. No evidence was found suggesting significant solubility of silicon in zinc sulfide. PL characterization of these samples showed extremely intense self-activated emissions related to zinc vacancies. Since it is known that silicon-zinc bonds are not favorable, it is theorized that this emission may be

due to zinc vacancies formed in a zinc sulfide/silicon matrix. At the silicon-zinc sulfide interface, sulfur will preferentially bond with the silicon leading to an increase in zinc vacancies. By adjusting the growth conditions, it should be possible to control the size of the silicon inclusions in the zinc sulfide matrix.

A third alternative is high dosage implants of silicon in zinc sulfide using ion implantation. Subsequent annealing should result in the coalescence of the silicon into nano-crystals embedded in a zinc sulfide matrix. The size of the nano-crystals could be controlled by varying the dosage, implant profile, and annealing conditions.

6.2.3 Silicon/Zinc Sulfide LED

The results of Aven and Cusano¹⁷⁵ on copper sulfide/zinc sulfide junctions indicates that a short wavelength LED may be possible using a silicon/zinc sulfide heterojunction. Copper sulfide is believed to be an indirect band gap semiconductor with a band gap comparable to that of silicon. Emission was reported at wavelengths as low as 445 nm. Free hole concentrations in the copper sulfide were determined to be in the range of $1 \times 10^{20} \text{ cm}^{-3}$ to $1 \times 10^{22} \text{ cm}^{-3}$. Zinc sulfide films were reported to be "strongly n-type."

Maximum p-type doping in silicon has been reported to be on the order of $1 \times 10^{20} \text{ cm}^{-3}$ to $3 \times 10^{20} \text{ cm}^{-3}$.¹⁷⁶ Thus, it should be possible to create a comparable device using silicon in place of copper sulfide. The various schemes for increasing device brightness detailed in § 6.2.1 could potentially result in a short wavelength device that would be competitive with commercial III-nitride LEDs.

6.2.4 Long Wavelength Quantum Cascade LED

An inspection of the electron energy levels as a function of silicon quantum well width indicates that a quantum cascade LED may be possible. Quantum cascade LEDs

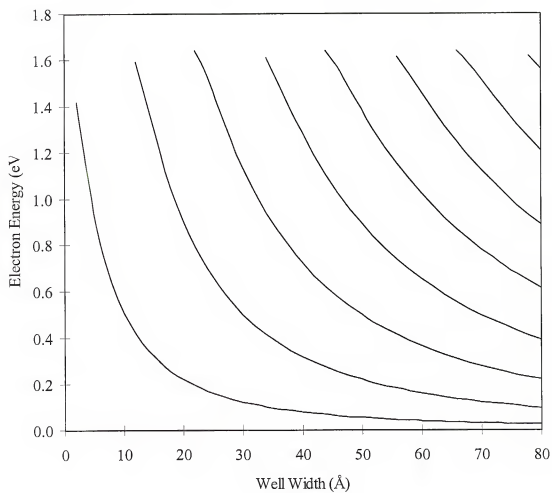


Figure 6-1. Electron energy levels for a silicon quantum well with zinc sulfide barriers.

take advantage of resonant tunneling phenomenon in multi-quantum well structures. Since this type of device relies only on the transport of a single species of charge carrier, concerns with p-type doping and hole transport in zinc sulfide are avoided. Potential emission wavelengths range from the near (just over 1 μm) to far infrared ($> 8 \mu\text{m}$). This range includes the 1.3 μm and 1.55 μm wavelengths used in long distance optical data transmission.

Since these wavelengths correspond to energies below the band gap of silicon, the silicon substrate could be used as a transmission window and serve as a transparent contact. Doping levels cease to be a major concern for this device. The most critical element during growth for this type of device is growth uniformity. Variations in well and barrier thicknesses potentially impact the emission wavelength, operational voltage, and device brightness.

6.2.5 Silicon On Insulator Technology

The fact that zinc sulfide deposited at higher temperatures is highly resistive and that high quality silicon films can be deposited on silicon/zinc sulfide substrates leads to the possibility of a new method for creating silicon on insulator substrates. Initially, SOI substrates were investigated for the potential to increase the radiation resistance of devices. More recently, SOI materials have been used to provide a compact way to increase device isolation and reduce parasitic capacitance.¹⁷⁷ Current research focuses on the use of ion-implanted material or silicon on sapphire (SOS) substrates.

The ion-implantation method utilizes high dose implants ($> 1 \times 10^{18} \text{ cm}^{-2}$) of oxygen or nitrogen in a silicon substrate. Since the goal is to minimize surface damage, the substrates are typically maintained at 500 °C during implantation to allow self annealing

of implant damage. Still, substantial surface damage remains after the implantation process and typically an additional high temperature annealing step is used to remove this damage. Some complications of this process include the sputtering of surface atoms during implantation and the expansion of the substrate surface during oxide or nitride formation which results in residual stress in the substrate.

Silicon on sapphire methods deposit an amorphous silicon film on a sapphire substrate. This amorphous film is then annealed to crystallize the deposited silicon. Although this method provides superior electrical isolation, economically it suffers from the high cost of sapphire substrates ($\sim \$30 \text{ in}^{-2}$). Device fabrication from SOS substrates is further hindered by the hardness of the sapphire and the lack of a cleavage plane for device separation.

A literature search shows an abundance of evidence for the ease of epitaxial growth of zinc sulfide on silicon. The foundations developed in this study for epitaxial growth of silicon on zinc sulfide indicate an inexpensive path to creating a new class of SOI materials. The etch pit density of the silicon on zinc sulfide (SOZ) material in this study indicates that the substrates have the potential to be used in SOI applications. Use of SOZ materials may be limited to applications that utilize lower silicon growth temperatures. The cubic to hexagonal transition for zinc sulfide is 1020°C . The effect of this phase transition on the overlying silicon layer is unknown. High temperature processing of a SOZ substrate may render the zinc sulfide layer conductive due to silicon diffusion. Fortunately, the tendency of zinc sulfide to self-compensate at higher temperatures may counteract any doping effects due to silicon diffusion.

6.2.6 Low Temperature Silicon Cleaning

The results of Chapter 4 indicate a strong potential for a new method for low temperature silicon surface preparation. Preliminary results show that etch pit densities of $< 100 \text{ cm}^{-2}$ are obtainable using a combination of an HF wet etch and in-situ H_2S treatment. No attempts were made at optimizing the process in this study. Higher purity H_2S or longer dosing times may improve the quality of homoepitaxial silicon. The effective temperature range still needs to be investigated although the results of Yongnian, Hickey and Gibson¹⁷⁸ suggest that at temperatures as low as 450°C H_2S dosing is still effective in producing a clean silicon surface.

APPENDIX A SOLUTIONS TO THE SCHRÖDINGER EQUATION

In order to obtain a useful graph relating the energy of a particle in a box with finite barriers and account for mass differences in the box and in the barrier, it is necessary to solve equation 2-6 and 2-7.

$$\tan \left[\frac{L}{2} \sqrt{\frac{8\pi^2 m_w^* E}{h^2}} \right] = \left[\frac{m_w^* (E_b - E)}{m_b^* E} \right]^{1/2} \quad (2-6)$$

$$\cot \left[\frac{L}{2} \sqrt{\frac{8\pi^2 m_w^* E}{h^2}} \right] = - \left[\frac{m_w^* (E_b - E)}{m_b^* E} \right]^{1/2} \quad (2-7)$$

where L is the box width, m_w^* is the particle mass in the well, m_b^* is the particle mass in the barrier, E_b is the barrier height and E is the energy due to confinement. Since no analytic solutions for these equations, numerical methods must be used solve for the quantum energy levels. The task at hand is to devise an efficient method to accomplish this goal. The job is made easier if the right hand argument is subtracted from both sides of each equation.

$$f(E) = \tan \left[\frac{L}{2} \sqrt{\frac{8\pi^2 m_w^* E}{h^2}} \right] - \left[\frac{m_w^* (E_b - E)}{m_b^* E} \right]^{1/2} \quad (A-1)$$

$$g(E) = \cot \left[\frac{L}{2} \sqrt{\frac{8\pi^2 m_w^* E}{h^2}} \right] + \left[\frac{m_w^* (E_b - E)}{m_b^* E} \right]^{1/2} \quad (A-2)$$

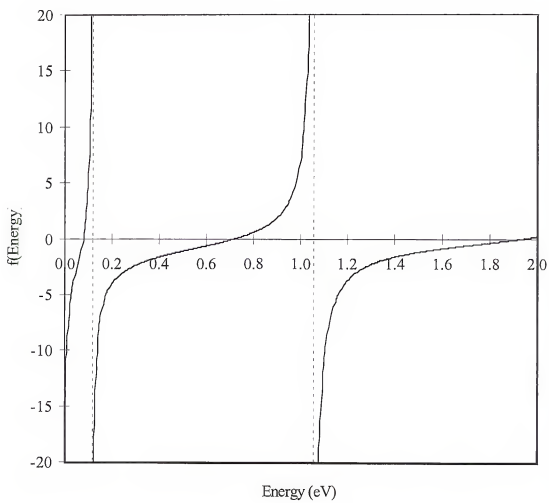


Figure A-1. Plot of equation A-1 for $L = 40 \text{ \AA}$, $m_w^* = 0.20$, $m_b^* = 0.40$ and $E_b = 2.00 \text{ eV}$.

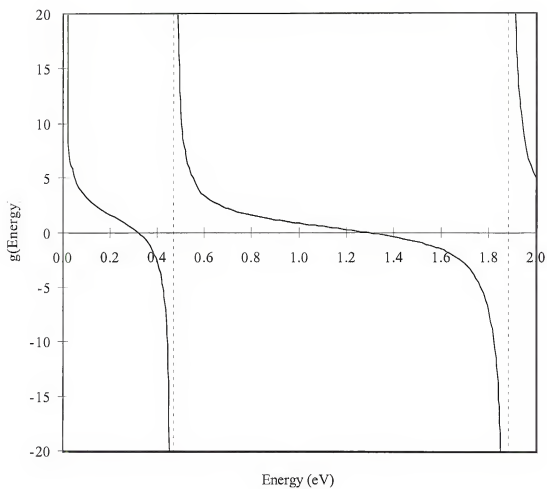


Figure A-2. Plot of equation A-2 for $L = 40 \text{ \AA}$, $m_w^* = 0.20$, $m_b^* = 0.40$ and $E_b = 2.00 \text{ eV}$.

Figures A-1 and A-2 show the general form of the equations for $L = 40 \text{ \AA}$, $m_w^* = 0.20$, $m_b^* = 0.40$ and $E_b = 2.00 \text{ eV}$. It is important to notice that both equations either increase or decrease monotonically between vertical asymptotes. The vertical asymptotes occur when the argument of tangent equals $(2n-1)\pi/2$ and the argument of cotangent equals $(2n)\pi/2$ for $(n = 1, 2, 3, \dots)$.

Knowing this, it is possible to solve for the location of the asymptotes algebraically. The location of the asymptotes is given by the following equations.

$$E = \frac{(2n-1)^2 \hbar^2}{8 m_w^* L^2} \quad (\text{A-3})$$

$$E = \frac{n^2 \hbar^2}{2 m_w^* L^2} \quad (\text{A-4})$$

With knowledge of the location of the vertical asymptotes, and the fact that the equations increase or decrease monotonically between asymptotes, the roots can be found on the interval $(E_{\text{Low}} + \Delta, E_{\text{Hi}} - \Delta)$. Where E_{Low} is the lower vertical asymptote, E_{Hi} is the upper vertical asymptote and Δ is an arbitrarily small number. For situations where $E_{\text{Hi}} > E_b$, the value of E_b can be substituted. The algorithm shown in figure A- 3 can be used to rapidly find the roots of equations A-1 and A-2. This algorithm divides the interval around the root in half with each iteration. Thus, the maximum error in the solution is given by:

$$\varepsilon < \frac{(E_{\text{Hi}} - E_{\text{Low}})}{2^{n+1}}, \quad n = \text{iteration number} \quad (\text{A-5})$$

For any realistic system ($E_b \leq 5 \text{ eV}$) the error will be on the order of 1 meV within 12 iterations.

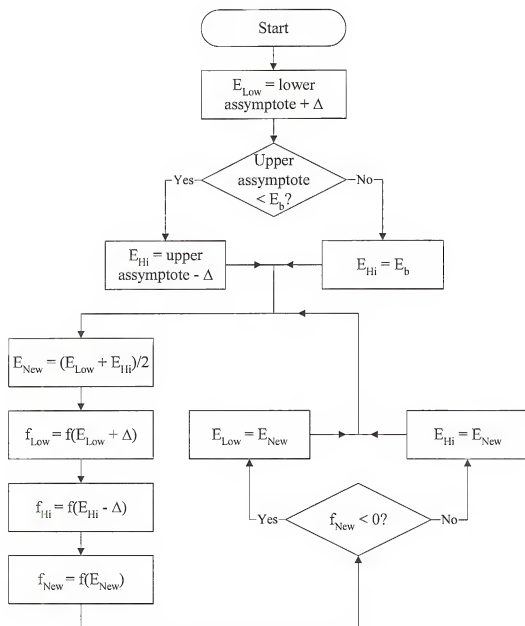


Figure A-3. Solution algorithm for quantum energy level calculations.

Traditionally, this algorithm would be implemented by encoding the algorithm in any of a number of computer languages. Usually a different compiler must be used for each operating system on which the code is to be run. The advent of personal computers and the variety of operating system used around the world mean that to distribute a program, the source code must be sent to each user and compiled to run under their operating system. This is at simple, but tedious task. Often the source code must be edited slightly to accommodate the differences between compilers.

The pervasive nature of personal computers in businesses and homes has led to the development of a number of a multitude of word processing and spreadsheet programs. In order to remain competitive, software vendors have updated their programs to read and write data in a competitor's file format. This flexibility of software in reading file formats can be used to great advantage in providing a truly portable algorithm.

Spreadsheet programs have been used for over a decade in solving differential equations. They provide a simple method for implementing repetitive calculations. What follows is an outline for using a spreadsheet program to implement an algorithm for numerical solutions. The primary component needed is a method for implementing IF statements. All of the IF statements in the algorithm can be expressed as an equation that will either be less than or greater than zero. What is then needed are a pair of equations that will return a value of one for an argument less than zero and a value of zero if the argument is greater than zero and vice-versa.

$$L(x) = \frac{\left(1 - \frac{|x|}{x}\right)}{2} \quad (\text{A-6})$$

$$G(x) = \frac{\left(\frac{|x|}{x} - 1\right)}{2} \quad (\text{A-7})$$

Equations A-6 and A-7 satisfy these requirements. These equations can be used to select between two variables to implement the algorithm outlined above. They are also useful in determining whether or not an asymptote lies in a region where equation A-1 or A-2 is undefined. In this case, it is necessary to use the barrier height as the upper interval. It is also possible to use these equations to determine if a root does not exist on the search interval since the nature of the equations being solved guarantees convergence to zero if in fact there is a root on the interval of interest. Knowing the width of the search interval, if the value of the function is greater than the error given by equation A-5, then there is no root on the search interval. Using these and other similar equations in different combinations, it is possible to develop mathematical equivalents of complex IF THEN ELSE structures. This set of equations then provides a basis for implementing numerical solutions in a spreadsheet environment.

Table A-1. Portion of quantum calculation spreadsheet showing formulas used to implement the solution algorithm.

A	B	C	D	E	F	G
1	Well Width	40		TOL	1.00E-06	
2		Electron	Hole	Total Offset:	2.50	
3	M_w	0.200	0.500	Level:	3	
4	M_b	0.400	0.750		Electron	Hole
5	CBO	2.00		Energy:	=G9*G10*F40	
6	VBO	0.50		Residual:	=G9*G10*G40	
7	Ratio	2.000				
8						
9	Low:	0.1175	High:	1.0576	Reality Check:	=G(E10-C9)
10			E_b :	2.00	Resid. Check:	=G(TOL-G45)
11			E_b check:	=L(E9-E10)		
12						
13	Electron Calculations		=G9*(E11*E9+(1-E11)*E10)-F1)+(1-G9)*2*F1			
14	Low	f(Low)	High	f(High)	New	f(New)
15	=F9*B9+(1-F9)*E1	=f(B15)		=f(D15)	=(B15+D15)/2	=f(F15)
16	=L(F15)*F15+G(F15)*B15	=f(B16)	=L(G15)*D15+G(G15)*G15	=f(D16)	=(B16+D16)/2	=f(F16)
17	=L(F16)*F16+G(F16)*B16	=f(B17)	=L(G16)*D16+G(G16)*G16	=f(D17)	=(B17+D17)/2	=f(F17)
18	=L(F17)*F17+G(F17)*B17	=f(B18)	=L(G17)*D17+G(G17)*G17	=f(D18)	=(B18+D18)/2	=f(F18)

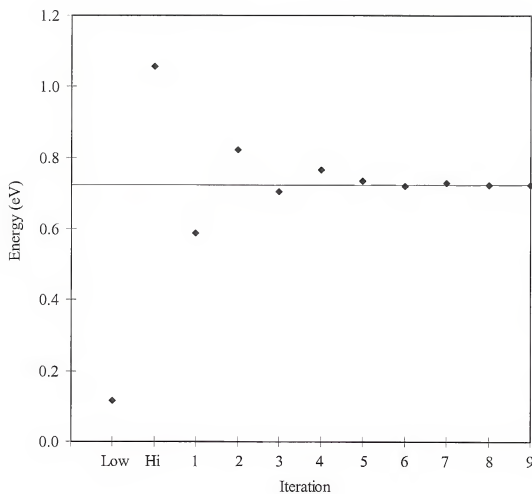


Figure A-4. Convergence characteristics of the solution using the same variables as figure A-1 and A-2.

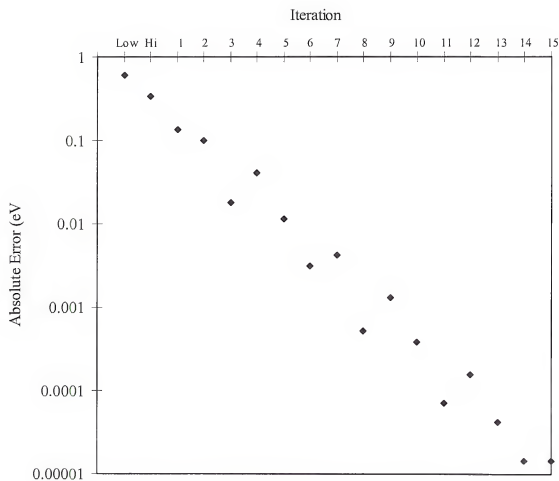


Figure A-5. Error of solution as a function of iteration using variables in figure A-1 and A-2.

Using formulas containing equations similar to A-6 and A-7, it is possible to select between values in a manner analogous to a traditional IF THEN ELSE statement in computer code.

Table A-1 shows some of the equations used in the spreadsheet developed to solve for quantum energy levels. The key to solving these equations reliably lies in checking to see if the equation being solved is undefined on the interval being searched and whether or not the final value is sufficiently close to zero.

The upper left portion of the spreadsheet contains information on the particle characteristics and the width and barrier height of the quantum well. Cells C9 and E9 contain formulas to calculate the lower and upper vertical asymptotes for the energy level give in cell F3. G9 checks to see if the energy equation is undefined over the entire interval of interest. E11 serves to verify if the upper asymptote is outside the region were the energy equation is defined. C11 is a final check to see if the solution has converged to zero. The spreadsheet is set to return a value of zero for the energy and residual for any energy level that does not converge. Table A-2 shows a sample output from the spreadsheet calculations.

Table A-2. Sample output from spreadsheet calculations.

	Well	Barrier	Mass Ratio	
Electron mass	0.200	0.400	2.000	
Hole mass	0.500	0.750	1.500	
Band gap (eV)	1.120	3.620		
	Total Offset:	2.500		
	Well Width:	40		
	Conduction Band offset:	2.000		
Energy Level	Electron	e ⁻ Residual	Hole	h ⁺ Residual
Ground State	0.0403	9.225E-10	0.0164	3.765E-09
1 st Excited	0.1617	3.912E-10	0.0654	9.025E-10
2 nd Excited	0.3658	1.810E-10	0.1468	1.123E-09
3 rd Excited	0.6533	4.153E-10	0.2600	4.630E-10
4 th Excited	1.0226	1.998E-10	0.4036	6.486E-10
5 th Excited	1.4590	2.727E-10	0.5750	2.739E-10
6 th Excited	0.0000	0.000E+00	0.7660	3.322E-10
7 th Excited	0.0000	0.000E+00	0.0000	0.000E+00
8 th Excited	0.0000	0.000E+00	0.0000	0.000E+00
9 th Excited	0.0000	0.000E+00	0.0000	0.000E+00

APPENDIX B

APPROXIMATE SOLUTIONS TO THE SCHRÖDINGER EQUATION

The most common solution to the Schrödinger equation seen in textbooks is the solution for a particle in a one dimensional box with infinite barriers (equation 2-4). This solution has the unfortunate handicap being simple and easy to use. It is unfortunate, because as shown in Chapter 2, it can be extremely inaccurate. The used to take into account the presence of a finite barrier and the differences in effective mass inside the well and the barrier are far more accurate, but suffer from the non-existence of an analytical solution. The difficulty lies in finding a solution to the trigonometric term in the equations.

Before embarking on the journey to find an algebraic approximation to the tangent function, it is helpful to review its basic properties. There are vertical asymptotes located at $\pi/2 (+\infty)$ and $-\pi/2 (-\infty)$ and it passes through the origin. Two simple function that can provide the asymptotic behavior are: $-1/(x + \pi/2)$ and $1/(-x + \pi/2)$. The sum of these equations at $x = 0$ is zero, so they should provide a reasonable approximation to the tangent function.

$$\tan(x) \cong \frac{-1}{\left(x + \frac{\pi}{2}\right)} + \frac{1}{\left(-x + \frac{\pi}{2}\right)} = \frac{-2x}{\left(x^2 - \frac{\pi^2}{4}\right)} \quad (\text{B-1})$$

As shown in figure B-1, this simple equation provides a reasonable approximation to the tangent function. The error between the approximation and the tangent function shown in

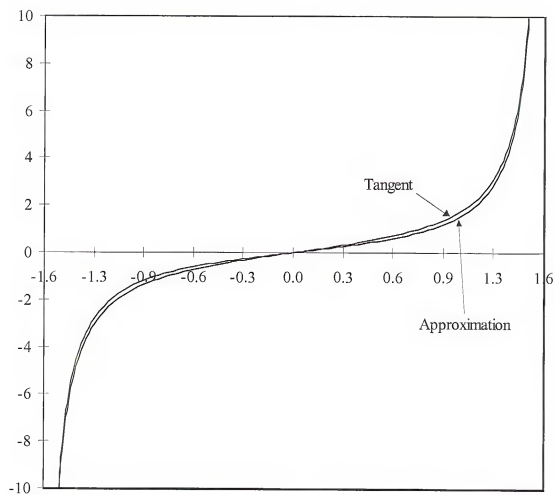


Figure B-1. Comparison of tangent function and algebraic approximation.

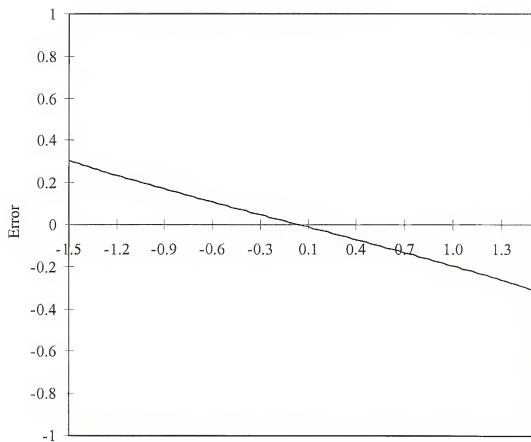


Figure B-2. Error between the tangent approximation and the tangent function.

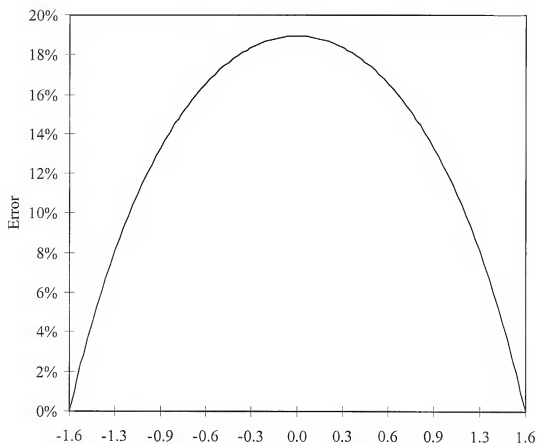


Figure B-3. Percent error between the tangent approximation and the tangent function.

figure B-2 indicates that a substantial improvement can be made by adding a linear term to equation B-1. Fitting the error to a linear function and incorporating this new term into the approximation gives:

$$\tan(x) \cong \frac{-2x}{\left(x^2 - \frac{\pi^2}{4}\right)} - 0.19695x \quad (\text{B-2})$$

Although the addition of this linear term reduces the maximum error two $\sim 0.75\%$, it will not be used in finding an algebraic approximation to equation 2-9. The addition of the linear term complicates the algebra and gives higher order terms. Substituting B-1 into equation 2-9 yields:

$$\frac{4x^2}{x^4 - \frac{x^2\pi^2}{2} - \frac{\pi^4}{16}} = \sqrt{\frac{m_w^*(E_b - E)}{m_b^*E}}, \text{ where } x = \frac{L}{2} \sqrt{\frac{8m_w^*\pi^2 E}{h^2}} \quad (\text{B-2})$$

Following through the algebra and solving for zero gives:

$$4\eta E = \left(\eta^2 E^2 - \frac{\pi^2 \eta^2 E}{2} - \frac{\pi^4}{16} \right) \left[\frac{m_w^*(E_b - E)}{m_b^*E} \right], \text{ where } \eta = \frac{2L^2 m_w^* \pi^2 E}{h^2} \quad (\text{B-3})$$

$$4\eta m_b^* E^2 = \left(\eta^2 E^2 - \frac{\pi^2 \eta^2 E}{2} - \frac{\pi^4}{16} \right) [m_w^*(E_b - E)] \quad (\text{B-4})$$

$$\frac{4\eta m_b^* E^2}{m_w^*} = \eta^2 E_b E^2 - \frac{\pi^2 \eta^2 E_b E}{2} - \frac{\pi^4 E_b}{16} + \eta^2 E^3 + \frac{\pi^2 \eta^2 E^2}{2} + \frac{\pi^4 E}{16} \quad (\text{B-5})$$

$$\frac{4\eta m_b^* E^2}{m_w^*} = \eta^2 E_b E^2 - \frac{\pi^2 \eta^2 E_b E}{2} - \frac{\pi^4 E_b}{16} + \eta^2 E^3 + \frac{\pi^2 \eta^2 E^2}{2} + \frac{\pi^4 E}{16} \quad (\text{B-6})$$

$$\eta^2 E^3 + \left(\frac{4\eta m_b^*}{m_w^*} + \eta^2 E_b - \frac{\pi^2 \eta^2}{2} \right) E^2 + \left(\pi \eta^2 + \frac{\pi^4}{16} \right) E + \frac{\pi^4 E_b}{16} = 0 \quad (\text{B-7})$$

If it is assumed that the root is < 1 , then the cubic term will be $\ll 1$ and may be ignored, leaving a simple quadratic equation in E . Which can be easily solved.

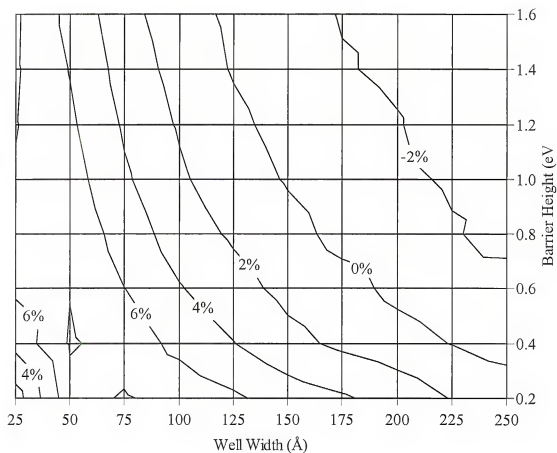


Figure B-4. Ground state energy error for equation B-8 with $m_w^* = m_b^* = 0.05$ and a correction factor of 0.97.

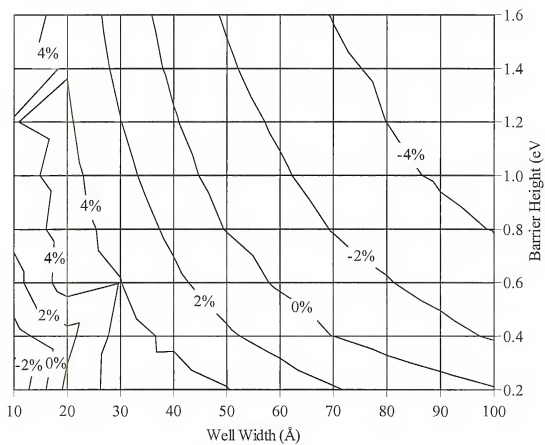


Figure B-5. Ground state energy error for equation B-8 with $m_w^* = m_b^* = 0.20$ and a correction factor of 0.97.

$$\left(\frac{4\eta m_b^*}{m_w^*} + \eta^2 E_b - \frac{\pi \eta^2}{2} \right) E^2 + \left(\pi \eta^2 + \frac{\pi^*}{16} \right) E + \frac{\pi^* E_b}{16} = 0 \quad (\text{B-8})$$

It can be shown that the roots of this equation are always real for $E_b > 0$. The negative root has no meaning for this equation and the positive root corresponds to the ground state quantum energy level for the particle. Similar equations can be defined for the higher energy levels.

This accuracy of the approximation varies with the parameters of the system. It is surprisingly accurate for extremely narrow or wide well widths. The error goes through a maximum and then decreases. The input parameters were varied to estimate the expected error resulting from the approximations made. It was noted that over a large parameter space, the average error was typically on the order of 3 % with a maximum error of ~ 8 %. In the most extreme cases, the absolute errors were noted to be on the order of 20 meV. Noting that the errors were always positive and on the order of 3 %, the estimation of the energy can be improved by using an adjustable parameter to reduce the energy level. Using a correction factor of 0.97 reduces the maximum error to ~ 6 % and the average error to < 3 %.

While equation B-8 is more complicated than the infinite barrier solution, it is not necessary to resort to numerical methods to find a solution. Additionally, it has been shown to provide reasonably accurate results.

REFERENCES

1. L. T. Canham, Appl Phys. Lett. **57**, 1046 (1990).
2. R. E. Hummel and S. Chang, Appl. Phys. Lett., **61** 1965 (1992).
3. D. Z. Tsang, Lincoln Laboratories Journal., **4** 31 (1991).
4. J. W. Goodman, F. I. Leonberger, S. Y. Kung and R. A. Rathale, Proc. IEEE., **72** 850 (1984).
5. M. R. Feldman, S. C. Esener, C. C. Guest and S. H. Lee, Appl. Opt., **27** 1742 (1984).
6. J. Nishizawa, M. Saito, in Proceedings of the Sixth International Conference on Chemical Vapor Deposition, Electrochem. Soc., Pennington, New Jersey (1981) 317.
7. VLSI Technology, S. M. Sze, ed., McGraw-Hill Book Company, New York (1988).
8. C. Cobianu and C. Pavelescu, Thin Solid Films, **117** 211 (1984).
9. A. C. Adams, C. D. Capio, J. Electrochem. Soc., **126** 1042 (1979).
10. K. Watanabe, T. Tanigaki, S. Wakayama, J. Electrochem. Soc., **128** 2630 (1981).
11. W. Michaelis and M. H. Pilkuhn, Phys. Stat. Sol., **36** 311 (1969).
12. L. T. Catham, Appl. Phys. Lett., **57** 1046 (1990).
13. J. M. Macauley *et al*, in Light Emission from Silicon, S. S. Iyer, L. T. Canham and R. P. Collins eds., Materials Res. Soc. Pittsburgh, PA (1992) **256** 46.
14. N. M. Kalkhoran, F. Namavar and H. P. Maruska, in Light Emission from Silicon, S. S. Iyer, L. T. Canham and R. P. Collins eds., Materials Res. Soc. Pittsburgh, PA (1992) **256** 89.
15. Z. Y. Xu, M. Gal and M. Gross, Appl. Phys. Lett., **60** 1375 (1992).
16. M. Stutzmann *et al.*, Adv. Sol. State Physics., **32** (1992).

17. S. M. Prokes, J. A. Freitas, Jr. and P. C. Seaeson, Appl. Phys. Lett., **60** 3295 (1992).
18. M. A. Tischler, R. T. Collins, J. H. Stathis and J. C. Tsang, Appl. Phys. Lett., **60** 6393 (1992).
19. H. Tamura, M. Rückschloss, T. Wirchem and S. Verprek, Appl. Phys. Lett., **65** 1537 (1994).
20. V. P. Koch, A. Kux, F. Muller, T. Muschik, F. Koch and V. Lehmann in Light Emission from Silicon, S. S. Iyer, L. T. Canham and R. P. Collins eds., Materials Res. Soc. Pittsburgh, PA (1992) **256** 41.
21. S. S. Chang, Production and Characterization of Photoluminescing Spark-Processed Si, Doctoral Dissertation, University of Florida (1994).
22. D. Zhang, R. M. Kolbas, P. Mehta, A. K. Singh, D. J. Lichtenwalner, K. Y. Hseih and A. I. Kingon, in Light Emission from Silicon, S. S. Iyer, L. T. Canham and R. P. Collins eds., Materials Res. Soc. Pittsburgh, PA (1992) **256** 35.
23. U. Gnutzmann, K. Clausecker, Appl. Phys., **3** 9 (1974).
24. K. Böer, Survey of Semiconductor Physics, Van Nostrand Reinhold, New York (1990).
25. S. N. Levine, Quantum Physics of Electronics, The Macmillan Company, New York (1965).
26. N. S. Averkiev, V. M. Asnin, A. B. Churilov, I. I. Markov, N. E. Mokrousov, Y. Yu. Silov and V. I. Stepanov, JETP Lett., **55** 657 (1992).
27. D. Cherns, D. Loretto, N. Chand and J. M. Gibson, Philosophical Magazine A, **63** 1335 (1991).
28. M. Yamaguchi, J. Mater. Res., **6** 376 (1991).
29. H. Kroemer, T. Y. Liu and P. M. Petroff, J. Cryst. Growth., **65** 96 (1989).
30. M. Yamaguchi, M. Sugo and Y. Itoh, Appl. Phys. Lett., **54** 2568 (1989).
31. T. Soga, T. Jimbo and M. Umeno, Appl. Phys. Lett., **56** 1433 (1990).
32. N. A. El-Masry, J. C. Tarn and N. H. Karam, J. Appl. Phys., **64** 3672 (1988).
33. M. Yamaguchi, T. Nishioka and M. Sugo, Appl. Phys. Lett., **54** 24 (1989).

34. G. Bremond, et al, *Material Science and Engineering*, **B9** 143 (1991).
35. D. Pribat, M. Dupuy, P. Legagneux and C. Collet, *Appl. Phys. Lett.*, **57** 375 (1990).
36. D. Pribat, V. Provendier, M. Dupuy, P. Legagneux and C. Collet, *Jpn. J. Appl. Phys.*, **30** L341 (1991).
37. Y. Ujiie and T. Nishinaga, *Jpn. J. Appl. Phys.*, **63** L337 (1989).
38. E. A. Fitzgerald, *J. Vac. Sci. Tech. B*, **7** 782 (1989).
39. G. P. Watson, D. G. Ast, T. J. Anderson and Y. Hayakawa, *Appl. Phys. Lett.*, **58** 2517 (1991).
40. E. A. Fitzgerald and N. Chand, *J. Electron. Mater.*, **20** 839 (1991).
41. G. Destriau, *J. de Chemie Physique.*, **33** 587 (1936).
42. G. R. Rawlins, *J. Mat. Sci.*, **5** 881 (1970).
43. P. Lilley, P. M. R. Kay, C. N. W. Litting, *J. Mat. Sci.*, **10** 1317 (1975).
44. Y. Yonggnian, C. F. Hickey and U. J. Gibson, *Thin Solid Films.*, **151** 207 (1987).
45. P. J. Wright and B. Cockayne, *J. Cryst. Growth.*, **59** 148 (1982).
46. H. P. Maruska, R. Sudharsanan, E. Bretschneider, A. Davydov, J. E. Yu, B. Pathangey, K. S. Jones and T. J. Anderson in Microcrystalline and Nanocrystalline Semiconductors., R. W. Collins, C. C. Tsai, M. Hirose, F. Koch and L. Bruijs eds., *Materials Res. Soc. Pittsburgh, PA* (1995) **358** 987.
47. R. T. Shuey, Semiconducting Ore Minerals., Elsevier Scientific Publishing, New York (1975).
48. J. A. Van Vechten, *J. Electrochem. Soc.*, **122** 419 (1975).
49. F. A. Köger, The Chemistry of Imperfect Crystals., North-Holland, Amsterdam (1964).
50. L. C. Olsen, R. C. Bohara and D. L. Barton, *Appl. Phys. Lett.*, **34** 528 (1979).
51. S. Yamaga, A. Yoshikawa and H. Kasai, *J. Cryst. Growth.*, **86** 252 (1988).
52. T. Yasuda, K. Hara and H. Kukimoto, *J. Cryst. Growth.*, **77** 485 (1986).

53. Y. Nakanishi, K. Kimura, G. Shimaoka and M. Ogita, Appl. Surface Sci., **33/34** 677 (1988).
54. J. E. Yu, K. S. Jones, B. Pathangey, E. Bretschneider and T. J. Anderson J. Electron. Mater., **23** 299 (1994).
55. A. G. Milnes, Deep Levels in Semiconductors, Wiley, New York (1973).
56. K. Chen, X. Huang, J. Xu and D. Feng, Appl. Phys. Lett., **61** 2069 (1992).
57. P. N. Saeta and A. C. Gallagher, Microcrystalline and Nanocrystalline Semiconductors, R. W. Collins, C. C. Tsai, M. Hirose, F. Koch and L. Bruijs, eds., Materials Res. Soc. Pittsburgh, PA (1995) **358** 981.
58. J. M. Baribeau, Z. H. Lu and D. J. Lockwood, LEOS Newsletter, April 1996 7 (1996).
59. E. F. Steigmeier, R. Morf, D. Grützmacher, H. Auderset, B. Delley and R. Wessicken, Appl. Phys. Lett., **69** 4165 (1996).
60. R. L. Anderson, Solid-State Electron., **5** 341 (1962).
61. F. G. Allen, J. Phys. Chem. Solids, **8** 119 (1959).
62. C. A. Mead, Solid State Electronics, **9** 1023 (1965).
63. M. Aven and C. A. Mead, Appl. Phys. Lett., **7** 8 (1965).
64. R. Dingle, W. Weigmann and C. H. Henry, Phys. Rev. Lett., **33** 827 (1974).
65. R. C. Miller, A. C. Gossard, D. A. Kleinman and O. Munteanu, Phys. Rev. B, **29** 3740 (1984).
66. S. H. Wei and A. Zunger, Phys Rev. Lett., **59** 144 (1987).
67. T. Nakayama, Electronic Structures of Strained II-VI Superlattices, in II-VI Semiconducting Compounds, ed. M. Jain, World Scientific Publishing, Singapore (1993).
68. G. Margaritondo, ed., Electronic Structure of Semiconductor Heterojunctions, Kluwer Academic Publishers, Boston (1988).
69. J. Tersoff, Phys. Rev. B, **30** 4874 (1984).
70. D. W. Niles and G. Margaritondo, Phys. Rev. B, **34** 2923 (1986).

71. W. A. Harrison, *J. Vac. Sci. Technol.*, **14** 1016 (1977).
72. M. Cardona and N. E. Christensen, *J. Vac. Sci. Technol.*, **B6** 1285 (1988).
73. H. Kroemer, *Surface Science*, **132** 543 (1983).
74. W. G. Wilke, R. Seedorf and K. Horn, *J. Cryst. Growth*, **101** 620 (1990).
75. P. Perfetti, C. Quaresima, C. Coluzza, C. Fortunato and G. Margaritondo, *Phys. Rev. Lett.*, **57** 2065 (1986).
76. Ch. Maierhofer, S. Kulkarni, M. Alonso, T. Reich and K. Horn, *J. Vac. Sci. Technol.*, **B9** 2238 (1991).
79. G. B. Stringfellow, *Organometallic Vapor-Phase Epitaxy: Theory and Practice.*, Academic Press, San Diego (1989).
80. B. Cockayne and P. J. Wright, *J. Cryst. Growth*, **68** 223 (1984).
81. S. M. Gatos, B. A. Scott, D. B. Beach, R. Imbuhl and J. E. Demuth, *J. Vac. Sci. Technol.*, **A5** 628 (1987).
82. J. R. Engstrom, L. Q. Xia, M. J. Furjanic and D. A. Hansen, *Appl. Phys. Lett.*, **63** 1821 (1993).
83. F. E. Saalfeld and H. J. Svec, *Inorg. Chem.*, **2** 50 (1963).
84. *The Mechanical Engineer's Handbook. 12th ed.*, Colin Carmichael and J. K. Salisbury, eds., Wiley, New York (1950).
85. G. A. Goodenough, *Principles of Thermodynamics.*, Henry Holt and Company, New York (1932).
86. E. Fermi, *Thermodynamics.*, Dover Publications, New York (1936).
87. J. C. Maxwell, *A Treatise on Electricity and Magnetism.*, Clarendon Press, Oxford (1892).
88. W. Wien, *Neuere Probleme der Theoretischen Physik.*, Leipzig, Berlin (1913).
89. H. Kangro, *Early History of Planck's Radiation Law.*, Taylor and Francis Ltd., London (1976).
90. L. de Broglie, *Matter and Light: The New Physics.*, Dover Publications, New York (1946).

91. P. W. Atkins, Physical Chemistry, W. H. Freeman and Company, New York (1986).
91. H. Hertz, Ann. Phys. (Leipzig), **17** 983, (1887).
92. A. Einstein, Ann. Phys. (Leipzig) **17** 132 (1905).
93. A. Einstein and L. Infeld, The Evolution of Physics, Simon and Schuster, New York (1961).
94. E. Schrödinger, Collected Papers on Wave Mechanics, Chelsea Publishing Company, New York (1978).
95. L. de Broglie, Matter and Light: The New Physics, Dover Publications, New York (1946).
96. D. B. Cook, Schrödinger's Mechanics, World Scientific, London (1988).
97. R. H. Fowler and L. Nordheim, Roy. Soc. Proc. A, **119** 173 (1928).
98. M. Aven, Ext. Abstr. Meet. Electrochem. Soc., **11** 46 (1962).
99. F. A. Köger, The Chemistry of Imperfect Crystals, North-Holland, Amsterdam (1964).
100. A. G. Fischer, J. Electrochem. Soc., **110** 733 (1963).
101. F. C. Frank and J. H. Van der Merwe, Proc. Roy. Soc., **A189**, 205 (1949).
102. J. W. Matthews, Epitaxial Growth, ed. J. W. Matthews, Academic Press, New York (1975).
103. J. W. Matthews, J. Vac. Sci. Tech., **12**, 126 (1975).
104. J. C. Bean, Physics Today, **39**, 2 (1986).
105. D. Aspnes and J. Ihm, in: Heteroepitaxy on Silicon II, eds. J. C. C. Fan, J. M. Phillips and B. Y. Tsaur, Mater. Research Soc., Pittsburgh, PA, 45 (1987).
106. P. M. Petroff, J. Vac. Sci. Technol. B., **4** 874 (1986).
107. M. Akiyama, Y. Kawarda, T. Ueda, S. Nishi and K. Kaminishi, J. Crystal Growth, **77** 490 (1986).
108. W. I. Wang, Appl. Phys. Lett., **44** 1149 (1984).

109. N. Otsika, C. Choi, Y. Nakamura, S. Nagakura, R. Fischer, C. K. Peng and H. Morkoç, *Appl. Phys. Lett.*, **54** 2522 (1983).
110. R. Fischer, W. T. Masselink, J. Klem, T. Henderson, T. C. McGlinn, M. V. Klein, H. Morkoç, J. H. Mazur and J. Washburn, *J. Appl. Phys.*, **58** 374 (1985).
111. T. Won, G. Munns, R. Houdré and H. Morkoç, *Appl. Phys. Lett.*, **49** 1257 (1986).
112. P. L. Jones, J. Esson and K. E. Singer, *Thin Solid Films*, **43** 295 (1977).
113. J. Pfeifer, E. Sz. Haraszthy and M. Farkas-Jahnke, *Thin Solid Films*, **11** 71 (1972).
114. R. E. Hong, and D. A. Kramer, *RCA Review*, B30B 285 (1969).
115. H. Samelson, *J. Appl. Phys.*, **32** 309 (1961).
116. H. P. Maruska, R. Sudharsanan, E. Bretschneider, A. Davydov, J. E. Yu, B. Pathangey, K. S. Jones and T. J. Anderson, in Microcrystalline and Nanocrystalline Semiconductors, R. W. Collins, C. C. Tsai, M. Hirose, F. Koch and L. Bruijs eds., *Materials Res. Soc.*, Pittsburgh, PA **358** 987 (1995).
117. M. Yokoyama, K. Kashiro and S. Ohta, *J. Appl. Phys.*, **60** 3508 (1986).
118. K. Harabayashi and O. Kogure, *Jap. J. Appl. Phys.*, **24** 1590 (1985).
119. P. Lilley, P. L. Jones and C. N. W. Littig, *J. Mater. Sci.*, **5** 891 (1970).
120. S. Oda and H. Kukimoto, *IEEE Trans. Electron Devices.*, **ED-24** 923 (1977).
121. H. Kukimoto, S. Oda and T. Nakayama, *J. Luminescence*, **18/19** 365 (1979).
122. A. E. Thomas, G. J. Russell and J. Woods, *J. Cryst. Growth.*, **63** 265 (1983).
123. R. G. Kaufman and P. Dowbor, *J. Appl. Phys.*, **45** 4487 (1974).
124. V. A. Williams, *J. Electrochem. Soc.*, **113** 234 (1966).
125. L. C. Olsen, R. C. Bohara and D. L. Barton, *Appl. Phys. Lett.*, **34** 528 (1979).
126. S. Yamaga, A. Yoshikawa and H. Kasai, *J. Cryst. Growth.*, **86** 252 (1988).
127. T. Yasuda, K. Hara and H. Hukimoto, *J. Cryst. Growth.*, **77** 485 (1986).
128. K. C. Kao and W. Hwang, Electrical Transport in Solids. Pergamon Press, New

York, 1981.

129. F. A. Kröger, G. Diemer and H. A. Klasens, *Phys. Rev.*, **103** 279 (1956).
130. R. Smith, *Phys. Rev.* **97**, 1525 (1955).
131. M. Aven and C. A. Mead, *Appl. Phys. Lett.*, **7** 8 (1965).
132. G. H. Blount, M. W. Fischer, R. G. Morrison and R. H. Bube, *J. Electrochem. Soc.*, **113** 690 (1966).
133. V. A. Williams, *J. Electrochem. Soc.*, **113**, 234 (1966).
134. R. G. Kaufman and P. Dowbar, *J. Appl. Phys.*, **45** 448 (1974).
135. L. C. Olsen, R. C. Bohara and D. L. Barton, *Appl. Phys. Lett.*, **34** 528 (1979).
136. T. Yasuda, K. Hara and H. Kukimoto, *J. Cryst. Growth*, **77** 485 (1986).
137. I. P. McClean, N. Konofaos and C. B. Thomas, *J. Appl. Phys.*, **74** 397 (1993).
138. T. Yasuda, K. Hara and H. Kukimoto, *J. Cryst. Growth*, **77** 485 (1986).
139. S. Yamaga, A. Yoshikawa and H. Kasai, *J. Cryst. Growth*, **86** 252 (1988).
140. L. C. Olsen, R. C. Bohara and D. L. Barton, *Appl. Phys. Lett.*, **34** 528 (1979).
141. R. T. Holm, P. H. Klein and P. E. R. Nordquist, Jr., *J. Appl. Phys.*, **60** 1479 (1986).
142. G. Alameddine, Private communication "Simulation of Infrared Reflectance Spectra of Insulators and Semiconductors."
143. A. G. Milnes, Deep Levels in Semiconductors, Wiley, New York (1973).
144. A. Wachtel, *J. Electrochem. Soc.*, **108** 534 (1961).
145. K. Sugibuchi and Y. Mita, *Phys. Rev.*, **147** 355 (1966).
146. G. A. Reider, U. Höfer and T. F. Heinz, *Phys. Rev. Lett.*, **66** 1994 (1995).
147. J. R. Engstrom, L. Q. Xia, M. J. Furjanic and D. A. Hansen, *Appl. Phys. Lett.*, **63** 1821 (1993).
148. T. Horie, Y. Takakuwa, T. Yamaguchi and N. Miyamoto, *J. Cryst. Growth*, **136** 344 (1994).

149. G. A. Reider, U. Hofer and T. F. Heinz, *Phys. Rev. Lett.*, **66** 1991 (1994).
150. P. J. Ross, Taguchi Techniques for Quality Engineering., McGraw-Hill, New York (1996).
151. R. DeVor, T. Chang and W. Sutherland, Statistical Quality Design and Control. Macmillan, New York 1992.
152. G. Box, W. Hunter and J. Hunter, Statistics for Experimenters: An Introduction to Design, Data Analysis and Model Building. Wiley, New York 1978.
153. D. G. Schimmel, *J. Electrochem. Soc.*, **123** 734 (1976).
154. W. Kern and D. Puotinen, *RCA Rev.*, **31** 187 (1970).
155. C. F. Corallo and G. B. Hoflund, *Surface and Interface Analysis*, **12** 297 (1988).
156. S. L. Cohen in Surface Chemical Cleaning and Passivation for Semiconductor Processing., **259** 3, Mater. Res. Soc., Pittsburgh, PA (1993).
157. M. Liehr, C. Greenlief, S. R. Kasi and M. Offenburg, *Appl. Phys. Lett.*, **56** 629 (1990).
158. B. Meyerson, F. Himpsel and K. Uram, *Appl. Phys. Lett.*, **57** 1034 (1990).
159. T. O. Sedgwick, P. D. Agnello and D. A. Grützmacher, *J. Electrochem. Soc.*, **140** 3684 (1993).
160. M. Liehr, C. Greenlief, S. R. Kasi and M. Offenburg, *Appl. Phys. Lett.*, **56** 629 (1990).
161. P. Dumas, Y. J. Chabal and G. S. Higashi, *Phys. Rev. Lett.*, **65** 1124 (1990).
162. M. Liehr, *J. Vac. Sci. Technol. A.*, **8** 1939 (1990).
163. G. S. Higashi, R. S. Becker, Y. J. Chabal and A. J. Becker, *Appl. Phys. Lett.*, **58** 1657 (1991).
164. Y. J. Chabal in Surface Chemical Cleaning and Passivation for Semiconductor Processing., **259** 349, Mater. Res. Soc., Pittsburgh, PA (1993).
165. Surface Chemical Cleaning and Passivation for Semiconductor Processing., **259**, Mater. Res. Soc., Pittsburgh, PA (1993).
166. T. O. Sedgwick, P. D. Agnello and D. A. Grützmacher, *J. Electrochem. Soc.*, **140**

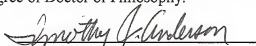
- 3684 (1993).
167. M. Tabe, T. T. Chiang, I. Lindau and W. E. Spicer, *Phys. Rev. B*, **34** 5780 (1986).
168. Y. Sasaki and M. Kitahara, *J. Appl. Phys.*, **76** 4344 (1994).
169. K. Era, S. Shionoya, Y. Washizawa and H. Ohmatsu, *J. Phys. Chem. Solids*, **29** 1843 (1968).
170. D. A. Cusano in Physics and Chemistry of II-VI Compounds, M. Aven and J. S. Prener, eds., North-Holland Publishing Company, Amsterdam (1967).
171. P. J. Dean, A. D. Pitt, M. S. Skolnick, P. J. Wright and B. Cockayne, *J. Cryst. Growth*, **59** 301 (1982).
172. N. Teraguchi, Y. Takemura, R. Kimura, M. Konagai and K. Takahashi, *J. Cryst. Growth*, **93** 720 (1988).
173. S. Takata, M. Minami, T. Miyata and H. Nanto, *J. Cryst. Growth*, **86** 257 (1988).
174. P. Yeh, Optical Waves in Layered Media, Wiley, New York (1988).
175. M. Aven and D. A. Cusano, *J. Appl. Phys.*, **35** 606 (1964).
176. S. M. Sze, VLSI Technology, McGraw-Hill, New York (1988).
177. Y. Yongnian, C. F. Hickey and U. J. Gibson, *Thin Solid Films*, **151** 207 (1987).

BIOGRAPHICAL SKETCH

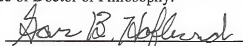
Eric Colin Bretschneider was born on June 3, 1966, in Panama City Florida. After attending schools in Oklahoma and Florida, he graduated as Valedictorian from Admiral Farragut Academy in St. Petersburg, Florida in 1984. He attended Tulane University in New Orleans, Louisiana and graduated with a Bachelor of Science in Engineering in the field of Chemical Engineering. After working briefly at Shell Oil, he returned to Florida and entered into the graduate school program at the University of Florida to begin studies for his Doctoral degree in the Department of Chemical Engineering. There he met his wife Kathleen.

He is currently employed by EMCORE Corporation and resides in New Jersey with his wife and family.

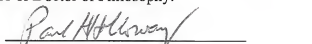
I certify that I have read this study and that in my opinion it conforms to acceptable standards of scholarly presentation and is fully adequately, in scope and quality, as a dissertation for the degree of Doctor of Philosophy.


Timothy J. Anderson, Chairman
Professor of Chemical Engineering

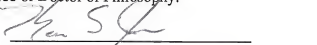
I certify that I have read this study and that in my opinion it conforms to acceptable standards of scholarly presentation and is fully adequately, in scope and quality, as a dissertation for the degree of Doctor of Philosophy.


Gar B. Hoflund
Professor of Chemical Engineering

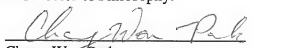
I certify that I have read this study and that in my opinion it conforms to acceptable standards of scholarly presentation and is fully adequately, in scope and quality, as a dissertation for the degree of Doctor of Philosophy.


Paul H. Holloway
Professor of Materials Science and Engineering

I certify that I have read this study and that in my opinion it conforms to acceptable standards of scholarly presentation and is fully adequately, in scope and quality, as a dissertation for the degree of Doctor of Philosophy.

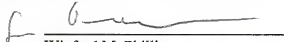

Kevin S. Jones
Professor of Materials Science and Engineering

I certify that I have read this study and that in my opinion it conforms to acceptable standards of scholarly presentation and is fully adequately, in scope and quality, as a dissertation for the degree of Doctor of Philosophy.


Chang-Won Park
Associate Professor of Chemical Engineering

This dissertation was submitted to the Graduate Faculty of the College of Engineering and to the Graduate School and was accepted as partial fulfillment of the requirements for the degree of Doctor of Philosophy.

December 1997

A handwritten signature in dark ink, appearing to read 'W. M. Phillips', is written over a horizontal line.

Winfred M. Phillips
Dean, College of Engineering

Karen A. Holbrook
Dean, Graduate School